

AILE TAMM

Atomic layer deposition of
high-permittivity insulators from
cyclopentadienyl-based precursors



The study was carried out at the Institute of Physics, University of Tartu

The Dissertation was admitted on October 1, 2010 in partial fulfilment of the requirements of the degree of Doctor of Philosophy in physics (solid state physics), and allowed for defence by the Council of the Institute of Physics, University of Tartu

Supervisors: Dr. Kaupo Kukli, Department of Materials Science, Institute of Physics, University of Tartu, Tartu, Estonia

Dr. Kalev Tarkpea, Department of Coordination, Institute of Physics, University of Tartu, Tartu, Estonia

Opponents: Dr. Malle Krunks, Department of Materials Science, Faculty of Chemical and Materials Technology, University of Technology, Tallinn, Estonia

Prof. Karol Fröhlich, D.Sc., Institute of Electrical Engineering, Slovak Academy of Science, Bratislava, Slovakia

Defence: November 26, 2010 at the University of Tartu, Estonia

ISSN 1406–0647

ISBN 978–9949–19–500–8 (trükis)

ISBN 978–9949–19–501–5 (PDF)

Autoriõigus: Aile Tamm, 2010

Tartu Ülikooli Kirjastus

www.tyk.ee

Tellimus nr. 583

CONTENTS

| | |
|---|----|
| LIST OF PUBLICATIONS..... | 7 |
| PRESENTATIONS AT INTERNATIONAL CONFERENCES AND DOMESTIC DOCTORAL SCHOOLS:..... | 7 |
| THE AUTHOR’S CONTRIBUTION TO THE PAPERS FORMING THE BASIS OF THE THESIS | 10 |
| LIST OF ABBREVIATIONS AND ACRONYMS | 11 |
| 1. INTRODUCTION..... | 12 |
| 2. STATEMENT | 15 |
| 3. WHY DO WE NEED THIN FILMS..... | 16 |
| 3.1. Some potential applications fields of nanometric thin films | 16 |
| 3.2. Silicon-based nanoelectronics | 17 |
| 3.3. Graphene-based nanoelectronics | 18 |
| 3.4. Other low-dimensional nanomaterials..... | 19 |
| 3.5. Dynamic Random Access Memories | 20 |
| 4. THIN FILM DEPOSITION TECHNOLOGY | 23 |
| 4.1. Atomic layer deposition in front of other deposition methods | 23 |
| 4.2. Current status and further challenges of ALD..... | 28 |
| 5. PRECURSORS..... | 29 |
| 6. COMPOSITION AND PRIMARY EVALUATION OF CMOS/DRAM MATERIALS | 32 |
| 6.1. Doped high-k oxides | 35 |
| 6.2. Nanolaminates..... | 37 |
| 7. THIN FILM GROWTH PROCESSES EXAMINED IN ARTICLES INCLUDED IN THIS THESIS | 38 |
| 8. GROWTH RATE, STRUCTURE AND CHARACTERIZATIONS..... | 40 |
| 8.1. Growth per cycle | 41 |
| 8.1.1. Growth of undoped films | 41 |
| 8.1.2. Growth of nanolaminates and doped films | 43 |
| 8.2. Morphology and conformal growth of thin films..... | 46 |
| 8.3. Structure | 52 |
| 8.3.1. Structure in doped films | 54 |
| 8.3.2. Structure of nanolaminated films | 56 |
| 8.4. Composition..... | 58 |
| 8.5. Capacitance-voltage measurements | 60 |

| | |
|---|-----|
| 8.6. Capacitance-voltage measurements on metal-oxide-semiconductor (MOS) structures | 63 |
| 8.7. Capacitance-voltage measurements in metal-insulator-metal structures..... | 64 |
| 8.8. The Capacitance Equivalent Oxide Thickness..... | 65 |
| 8.9. Interface state densities | 67 |
| 8.10. Conduction mechanisms | 71 |
| 8.10.1. Conduction mechanism in MOS structures | 73 |
| 8.10.2. Conduction mechanism in MIM structures | 75 |
| 8.10.3. Conduction mechanism in nanolaminated structures | 77 |
| SUMMARY AND CONCLUSIONS..... | 79 |
| SUMMARY IN ESTONIAN | 81 |
| ACKNOWLEDGEMENTS | 83 |
| REFERENCES..... | 84 |
| PUBLICATIONS | 91 |
| CURRICULUM VITAE | 152 |
| ELULOO KIRJELDUS..... | 153 |

LIST OF PUBLICATIONS

This thesis is based on the following publications that are referred to in the text by their corresponding Roman numerals

- I. Kaupo Kukli, Jaakko Niinistö, **Aile Tamm**, Jun Lu, Mikko Ritala, Markku Leskelä, Matti Putkonen, Lauri Niinistö, Fuquan Song, Paul Williams, Peter N. Heys, *Microelectronic Engineering* 84 (2007) 2010–2013. Atomic layer deposition of ZrO_2 and HfO_2 on deep trenched and planar silicon.
- II. Jaakko Niinistö, Kaupo Kukli, **Aile Tamm**, Matti Putkonen, Charles L. Dezelah, Lauri Niinistö, Jun Lu, Fuquan Song, Paul Williams, Peter N. Heys, Mikko Ritala, Markku Leskelä, *Journal of Materials Chemistry*, 18 (2008) 3385–3390. Advanced cyclopentadienyl precursors for atomic layer deposition of ZrO_2 thin films.
- III. Kaupo Kukli, Jaakko Niinistö, **Aile Tamm**, Mikko Ritala, Markku Leskelä, *Journal of Vacuum Science and Technology B* 27 (2009) 226–229. Behaviour of zirconium oxide films processed from novel monocyclopentadienyl precursors by atomic layer deposition.
- IV. **Aile Tamm**, Kaupo Kukli, Jaakko Niinistö, Jun Lu, Mikko Ritala, Markku Leskelä. *IOP Conference Series: Materials Science and Engineering* 8 (2010) 012022. Properties of HfO_2 and $HfO_2:Y$ films grown by atomic layer deposition in an advanced monocyclopentadienyl-based process.
- V. Indrek Jõgi, **Aile Tamm**, Kaupo Kukli, Marianna Kemell, Jun Lu, Timo Sajavaara, Mikko Ritala, Markku Leskelä, *Journal of The Electrochemical Society* 157 (2010) G202-G210. Investigation of ZrO_2 - Gd_2O_3 based high-k materials as capacitor dielectrics.
- VI. **Aile Tamm**, Mikko Heikkilä, Marianna Kemell, Jekaterina Kozlova, Kaupo Kukli, Väino Sammelselg, Mikko Ritala, Markku Leskelä, *Thin Solid Films* (2010), doi:10.1016/j.tsf.2010.08.111. Atomic Layer Deposition and Characterization of Zirconium Oxide – Erbium Oxide Nanolaminates.
- VII. **Aile Tamm**, Marianna Kemell, Jekaterina Kozlova, Timo Sajavaara, Massimo Tallarida, Kaupo Kukli, Väino Sammelselg, Mikko Ritala, Markku Leskelä, *Journal of The Electrochemical Society* 157 (2010) G193-G201. Atomic layer deposition and characterization of erbium-doped zirconium oxide thin films.

PRESENTATIONS AT INTERNATIONAL CONFERENCES AND DOMESTIC DOCTORAL SCHOOLS

1. Kaupo Kukli, Jaakko Niinistö, **Aile Tamm**, Jun Lu, Mikko Ritala, Markku Leskelä, Matti Putkonen, Lauri Niinistö, Fuquan Song, Paul Williams, Peter N. Heys, “Atomic layer deposition of ZrO_2 and HfO_2 on deep trench and planar silicon”, INFOS 2007 – 15th biannual conference “Insulating Films on Semiconductors” June 20–23, 2007, Training & Conference Center of the National Mortgage Bank of Greece, Athens/Glyfada, Greece (poster presentation + oral introduction 3 min/3slides by K. Kukli).
2. **Aile Tamm**, Kaupo Kukli, Jaakko Niinistö, Mikko Ritala, Markku Leskelä, “Characterization of ZrO_2 and HfO_2 films grown by atomic layer deposition”, Doctoral School of Materials Science and Materials Technology, Conference, 19–20.02.2008, Kääriku Leisure and Sports Center, Valga county, Estonia (poster presentation by A. Tamm/K. Kukli)
3. **Aile Tamm**, Kaupo Kukli, Jaakko Niinistö, Mikko Ritala, Markku Leskelä, “Characterization of high permittivity oxide films grown by atomic layer deposition compatible to the applications on large area substrates” The European Materials Research Society (E-MRS) 2008 Spring Meeting, Symposium E: Thin film materials for large area electronics, Congress Center, Strasbourg (France), 26–30.05.2008. (poster presentation by A. Tamm).
4. Kaupo Kukli, Jaakko Niinistö, Maarit Kariniemi, **Aile Tamm**, Mikko Ritala, Markku Leskelä, “Behaviour of zirconium oxide films processed from novel monocyclopentadienyl precursors by atomic layer deposition” The 15th Workshop on Dielectrics in Microelectronics, WoDiM 2008, Bad Saarow (Berlin), Germany, 23–25.06.2008. (poster presentation by K. Kukli).
5. **Aile Tamm**, Kaupo Kukli, Jaakko Niinistö, Mikko Ritala, Markku Leskelä, “Properties of HfO_2 and $HfO_2:Y$ films grown by atomic layer deposition in cyclopentadienyl-based process”, European Materials Research Society 2009 Spring Meeting, E-MRS 2009, Congress Center Strasbourg, France, June 8–12, 2009, (oral presentation by A. Tamm).
6. Kaupo Kukli, **Aile Tamm**, Indrek Jõgi, Jaakko Niinistö, Mikko Ritala, Markku Leskelä, “Advanced atomic layer deposition routes to metal oxides”, European Materials Research Society 2009 Spring Meeting, E-MRS 2009, Congress Center Strasbourg, France, June 8–12, 2009, (poster presentation by K. Kukli)
7. Indrek Jõgi, **Aile Tamm**, Kaupo Kukli, Mikko Ritala, Markku Leskelä, “Atomic layer deposited $ZrO_2-Gd_2O_3$ mixtures and laminates for high-k applications”, Baltic Conference on Atomic Layer Deposition 2009, BALD

- 2009, Department of Materials Chemistry, The Ångström Laboratory, Uppsala University, Sweden, June 15–16, 2009. (poster presentation by I. Jõgi)
8. **Aile Tamm**, Kaupo Kukli, Mikko Ritala, Marianna Kemell, Jaakko Niinistö, Markku Leskelä, “Atomic layer deposition and characterization of rare-earth doped high-k thin films” Baltic Conference on Atomic Layer Deposition 2009, BALD 2009, Department of Materials Chemistry, The Ångström Laboratory, Uppsala University, Sweden, June 15–16, 2009. (poster presentation by A. Tamm)
 9. **Aile Tamm**, Indrek Jõgi, Kaupo Kukli, Jekaterina Kozlova, Mikko Heikkilä, Marianna Kemell, Timo Sajavaara, Jun Lu, Massimo Tallarida, Väino Sammelselg, Mikko Ritala, Markku Leskelä, “Atomic layer deposition and characterization of $\text{ZrO}_2\text{-Er}_2\text{O}_3$ and $\text{ZrO}_2\text{-Gd}_2\text{O}_3$ nanolaminates” Estonian PhD Student Conference on Functional Material and Science 2010, FMTDK 2010, Dorpat Conference Centre, Tartu, Estonia, February 25–26, 2010. (oral presentation by A. Tamm).
 10. **Aile Tamm**, Kaupo Kukli, “Aatomkihtsadestamise kasutamine tänapäeva mikro- ja nanoelektronika seadmetes” (ALD in micro- and nanoelectronic devices) Estonian LOTE PhD Student Conference 2010, Haanjamehe talu, Võru county, Estonia, May 11–12, 2010. (Oral presentation by A. Tamm).
 11. **Aile Tamm**, Indrek Jõgi, Kaupo Kukli, Jekaterina Kozlova, Mikko Heikkilä, Jun Lu, Väino Sammelselg, Mikko Ritala, Markku Leskelä, “Atomic Layer Deposition and Characterization of $\text{ZrO}_2\text{-Er}_2\text{O}_3$ and $\text{ZrO}_2\text{-Gd}_2\text{O}_3$ Nanolaminates”, Baltic Conference on Atomic Layer Deposition 2010, The Baltic ALD 2010 & GerALD 2, Hamburg, Germany, September 16–17, 2010. (oral presentation by A. Tamm).

THE AUTHOR'S CONTRIBUTION TO THE PAPERS FORMING THE BASIS OF THE THESIS

- Publication I The author analysed the results of electrical measurements (I-U and C-V) determining the conduction mechanisms and defect densities.
- Publication II The author analysed the results of electrical measurements (I-U and C-V) determining the conduction mechanisms and defect densities.
- Publication III The author analysed the results of electrical measurements (I-U and C-V) determining the conduction mechanisms and defect densities.
- Publication IV The author made all atomic force microscopy (AFM) and electrical measurements. The author interpreted the results and wrote the article.
- Publication V The author made part of the electrical measurements and assisted in their interpretation.
- Publication VI The author planned and made the film growth experiments and also the electrical measurements. The author did the experimental work excepted the high-temperature X-ray diffractometry (HTXRD), scanning electron microscope with focused ion beam (SEM-FIB), scanning electron microscope with energy dispersive X-ray spectrometry (SEM-EDX), Rutherford backscattering spectrometry (RBS) analysis. The author interpreted the results and wrote the article.
- Publication VII The author planned and made the film growth experiments and also the electrical measurements. The author did the experimental work excepted SEM-FIB, SEM-EDX, RBS and X-ray photoelectron spectroscopy (XPS) analysis. The author interpreted the results and wrote the article.

LIST OF ABBREVIATIONS AND ACRONYMS

| | |
|------------|--|
| AFM | – atomic force microscope |
| ALD | – atomic layer deposition |
| CVD | – chemical vapor deposition |
| CET | – capacitance equivalent oxide thickness |
| DLTS | – deep-level transient spectroscopy |
| DRAM | – dynamic random access memory |
| EDX | – energy dispersive X-ray spectrometry |
| EOT | – equivalent oxide thickness |
| GIXRD | – grazing incidence X-ray diffraction |
| GPC | – growth per cycle |
| HRTEM | – high-resolution transmission electron microscopy |
| HTXRD | – high-temperature X-ray diffractometry |
| HVM | – high volume manufacturing |
| FWHM | – full width at half maximum |
| MBE | – molecular beam epitaxy |
| MIM | – metal insulator metal |
| MIS | – metal insulator semiconductor |
| MOSFET | – metal-oxide-semiconductor field-effect transistor |
| NMOS | – metal-oxide-n-type semiconductor |
| PMOS | – metal-oxide-p-type semiconductor |
| RBS | – Rutherford backscattering spectrometry |
| SWNT | – FET carbon nanotube field-effect transistor |
| SEM | – scanning electron microscope |
| SEM-FIB | – scanning electron microscope with focused ion beam |
| TEM | – transmission electron microscope |
| TMA | – trimethylaluminium |
| ΔG | – change in Gibbs free energy |
| XPS | – X-ray photoelectron spectroscopy |
| XRR | – X-ray reflectometry |

I. INTRODUCTION

The fundamental building blocks for all computer chips – transistors – have tracked with Moore’s Law for about forty years [1–3]. Those nanometric scale fundamental building blocks consist of thin layers of different materials. Thin layers or thin solid films are of course relevant to numerous applications in microelectronics, optoelectronics, sensory, and nanotechnology, as well as protective or biocompatible coatings. However, the most important exploiter of the films in the context of this study is semiconductor industry [4]. The industry has sought a new material for transistor gate dielectrics instead of silicon dioxide (SiO_2) for seven logic-process generations over the last 15 years. Hafnium dioxide (HfO_2) as one of the candidate materials has gained considerable attention at first because of its high permittivity (16–22), which is also the reason why HfO_2 and several other metal oxides are also called high-k materials. The dimensions of the transistors with its component layers have shrunked continuously throughout the generations. In this connection, the idea behind the replacement of SiO_2 namely stems from the necessity to find higher permittivity materials for capacitive structures. This is in order to keep the layer thickness higher than that allowing extensive tunneling currents through the dielectric layer and still keep or even increase the capacitance densities within the same or even decreased capacitor areas. Other values of HfO_2 are due to its large band gap (5.6–5.8 eV), related high breakdown field and low leakage currents, and – quite importantly – to sufficient thermodynamic stability on Si [5–7]. The significant breakthrough in solving the chip power problem took place namely upon identifying HfO_2 as an appropriate replacement for SiO_2 in both NMOS (n-metal-oxide-semiconductor) and PMOS (p-metal-oxide-semiconductor) transistors. Thus, HfO_2 has already substituted SiO_2 in metal-oxide-semiconductor field effect transistor (MOSFET) technology [1,2] and the method recognized and used for the growth of HfO_2 layers is called atomic layer deposition (ALD).

Regarding the development of materials suited to gate dielectric applications in silicon-based electronics, ZrO_2 has occurred inferior to HfO_2 in terms of its chemical stability on silicon, although ZrO_2 and HfO_2 are chemically and physically quite alike materials otherwise. In the case of ZrO_2 , reactions between the deposited materials and substrate, as well as solid-state reactions, are more favored and the regrowth of interfacial SiO_2 more likely than in the case of HfO_2 . However, because of similar band offset and somewhat higher dielectric constant of ZrO_2 compared to those of HfO_2 , ZrO_2 is apparently an advantageous material suited to dynamic random access memories (DRAM) formed on metal nitride or metal electrodes.

The high-k materials, especially ZrO_2 for DRAMs, must be deposited in the form of very thin films on structured surfaces. Herewith the self-limiting and surface-controlled growth mechanism characteristic to atomic layer deposition (ALD) facilitates the control of film thickness at the atomic level and allows

deposition on large and topologically complex surfaces. These features make ALD a very promising technique also for future integrated circuits which will be considered as a part of nanotechnology with devices more and more becoming three-dimensional. Indeed, ALD is currently one of the most rapidly developing and one of the most prospective fields of thin film technology [4–6, 8–11].

ALD of ZrO_2 and HfO_2 films has most often and traditionally been realized using metal chlorides [12–14]. As possible drawbacks regarding the applications, the films deposited with the traditional $ZrCl_4-H_2O$ and $HfCl_4-H_2O$ processes could incorporate some chlorine impurities, and the reaction byproduct, HCl, could also cause serious problems in the fabrication of microelectronic devices. In addition, both $ZrCl_4$ and $HfCl_4$ are solids with high evaporation temperatures and very fine particle sizes causing a risk that these particles may become transported onto the substrate and cause defects. Upon scale-up of the planar CMOS process, these problems have most likely been solved and appropriate techniques enable the exploitation of the chlorides as well. However, there are also non-planar applications, such as DRAM structures, where the thin layer of metal oxide must be deposited conformally and uniformly on three-dimensional substrates, i.e. into holes, pores, trenches or stacks with aspect ratio at least 1:20. Some works have indicated that the deposition of uniform thin films from chlorides on such substrates may be quite a complicated task and the corresponding experiments were not appreciably successful [15,16]. Also plasma-activated deposition processes may not assist in the fulfilment of the conformity requirements, because the plasma may not conveniently reach the bottom regions of the deep trenches. These issues initially motivated the search for alternative ALD precursors for zirconium and hafnium, such as cyclopentadienyls of these metals. Chemical vapor deposition (CVD) of ZrO_2 films dates back to 1999 [17], when the growth of ZrO_2 was realized and reported using Cp_2ZrMe_2 , $(MeC_5H_4)_2ZrMe_2$, and $(MeC_5H_4)_2Zr(BH_4)_2$, in where Cp is the cyclopentadienyl group, C_5H_5 , and $Me = CH_3$. The latter study, however, did not assume the exploitation of ZrO_2 for electronic purposes. ALD with cyclopentadienyl based compounds was started approximately in 2000 by dr. Matti Putkonen and prof. Lauri Niinistö in Helsinki University of Technology (nowadays Aalto University). Different ALD processes based on cyclopentadienyl-based chemicals have been described to date, such as those based on Cp_2ZrCl_2 [18], Cp_2ZrMe_2 [18], Cp_2HfCl_2 [19], Cp_2HfMe_2 [19], $(CpMe)_2HfMe_2$ [20], $(CpMe)_2Hf(OMe)_2$ [20], $(CpMe)_2Hf(OMe)Me$ [20], $(CpMe)_2ZrMe_2$ [21] and $(CpMe)_2Zr(OMe)Me$ [21]. Cyclopentadienyl-based processes have also been compared to some alternatives, such as those based on beta-diketonates, e.g. $Zr(thd)_4$, where thd = 3,3,5,5-tetramethylheptane-3,5-dionate [18]. Cyclopentadienyls have proven their value in producing chemically quite pure ZrO_2 and HfO_2 films with either water or ozone as the oxygen sources. These precursors have sufficient thermal

stabilities, and provide good structural and dielectric properties of resulting thin films [21–23].

Although both ZrO_2 and HfO_2 have relatively high dielectric constants compared to SiO_2 or SiON_x , their dielectric permittivity is phase-dependent [24], e.g. metastable cubic and/or tetragonal ZrO_2 possess considerably higher permittivity compared to the stable monoclinic phase [25]. Thus the capacitive properties of $\text{ZrO}_2/\text{HfO}_2$ based devices might further become improved via stabilization of cubic/tetragonal polymorphs. Metastable polymorphs of ZrO_2 and HfO_2 may become stabilized in very thin films during the deposition process (ca. 2–20 nm), but these structures may not necessarily withstand thermal treatment procedures – they transform into monoclinic phase. It is possible to retain the metastable polymorphs in multilayers of different oxides, e.g. in $\text{ZrO}_2\text{-Ta}_2\text{O}_5$ nanolaminates [26], but the nanolaminated structures may not become suited to CMOS and DRAM technologies due to their high thickness. It is probably more straightforward to dope the ZrO_2 (HfO_2) thin films with foreign cations in order to keep the cubic lattice stable against annealing. For instance, HfO_2 has been combined with oxides of other metals against the transformation to monoclinic phase, exemplified by hafnium oxide stabilized by lanthanum [27] erbium [28,29], yttrium [30–32], cerium [33], dysprosium, gadolinium, erbium [34] and ZrO_2 with germanium [35] or lanthanum [36,37].

In this work, atomic layer deposition of ZrO_2 and HfO_2 films from different novel cyclopentadienyls was studied [I–III]. In order to stabilize the cubic/tetragonal phases of either HfO_2 or ZrO_2 , these dielectric materials were also combined with rare earth metal oxides like Er_2O_3 , Gd_2O_3 and Y_2O_3 [IV–VII]. Conformal deposition on three-dimensional substrates with aspect ratios of 1:60 [I–III] and 1:20 [VI,VII] was examined. Structural and electrical characterization of the resulting films was provided [I–VII].

2. STATEMENT

ZrO₂ and HfO₂ thin films can be grown from novel cyclopentadienyl-based precursors in normal laboratory conditions via surface-controlled reactions from gas phase to thicknesses in nanometer range with good conformality and process controllability. The films grown to thicknesses in the range of 5–15 nm crystallize dominantly in the form of cubic/tetragonal polymorphs. The contribution from monoclinic phase increases fast with the further increase in thickness and also upon annealing, being essentially more significant in HfO₂. After mixing with rare earth metal oxides, the metastable phases become stabilized in both oxides. The capacitors based on ZrO₂ or HfO₂ dielectrics in their pure form are good insulators with high permittivity. Capacitors based on ZrO₂ or HfO₂ either doped or nanolaminated with rare earth metal oxides like Er₂O₃, Gd₂O₃ and Y₂O₃ demonstrate either higher capacitance or better insulating properties with low leakage current density compared with pure ZrO₂ or HfO₂. Cyclopentadienyls of hafnium and zirconium studied are prospective precursors and can be used at least in the production of capacitor dielectrics.

3. WHY DO WE NEED THIN FILMS

3.1. Some potential applications fields of nanometric thin films

Devices in micro- and nanoelectronics consist, either entirely or partially, of thin films. For instance, capacitors may be regarded as thin film stacks consisting of two metal electrode layers on both sides of a dielectric layer. Another example, carbon nanotube field effect transistor (CNT-FET) does contain a base structure – the carbon nanotube – which is not a film, although can be fabricated by thin film deposition methods (CVD). Nevertheless, these nanotubes are to be either back-gated or top-gated by first depositing a dielectric layer, e.g. HfO_2 or ZrO_2 . Nanodot-based devices, such as nanoflash memories, can serve as yet another example. Nanodots can well be grown using thin film technologies, such as CVD or ALD, making an advantage of the nucleation and island growth at the very early stages of the film deposition process. After formation of the dots distributed with certain lateral density on some kind of thin tunneling oxide film, these dots have again to be covered with a thin insulating metal oxide charge stopper layer. In general, while constructing nanoscale devices, each of the constituent layers should be very thin and as uniform, dense, structurally defined, and defect-free as possible. The deposition should be carried out using a method most uniformly covering the devices by functional layers with the deposition rate and film thickness precisely controlled at subnanometric level. Herewith the ALD process is the one being intrinsically atomic in nature, as it is based on subsequent deposition of monomolecular layers of the precursors, controlled and limited by the substrate surface only, not by the transport and nucleation in gas-phase, Thereby ALD often provides appreciably qualified deposition of films with excellent conformality [38] eligible for several applications. In this connection, the application of ALD to nanofabrication strategies and emerging nanodevices has sparked a good deal of interest due to its inherent benefits compared to other thin film deposition techniques [5,6,10–12,39]. Figure 1 represents some potential application fields of ALD ranging from nanotube-transistors to solar cells. In the case of all potential applications, the choice and selection of the precursors may appear as quite a critical issue: the precursors exploited in the deposition process must enable the growth of thin films in submonolayer-by-submonolayer mode, without their thermal decomposition causing poor thickness and thickness uniformity control.

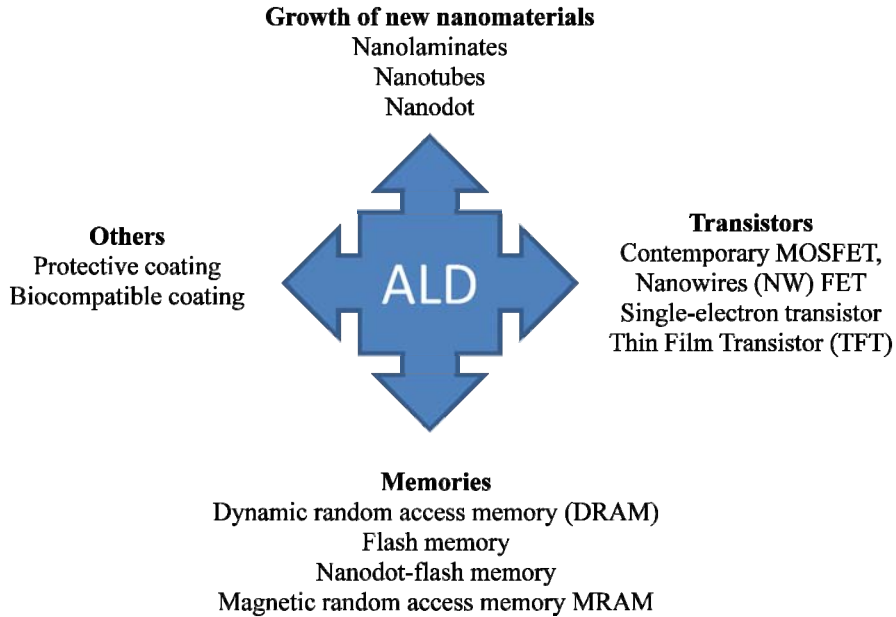


Figure 1. Schematic and non-exhaustive representation of current or potential application fields for atomic layer deposition method.

The precursors must be highly reactive, i.e. allowing fast surface reactions at relatively low temperatures and without large amounts of chemical residues in the solids deposited, otherwise quite common for chemical growth methods. The chemical residues should not harm the quality of the devices, e.g. the residual chlorine, carbon or hydrogen should not essentially affect the quality of contacted substrates or other functional layers neither should they strongly influence the electrical performance of the (dielectric) layer itself. While investigating new precursors for certain purposes, e.g. cyclopentadienyls for DRAMs as it has been done within this thesis, one should also keep in mind possible applications elsewhere. Evaluation of the chemical and physical qualities of the particular layers deposited and measured would thus possibly direct a reader to the alternative fabrication routes to other devices.

3.2. Silicon-based nanoelectronics

The most important exploiter of thin film technology in the context of the present thesis work is the semiconductor industry. Silicon-based CMOS technology has, from the very beginning of the production of chips been based on the exploitation of SiO_2 (and later SiON_x) as the “heart of the transistor” –

the gate dielectric oxide [40]. As implied above, the change in the generations of silicon-based microelectronics has required the replacement of SiO₂ with high-k materials. Intel is, currently, probably the only company admitting the use of hafnium-based high-k oxides (HfO₂) in transistors, starting from November 2007 [1]. The details of the process chemistry are not directly revealed, though. Intel keeps promising to follow the Moore's Law even beyond the 32 nm technology node and production of high performance, low power consumption and lower cost transistors [2,3,41]. The engineers of Intel realized that introducing hafnium oxide into silicon-based chips allows one to reduce electrical leakage currents enabling smaller, more energy-efficient and performance-packed processors [42]. Such actions have already provided significant performance improvements over the previous-generation processors, delivering new levels of functionality to the end-users on the new 32 nm technology node. [41,43].

It may become true, that the current planar Si-based CMOS-FET technologies are well-established and the further development of the silicon-based transistor generations will not necessarily require an introduction of any novel precursor chemistry, such as that based on the cyclopentadienyls. One has also to take into account that the actual scale-up of any process suited to the production of devices to be actually sold in the market would require years of the research and development, including preparative marathon runs. If the relatively novel three-dimensional transistor concepts, such as FinFETs, will not initiate an interest in novel process chemistry, the research on diverse ALD processes such as those based on cyclopentadienyls might have a relatively little practical value. However, there are other applications, which may require an active research on new precursor compounds.

3.3. Graphene-based nanoelectronics

Graphene may be regarded as one of the most prospective materials which may replace the silicon-based channels in future transistors. The discovery of graphene with its superior electron transport properties in mechanically exfoliated sheets or epitaxial graphene grown on SiC substrate has generated enormous interest in that material in both academy and industry [44,48]. Graphene is essentially a sheet of hexagonally bonded carbon atoms, a two-dimensional crystal, which exhibits superior electron transport properties with a velocity of 10⁸ cm/s and a room-temperature mobility of >15 000 cm²/V·s. In the future, it may occur possible to deposit graphene sheets reproducibly on large areas, making it fast compatible to lithographical procedures and in this way enable the high volume manufacturing (HVM) of nanoelectronic devices. This can not necessarily and that easily become realized in the case of more "classical" nanostructures such as nanotubes, nanowires or nanobelts. In the latter cases, reliable reproduction of the structures mentioned requires the

establishment of a process enabling the reproduction of the respective base configurations with well-defined diameter, length, and growth direction, i.e. some important process-related qualities which may not appear quite that much imperative in the case of graphene. The (chemical vapor) deposition of graphene over large substrate areas is, however, one of the current challenges [49,50] and reliable solutions are sought actively. Another and almost an equally important challenge is connected to the growth of other functional materials on graphene, especially when considering the importance of the top-gating of graphene-based switches or transistors. These gate materials in the context of graphene-related devices are currently supposed to contain basically the same metal oxides as those either explored or already actually used in connection to the silicon-based electronics. ALD has been used in order to grow gate dielectrics based on Al_2O_3 [47], and HfO_2 [48,51] on graphene. These graphene-related studies were mostly based on the exploitation of hafnium alkylamides as the HfO_2 precursors on pre-functionalized carbon. There are, however, some implications that the HfO_2 may grow on graphene even without the functionalization, such as in the study devoted to the ALD of HfO_2 on graphene using two different deposition temperatures and using the most traditional hafnium precursor, i.e. the hafnium tetrachloride [52]. Other hafnium (or zirconium) precursors have not yet been studied in connection to the very frontier nanoelectronics, and that should be kept in mind also when looking for new application areas for cyclopentadienyls.

3.4. Other low-dimensional nanomaterials

The most easily and inherently fabricated nanomaterials by ALD are nanolaminates, i.e. "sandwiched" structures or multilayers consisting of ca. 1–20 nm thick single layers of different materials deposited on each other, e.g. ultrathin Al_2O_3 films deposited alternately with ZrO_2 , or Al_2O_3 grown alternately with TiO_2 , ZrO_2 with SiO_2 , *et cetera*. Also the gate oxides or memory capacitor insulators with improved electrical properties were often fabricated as nanolaminates by ALD and studied accordingly [11,53,54,58] In such kinds of nanolaminates consisting of different metal oxides, the dimensions of those constituent oxide layers (distinct in terms of their chemical composition) are limited to a few nanometers along the normal to the substrate surface, which also may open up the possibilities to stabilize crystallographic phases uncommon in the bulk materials under normal conditions. The layers constituting the nanolaminates might be recognized as two-dimensional (2D) elements of the nanostructures.

Nanomaterials with even lower dimensions, especially one-dimensional (1D) nanotubes [59,60], nanowires [61], nanobelts [62] as well as the so-called zero-dimensional (0D) nanodots [63], are considered as potential building blocks of the future nanotechnological devices. ALD is not very common method for the

fabrication of 1D and 0D cores of the nanodevices, but can still be used in special cases for the growth of nanodots [63,64] and nanorods [65]. The low dimensional nanomaterials like carbon nanotubes are currently used to build the prototypes of single-wall carbon nanotube field-effect transistor (SWNT-FET). The ALD process enables the growth of gate insulators with high capacitance while being chemically begin to nanotubes, which is a key to the integration of advanced dielectrics into low-dimensional electronics. The memory or switching elements containing gate dielectrics on nanotubes to date also included ZrO_2 [59] or HfO_2 [60]. These oxides were grown by ALD using metal halides (tetrachloride) or alkylamides. It is to be noted, that the behavior of carbon nanotube based devices is not dependent only on the predicted conductive properties of the tube, but also on the quality of the gate oxide layer deposited around the tube. Also the oxide deposition process may or may not affect the electronic quality of the ballistically transporting channel, i.e. the CNT. Since the CNT-based devices are not yet upscaled and even not well defined the choice of the appropriate precursors for complementary high-k materials (which may well be ZrO_2 and/or HfO_2) is, most probably, still open.

3.5. Dynamic Random Access Memories

The development of Dynamic Random Access Memories (DRAM) has been analogous to that of transistors and processors [66] in terms of shrinking the device dimensions and consequent transfers between 90 (reached for 2003, 50 nm length), 65 (2005, 30 nm Prototype), 45 (2007, 20 nm Prototype), 32 (2009, 15 nm Prototype) nm and further nodes: 22 (2011, 10 nm Prototype), 16 (2013) nm [67–71]. However, the transistors in the processors are still produced using planar silicon technology, whereas the new 3D transistor concepts such as A Self-Aligned Double-Gate MOSFET (FinFETs) [73, 74] are still at prototype level and to be scaled up. At the same time, contemporary DRAMs can be considered as matrix of cells consisting of switching transistor and 3D capacitor storing the bits (Figure 2). The capacitor in the cell is planar either in the form of narrow hole etched in the silicon below the wafer level before the transistor (trench) or silicon-based hollow column fabricated above the wafer level after the transistor (stack) [75, 76].

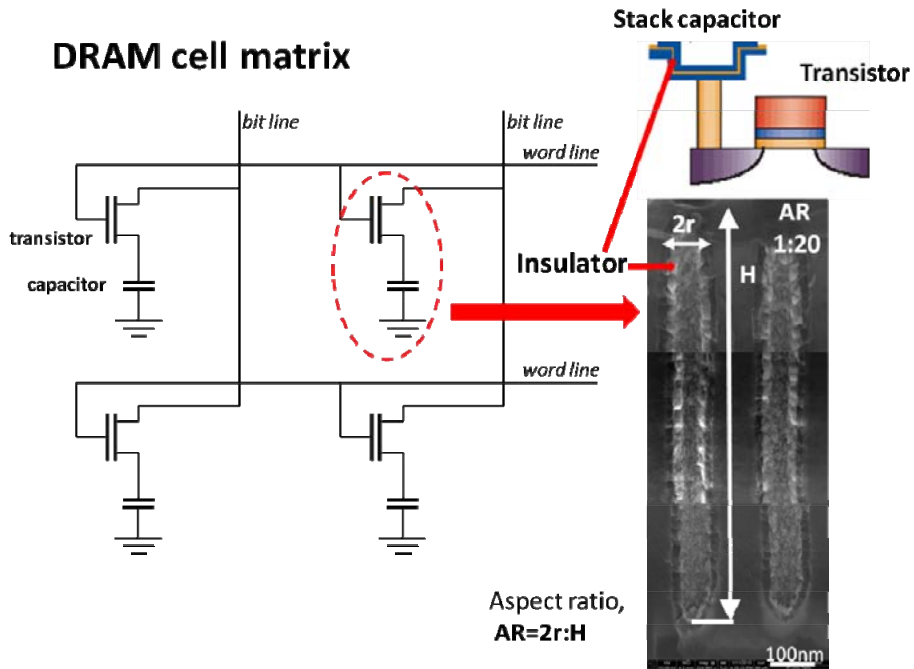


Figure 2. Schematic representation of DRAM cell matrix with three-dimensional capacitors. The high-k dielectric ZrO_2 is deposited on the stack capacitor structure with aspect ratio 1:20.

In such a capacitor, the (conductive) surface of the trench or stack, possibly covered with a metal film, works as bottom electrode, the dielectric material is to be deposited uniformly over the 3D surface, and then the top electrode should also be deposited in the form of uniform metal or metal nitride film on the dielectric layer. Currently the generations developed are more based on stack (or pillar) configurations [76]. This kind of configuration allows one to effectively use the wafer area and minimize the lateral dimensions of a single capacitor still notably increasing the electrode area and consequently the capacitance (density). The narrower and deeper the 3D holes the higher the lateral density of capacitors and the capacitance value. Trenches and stacks are characterized by aspect ratio, which is the ratio between the diameter of the hole to the depth of the hole. Exploitation possibilities of the trenches were actively investigated up to the aspect ratios 1:90 or 1:100. Stack prototypes also used in this study are with lower AR in the order of 1:20. Upon increase in aspect ratio, further deepening the holes, and keeping the diameter of the hole within some tens of nanometers, the uniform deposition of both metal and dielectric layers on the walls of the hole becomes more and more complicated. Most of the thin film deposition methods are not capable to meet that challenge.

The candidate materials for the dielectric layers for DRAMs are or have been essentially the same as those earlier explored as gate oxides – TiO_2 , Ta_2O_5 , Al_2O_3 , HfO_2 , ZrO_2 [67,74,77,78]. For further generations, materials of even higher permittivity are investigated, such as perovskites SrTiO_3 or $(\text{Ba,Sr})\text{TiO}_3$. The capacitance density can be increased and/or dielectric layer thickness decreased, when applying materials with higher dielectric constants. ZrO_2 -based films and also ZrO_2 films alternately layered with Al_2O_3 [66] can nowadays be considered as base materials on which the actual memories are produced. As DRAMs keep evolving in the direction of three-dimensional structures with increasingly high aspect ratios (1:20, 1:60 etc.) the surface-controlled growth as an inherent property of ALD would allow one to follow the increasing demands for conformal deposition, still producing films with appreciable chemical purity, smooth surface and dense structure. Actually, ALD may be the only method capable to meet those challenges in the end. An essential prerequisite for the realization of film growth on three-dimensional structures with appreciably high step-coverage (SC) is the appropriate selection of the chemical precursors able to diffuse quickly into the 3D holes without thermal decomposition and providing high nucleation density. Step coverage is basically the similarity in film thickness at the bottom or top of the 3D hole compared to that at the wafer level, and should approach 100%.

The search for the novel materials and/or precursors of the materials suited to the DRAM technology continues. ALD with new cyclopentadienyl-based chemicals and either water or ozone as HfO_2 and ZrO_2 precursors has appeared as a promising process resulting in conformal films with defined crystallographic structure as trenched substrates [79]. More recently, attempts have been made to stabilize higher-permittivity phases of ZrO_2 by doping ZrO_2 with foreign metal oxides keeping in mind the suitability for DRAMs [66,80,81]. This thesis work is also mainly devoted to the evaluation of HfO_2 and ZrO_2 -based films processed using cyclopentadienyl precursors with the first aim at proving their validity as potential DRAM capacitor dielectrics, still not forgetting the possible applications elsewhere.

4. THIN FILM DEPOSITION TECHNOLOGY

4.1. Atomic layer deposition in front of other deposition methods

There exists a variety of physical and chemical thin film deposition methods, such as molecular beam epitaxy (MBE), sputtering, electron-beam evaporation (EBE), pulsed laser deposition (PLD), as physical methods, and spray pyrolysis, sol-gel deposition, chemical bath deposition (CBD), chemical vapor deposition (CVD), as chemical methods. The major difference between physical and chemical methods is based on the fact that in the case of physical methods, the precursors consist of the same elements as the resulting film, and the film is deposited without chemical exchange or decomposition reactions. In the case of chemical methods the precursors contain molecules with ligands and substitutes which contain also chemical elements not contributing to the target composition of solid films – the deposition process proceeds via chemical exchange reactions and/or thermal decomposition. Due to the ligands, which partially remain as impurities, chemically deposited films are inferior to physically deposited ones in terms of chemical purity. On the other hand, chemical deposition is superior to physical deposition in terms of conformal growth on large areas. ALD has common features with two very different methods, MBE and CVD. A physical method MBE is well suited to the layer-by-layer growth and sequential deposition of monatomic layers, since the elemental precursors can be evaporated and deposited alternately. The origin of ALD may well lie on MBE technique. However, since the ALD is a chemical gas-phase deposition method commonly exploiting precursor molecules with ligands, it is nowadays most often regarded as a “special modification of CVD”. CVD method is indeed a very widely recognized thin film deposition technique [82], used to produce high- performance solid materials and thin films. CVD can exploit different chemicals which are evaporated and transported into reactor simultaneously in carrier gas flow, reacting with moderate rate already in gas phase and diffusing to the substrate surface. Frequently, volatile by-products are also produced, which are removed by gas flow through the reaction chamber. With CVD, it is possible to produce most metals, many nonmetallic elements such as carbon and silicon as well as a large number of compounds including carbides, nitrides, oxides, intermetallics, and many others. This technology is now an essential factor in the manufacture of semiconductors and other electronic components, in the coating of tools, bearings, and other wear-resistant parts and in many optical, optoelectronic and corrosion applications [82].

The essential property of ALD, distinct from CVD, is that film growth takes place in a stepwise, cyclic manner [38]. In ALD, exchange reactions proceed only on substrate surface between alternately adsorbing precursors, not in the gas phase, upon alternate exposure of the surface to precursor flows. Normally

one growth cycle consists of four steps: 1) exposure to the first precursor, 2) purge of the reaction chamber, 3) exposure to the second precursor, and 4) the second purge of the reaction chamber. The growth cycles are repeated as many times as required for the desired film thickness. Due to the fact, that the precursors are separated by purge periods, aggressively reacting chemicals can be used, i.e. those which can not be used in CVD. This allows the processes conducted also at rather low temperatures. The (metal) precursor adsorbs during the first exposure time (0.2–20 s) on an active, quite often hydroxylated, surface. Provided that the precursor does not decompose thermally in the gas-phase resulting in uncontrolled deposition, or do not etch the film already deposited, the adsorption process is then self-limiting, i.e. the surface receives only one (sub) monomolecular layer of the precursor at a time, because a precursor does not adsorb on itself and does not react with itself. During the second exposure, which in the case of metal oxide growth means reactions of the metal precursor with a selected oxygen precursor (H_2O , H_2O_2 , O_2 , O_3), another (sub) monolayer of the target material grows on the surface. The amount of film material deposited in each reaction cycle is supposed to be a constant. Thus each reaction cycle adds a certain amount of the target material to the surface, referred to as the growth per cycle (GPC) [83]. Commonly, the growth rate (growth per cycle) of the film is back-calculated after measuring the thickness of the films by X-ray reflectance (XRR), UV-VIS spectrometry, ellipsometry, X-ray fluorescence (XRF), Rutherford backscattering spectrometry (RBS) or other means, and dividing the result by the amount of growth cycles applied. The film growth rate in the case of ALD is in any case routinely expressed either in nm/cycle or Å/cycle units, instead of directly using time units.

Depending on the process chemistry, complexity of substrates, and the reactors used, the duration of a single deposition cycle can vary between a couple of seconds and a few minutes, and may provide the films growing with averaged rates between 0.02 and 0.15 nm/cycle. Even higher growth rates would already imply the thermal decomposition of the precursor, which enhances the apparent growth rate but usually on the expense of the precision of the thickness control. An appropriate length to be chosen for the cycle times strongly depends on the rate of the film-formation reaction, i.e. on the reactivity of the precursors chosen. In addition, the optimized cycle times may, in practice, depend on the topology of the substrate to be covered with the film. For instance, 3D substrates such as deep trenches for DRAMs with aspect ratio up to 1:90 may well require the application of pulse and purge length ca. ten times longer compared to those providing flat films on planar silicon within a few seconds [I]. In not so deep trenches like AR = 1:20 coverage may be accomplished even with the same pulse and purge times as for planar substrates [VI, VII].

The growth per cycle is quite a critical parameter. The main drawback related to any ALD process has always been the low growth rate inherently

characteristic of ALD. Roughly within several tens of seconds, only two-three nanometers of a solid material can be deposited. Taking into account that high rate of the deposition means reduction in the processing time and, therefore and most importantly, the cost of the process, ALD has always met challenges when competing with much quicker deposition processes such as CVD and variations of PVD. The latter methods allow depositions of thin films with absolute rates in the range of several nanometers per second. However, in the case of the deposition of ultrathin and dense films at low temperatures in the thickness range of 2–20 nm, especially on 3D substrates, ALD has often proven itself as a method superior to the rest of the known methods. Moreover, in special cases, such as in the case of the production of high-quality flat-panel electro-luminescent displays, the eventual quality of ALD-processed films has in the past had a decisive importance, although the growth of dielectric-phosphor-dielectric stack to thickness about 1 μm may have required days and weeks of the processing time [84]. Nonetheless, one should carefully consider the growth rates in the case of any new process nowadays to be introduced in the contemporary and future electronics or optics. Regarding the relatively thick films in the form of nanolaminates, i.e. periodical multilayered structures consisting of several oxide layers of distinct chemical composition, the knowledge on the growth rates of constituent oxides is most important, since the growth rates lower for any of the constituents would significantly decrease the average growth rate of the whole stack.

As already mentioned, in ALD one can make use of as aggressive net reactions as possible, i.e. those strongly spontaneous with as large negative change in free energy (Gibbs energy, ΔG), as possible [38]. This is not advantageous in CVD, in where the precursors should react with a moderate rate in gas phase in order to enable the efficient transport of nuclei to the substrate surface by the carrier. It is already understood, that ALD is probably the slowest among the advanced film growth methods, owing to the cyclewise deposition of monolayers with the single cycle lengths/times in the order of several seconds or even minutes, and with the total film thickness determined by the number of such cycles. Nevertheless, the high reactivity of precursors chosen is the first criterion relevant before the high growth rate or growth per cycle. Further, the film thickness obtained per cycle, i.e. the growth rate, can also depend on the size of the precursor molecule, because the steric hindrance may put additional limitations to the number of molecules capable to adsorb and subsequently react on the surface. In addition, the number of adsorption sites at the surface also affects the amount of molecules adsorbed. Ideally, each exposure and purge step in ALD is complete, in terms of the completion of the exchange reactions on the surface and removal of excess reactants/byproducts, respectively. Quite commonly, H_2O is used as oxygen precursor in ALD of oxides, which makes alternate hydroxylation, adsorption of precursor molecules at active $-\text{OH}$ sites and rehydroxylation of the oxide surface an inherent property of the process. However, the surface density of those active adsorption

sites (-OH) is rather sensitive to the substrate temperature, with the tendency for the surface to dehydroxylate at increasing temperatures and during longer purge periods. This makes the growth rate also somewhat sensitive to the temperature, which means that the film growth rate changes when temperature is changed and the so-called perfect ALD “temperature-windows” [38] are seldom observed. Probably the best criterion of self-limited growth and well-defined ALD is the saturation of the growth rate against extension of the metal precursor pulse length, i.e. the insensitivity of the growth per cycle to the exposure time. The latter always proves that the precursor does not decompose thermally and the deposition on surface is controlled by the surface only.

An adsorption process typical for ALD is schematically shown in Figure 3, representing the growth of ZrO_2 from a cyclopentadienyl-type precursor $\text{Cp}_2\text{Zr}(\text{CH}_3)_2$ and deuterated water [79]. It should be noted that the scheme drawn is oversimplified and in 3D space the formation of bulk ZrO_2 is a more complex. In addition, the steric hindrances caused by the bulkiness of the cyclopentadienyl ligand affect the growth rate, and as a result, only a distinct fraction of a monolayer is formed during one growth cycle. Typical growth rates for cyclopentadienyl-based processes lie in the range of 0.04–0.07 nm/cycle over a wide deposition temperature range from 250 to 350°C [21,85,86]. Such a growth schematics may be considered as relevant to the films grown also in other cyclopentadienyl-based processes treated within this thesis work. It is to be noted that ozone is often used instead of water as oxygen precursor. In such cases, the formation of hydroxyl sites on the surface may not be significant and the precursor has to adsorb mainly on oxygen sites. However, ozone is essentially more active precursor than water, and may reduce the steric hindrance. Thus, the growth rates in water and ozone based processes in the case of cyclopentadienyls do not differ markedly.

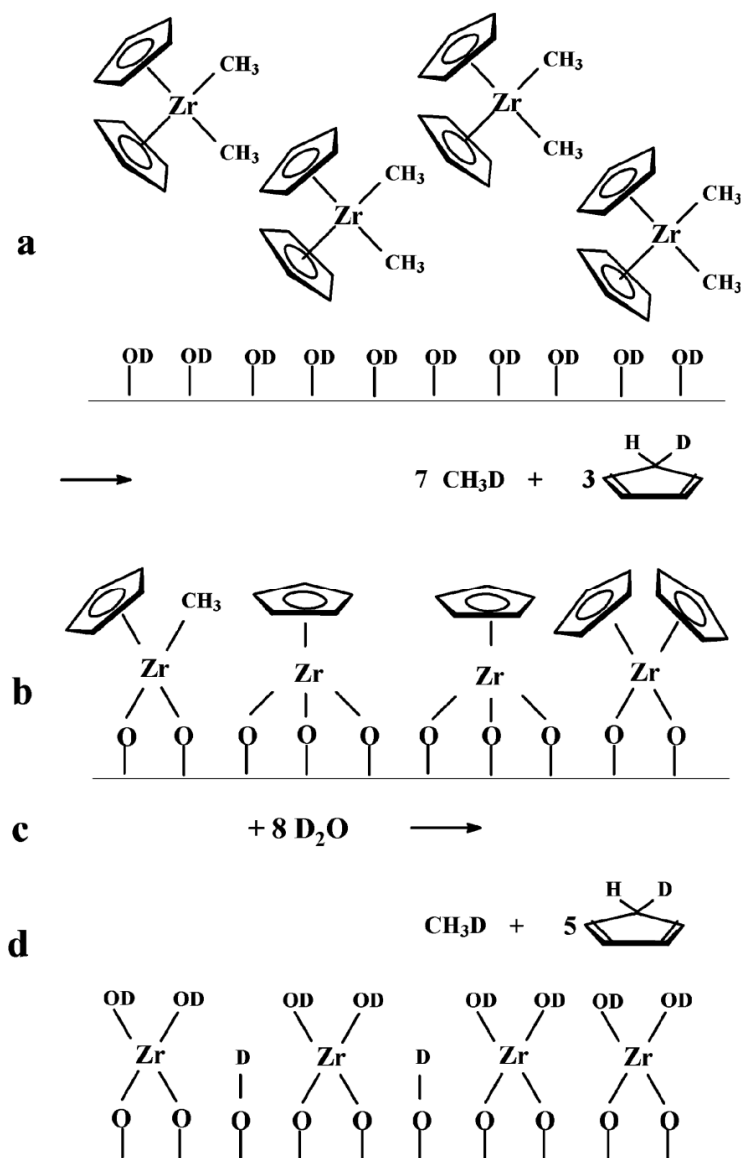


Figure 3. Cp-in-situ. Proposed reactions between $\text{Cp}_2\text{Zr}(\text{CH}_3)_2$ and activated (deuterated) surface in an ALD process at 350 °C [79]. The ALD cycle consists of (a) metal precursor pulse on the OD-terminated surface, (b) metal precursor adsorbed and CH_3D and CpD released, (c) inert gas purge and D_2O pulse, and (d) CH_3D and CpD released, the surface converted back to OD-terminated, followed by the inert gas purge, leaving the surface ready for the next ALD cycle. Deuterium was used in this study in order to follow the reactions by mass-spectrometer, separating the oxygen precursor from humid and residual water in the reactor. The Figure is reprinted by the permission of American Chemical Society.

4.2. Current status and further challenges of ALD

In the mid 1990s, rapidly increasing interest towards ALD has originated from the silicon based microelectronics. This is a consequence of the ever decreasing device dimensions and increasing aspect ratios in integrated circuits (IC). ALD has been selected by Intel as the method capable to grow uniform and dense ultrathin HfO₂ layers over large areas, i.e. on two-dimensional 300 mm diameter silicon wafers at relatively low processing temperatures (< 400°C). These achievements have further increased the attraction to the ALD method in the IC industry [11,42,71].

The developed and also sold generations of IC technologies are mostly based on the growth of thin films on planar silicon, apart from the current 3D DRAM generations. However, the future plans for the transistor development also foresee the exploitation of 3D-based concepts, especially those related to either FinFETs or nanotube-based switches. The explorations of the materials suited to the applications in memory devices are also directed to the finding of processes able to provide conformal growth on structures with more and more demanding aspect ratios. In this regard, ALD has the capability to coat extremely complex shapes with a conformal material layer of high quality, a capability unique among thin-film deposition techniques [87], and therefore the application areas of ALD can only become widened in the future. It is important to note, that the required thickness of the films has, in many cases, decreased to the order of a few nanometers and therefore the main drawback of ALD, the low deposition rate, is becoming less important.

Today, there are ALD reactors available from several tool suppliers. Some of these reactors can utilize gas, liquid, and solid precursors, having from two to ten sources that can be used simultaneously. This enables the deposition of a variety of different materials including ternary compounds and multilayer film stacks, which is a great advantage considering the R&D requirements. Nevertheless, it is noteworthy that each of the process chemistries exhibits individual requirements for the reactor design. In practice this means that some reactors are more compatible with some process chemistry than others, and the reactor hardware must often be optimized to a particular process chemistry [88]. High-volume manufacturing (HVM) does put demands on the quality of thin films, including film uniformity on large substrate areas, but even most importantly on the repeatability and reproducibility of the depositions. Because the uniformity requirements are becoming more and more demanding, it is important to have a good understanding of the ALD processes [89] using ALD-friendly precursors. Appropriately chosen process conditions are considered as the essential part of the research and development in the future.

5. PRECURSORS

A variety of chemicals have been investigated as potential ALD precursors [11,38,39,85]. A good precursor is the most important component of a good ALD process [38]. General requirements for reactants used in ALD comprise sufficiently high volatility and stability against thermal decomposition at the evaporation and ALD process temperatures, respectively. The gas-solid reactions of the reactants have to fulfill the criterion of self termination also in the sense that the precursors should not etch underlying substrate or film material. Also practical aspects, such as cost, safety and economical requirements are important. In addition, liquid or gaseous precursors are generally preferred over the solid ones due to the more convenient delivery in the reactor, absence of particles arising from the precursor powder, and higher vapor pressures.

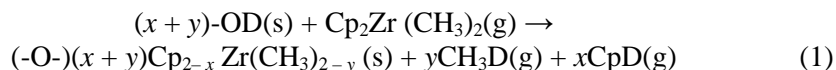
ALD processes have been developed for many types of solid inorganic materials: oxides, nitrides, sulphides, selenides, tellurides, pure elements, and other. Among the different types of inorganic materials grown by ALD, oxides have probably been the most frequently and thoroughly investigated ones. Oxides have been grown from precursors for alkaline earth metals, transition metals, lanthanoids, and group 13–15 elements. Herewith ZrO_2 and HfO_2 have been grown by ALD using halogenides (halides), alkoxides, alkylamides and cyclopentadienyls of zirconium and hafnium. The oxygen source in oxide deposition has most typically been water H_2O , but also diatomic oxygen O_2 , ozone O_3 , alcohols ROH (where R stand for alkyl groups), or atomic oxygen created through oxygen plasma have been often examined. Somewhat less common oxygen sources are $\text{H}_2\text{O}+\text{catalyst}$, H_2O_2 , N_2O , NO_2 , N_2O_4 , and metal alkoxide reactants in the case of nonhydrolytic ALD reactions between e.g. ZrCl_4 and $\text{Zr}(\text{OC}_2\text{H}_5)_4$ [90]. The first Hf and Zr precursors and oxygen sources ever applied in ALD were halides of these metals and water, respectively [91,92]. It is likely that the same precursor combination is also the one crucial for the production of contemporary microelectronics. It is worth noting that the metal chlorides, incl. HfCl_4 and ZrCl_4 are probably the most universal ALD precursors in terms of the temperature range enabling the growth. These precursors do not decompose thermally and the substrate temperatures can extend from ca. 100 to almost 1000°C [13]. Other precursors, including cyclopentadienyls, do not compete with chlorides in this regard.

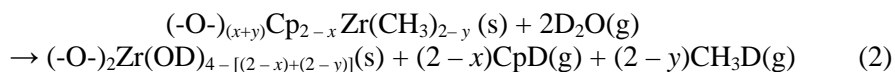
It is known that, in the Intel's processors, the transistor is gated after deposition of a hafnium-based high-k dielectrics [93]. This high-k material is either hafnium oxide, hafnium silicon oxide, or hafnium oxide containing nitrogen, while ALD was selected as the growth method [1]. Although the exact process details were not revealed, it is also known, that a reliable and advanced solid source delivery system has been developed by ATMI [94] enabling the particle free exploitation of solid HfCl_4 precursor in ASM's industrial-scale ALD reactors (Pulsar 3000), making the CMOS-processing using HfO_2 highly

reproducible. Regarding the other prospective hafnium precursor, an alkylamide Hf[N(CH₃)(C₂H₅)₄ tetrakis ethylmethyl hafnium (i.e. TEMAH), the higher impurity contents usually measured in such films have somewhat suppressed the considerations of TEMAH as competitor to HfCl₄ [94]. Herewith it is also possible, that the relatively late development of cyclopentadienyls may not any more enable the entrance of this precursor class in planar CMOS technology. However, in the case of other and preferably 3D technologies the chances for alternative processes are higher, and e.g. TEMAH is already considered as one of the most prospective precursors for DRAMs [77,78].

In this work the ALD of HfO₂ and ZrO₂ oxides grown from cyclopentadienyls is investigated. Cyclopentadienyls as a class of chemicals were introduced as ALD reactants in the early 1990s, for the deposition of MgO, Al₂O₃ and MgAl₂O₄ films [38,95] and have gained more popularity in the 2000s for deposition of HfO₂ and ZrO₂ oxides. Cyclopentadienyls also offer the possibility to use halide-free or assumptionally less corrosive precursors. Similarly to very highly reactive alkyls, cyclopentadienyls are organometallic, containing metal-carbon bonds. There are however, no alkyl precursors available for Zr and Hf. Cyclopentadienyls are reactive enough and for example, oxides can be grown through reaction with H₂O, in addition to O₃ [18,19,23,79,96,97] at reasonably low temperatures between 250 and 400°C. Another advantage of the cyclopentadienyl reactants is the fact that they can be synthesized also for rare earth metals, for which other compounds have been scarce [38]. This may later become useful for the doping and mixing of ZrO₂ or HfO₂ with other (rare earth) oxides in similar processes. We are interested only in the cyclopentadienyls of Hf and Zr in the framework of this study, though.

The optimum growth temperature range in the cyclopentadienyl-based process is narrower compared to the tetrachloride and the films grow with rates of 0.04–0.06 nm/cycle fluently increasing with substrate temperature in the range of 240–420°C [19,79,85,96,97]. Self-limitation of the surface reactions, as characteristic feature of the ALD process, and therewith the suitability of the use of cyclopentadienyls in ALD has been confirmed by the saturation of the growth rate against the length of metal precursor pulse time. High quality ZrO₂ films were grown with water or ozone as the oxygen source with acceptably high chemical purity (0.2–0.3 at. % H and C) [23,97]. The growth mechanisms of films in cyclopentadienyl-based processes have been studied in real time with quadrupole mass-spectrometry and with quartz crystal microbalances. In the case of Cp₂Zr(CH₃)₂-H₂O(D₂O) process the ALD regime was achieved in the substrate temperature range of 210–400°C by Niinistö *et al.* [79] and in the case of (CpMe)₂Zr(OMe)Me-H₂O, D₂O or O₃ at 350°C by Elam *et al.* [98] and Knapas and Ritala [99]. The studies also allowed the recognition of two-step ALD reaction cycle in the form of the following chemical equations:





In these papers, the studies on growth mechanisms revealed that, upon adsorption of Cp_2ZrMe_2 or $\text{CpMe}_2\text{Zr}(\text{OMe})\text{Me}$ on an $-\text{OD}$ -terminated surface, 90% (eq 1) of the methyl ligands left the surface after the D_2O pulse and 40% of the cyclopentadienyl ligands were released in deuterated form. Because the methyl ligand is expected to be extremely reactive, one could indeed assume that $\text{Cp}_2\text{Zr}(\text{CH}_3)_2$ would react with the surface $-\text{OD}$ groups via methyl ligands releasing all CH_3D during the metal precursor pulse. [79]. Rest of the ligands was released in deuterated form during the D_2O pulse, which also re-formed the $-\text{OD}$ terminated surface ready for the next ALD cycle (eq. 2). [79,99]. These studies have confirmed that the adsorption reactions in cyclopentadienyl processes are quite fast and high efficient, which makes these precursors promising for ALD applications.

6. COMPOSITION AND PRIMARY EVALUATION OF CMOS/DRAM MATERIALS

Materials with high dielectric constants and wide band gaps have played a central role in the research on alternative gate oxides for MOSFETs and capacitor dielectrics for DRAMs. Dielectric constants relate to the capacitance densities, whereas band gaps influence the films conductivity: the wider the gap, the better insulator. Unfortunately, the band gap width and dielectric permittivity tend to be inversely related, and it is already quite complicated to find novel materials with both high capacitance and low leakage for further device generations. When the values of the dielectric constants and the band gaps of several metal oxides were compared, it looked apparent that alumina, hafnia and zirconia along with lanthanide oxides would be the best candidates for high-k materials [5,27–30,100–103] (Table 1).

Table 1. List of some candidates for high-k metal oxide materials with their average dielectric constants and band gaps [100,103].

| Metal Oxide | K | Band gap, eV |
|-------------------------|----|--------------|
| Al_2O_3 | 9 | 8.7 |
| Y_2O_3 | 15 | 6 |
| La_2O_3 | 30 | 6 |
| TiO_2 | 80 | 3.5 |
| Ta_2O_5 | 26 | 4.5 |
| Gd_2O_3 | 14 | 5.3 |
| Er_2O_3 | 14 | 5.3 |
| ZrO_2 | 25 | 5.8 |
| HfO_2 | 28 | 5.8 |

The motivation for the deposition of the high-k oxides like Al_2O_3 , ZrO_2 , and HfO_2 came from the detrimentally high tunneling currents through the traditional SiO_2 MOSFET gate dielectric, when it became downscaled to a thickness of about 1.0 nm and below [5,100]. With high-k oxides, the gate dielectric layer could be made physically thicker still maintaining and ever increasing the capacitance density, thus lowering the tunneling current. A convenient measure for the capacitor dielectrics is its equivalent oxide thickness, EOT. EOT is the thickness of a fictional SiO_2 layer, which would provide the same capacitance density as the high-k layer grown, although the high-k layer is grown to notably higher thickness. The dielectric permittivity of SiO_2 is 3.9. A high-k material with dielectric permittivity of 25 (monoclinic ZrO_2), which is 6.4 times that of SiO_2 , can be grown to 6.4 times higher thickness as SiO_2 for the same capacitance. EOT can preliminarily be evaluated quite directly from the capacitance measurements on planar parallel-plate capacitor, by taking the relative dielectric constant in the simple capacitor

equation equal to 3.9. Then the thickness of the capacitor dielectric layer calculated from that formula is equal to EOT. EOT and the permittivity of the high-k material are related through the following equation [100,104]:

$$EOT = \frac{d_{high-k} \times k_{SiO_2}}{k_{high-k}} = 3.9 \times \frac{d_{high-k}}{k_{high-k}},$$

where d_{high-k} , k_{SiO_2} , k_{high-k} are the thickness of high-k layer, permittivity of SiO₂ and permittivity of high-k material, respectively. If EOT is determined solely from the accumulation capacitance and quantum mechanical effects are not taken into account, then another term CET – capacitance equivalent oxide thickness – is used, which yields just slightly higher values than the EOT. CET will commonly be used also in this study.

For future devices with high-k-based dielectrics EOT should be 1.0 nm or less, for example the 32 nm MOSFET generation requires EOT as low as 0.5 nm. At the same time the leakage currents should remain at the level of 10⁻⁸ A/cm² [3,10]. The same requirements are generally valid for DRAM development. However, even pre-cleaned silicon surface is easily oxidized during the growth of high-k, and a thin interface layer of SiO₂ or a mixture of SiO₂ and the high-k oxide is easily formed, which adds to the overall EOT. On the other hand, the Si–SiO₂ interface is commonly recognized as the best semiconductor–insulator interface. Therefore, to achieve an EOT of less than 1.0 nm with good electrical characteristics, a very thin, one-to-two monolayer thick interfacial SiO₂ layer should preferably be left between the silicon and the high-k oxide. Controlling such a thin SiO₂ layer is very challenging. The (re)growth of interfacial oxide is an issue also in the case of MOSFET concepts based on SiGe or III–V compounds, such as GaAs. In current and future DRAM generations, the dielectric layers are to be grown on nitride or metal electrodes, but even in this case the interface layers of graded composition may form and cause the increase in EOT.

Research on ALD of high-k gate oxides has earlier and for a long time mainly been focused on three basic precursor systems: Al(CH₃)₃/H₂O, ZrCl₄/H₂O, and HfCl₄/H₂O [39]. These systems have all yielded good results in an EOT range of 1–2 nm [5]. Despite many efforts processes much better than those mentioned above have not been found [10,11]. Studies on cyclopentadienyl-based ALD processes have to date been mainly devoted to the introduction and description of novel precursors, rather than to the scaling down of EOT/CET values and fabrication of capacitors of ultimate quality. Preliminary electrical characterization was also provided in several cases. The capacitors were most often fabricated on silicon substrates using aluminum top electrodes, which is the common approach in a university laboratory scale, but may not provide the quality of capacitors comparable to those fabricated under clean room conditions and using more inert electrode materials suppressing the growth of interfacial layer. More attention has been paid to the process

parametrization, determination of optimum growth temperatures, and investigations on the crystalline structure of the films. One of the earlier studies on HfO₂ films grown from Cp₂Hf(CH₃)₂ and H₂O [96] revealed CET values of 2.7 and 3.4 nm (with interfacial 2 nm thick SiO₂) and permittivities of 12.0 and 13.5 (without SiO₂) in 2.2 and 4.9 nm thick HfO₂. Structure of that thin films was not described, neither were the conduction mechanisms evaluated although current-voltage curves were characteristic of insulating dielectrics. A study on HfO₂ grown from (CpMe)₂HfMe₂, Cp₂Hf(OMe)₂, (CpMe)₂Hf(OMe)Me, (CpMe)₂Hf(OMe)₂, and O₃ [20] was already conducted in order to prove that the HfO₂ grow into deep trenches with aspect ratio of 1:60 almost perfectly especially from CpMe)₂HfMe₂ and (CpMe)₂Hf(OMe)Me, although using 10 times longer cycle times than on planar substrates. Measurements on 5–10 nm thick films revealed the permittivity value of 12 with leakage in the order of 1×10⁻⁷ A/cm² at 1V. These thin films were not evaluated structurally. Another study was devoted on both HfO₂ and ZrO₂ films, in order to prove that these materials grow also with H₂O as oxygen precursor, when (CpMe)₂HfMe₂, (CpMe)₂Hf(OMe)Me, CpMe)₂ZrMe₂, and (CpMe)₂Zr(OMe)Me are used as metal precursors [21]. Conformal growth was not studied, but the paper already revealed the differences between ZrO₂ and HfO₂. In terms of crystallographic phase composition, ZrO₂ was dominantly cubic/tetragonal, whereas HfO₂ appeared as a mixture of monoclinic and cubic/tetragonal phases. It is worth noting, that the CET values of ZrO₂ based capacitors were, probably due to the phase content, lower despite the somewhat higher thickness of ZrO₂, i.e. CET values were 3.9–4.3 nm in 13.3–15.8 nm thick ZrO₂ films and exceeded 5.3 nm in 12.9–13.1 nm thick HfO₂ films, being indicative of the higher permittivity of ZrO₂ in otherwise identical capacitor configurations. On the other hand, leakage tended to be lower in HfO₂ (1×10⁻⁵ A/cm²), compared to that in ZrO₂ (1×10⁻⁴ A/cm²), before the breakdown. Analysis of current mechanisms was not performed. Current mechanisms were evaluated in a later study on 4–13 nm thick HfO₂ and ZrO₂ films grown using O₃ as oxygen precursor, and (CpMe)₂Hf(OMe)Me, CpMe)₂ZrMe₂, and (CpMe)₂Zr(OMe)Me as metal precursors [105], at temperatures mainly lower than room temperature. The currents were found to be bulk-driven, rather than dominated by the interface barriers possibly formed inside the Al/ZrO₂(HfO₂)/p-Si(100) capacitors. In addition, it was found that the density of interfacial electronic defects, D_{it}, was lower (1×10¹¹–1×10¹² cm⁻²eV⁻¹) in ZrO₂-based capacitors compared to the range of values (above 1×10¹² cm⁻²eV⁻¹) measured in HfO₂-based capacitors using deep-level transient spectroscopy (DLTS). Structure of the thin films was not investigated in the latter paper.

CET is quite a thickness-sensitive measure of the capacitive properties. Permittivity or k-value is not supposed to be that thickness-sensitive provided that the films crystallize well already at the very early stages of the growth and the concentration of (residual) impurities in the films is not dependent on the distance from the interface. In fact, the impurity concentration can very well be

profiled, i.e. the highest concentrations can be measured in the vicinity of the substrate [106,107], which basically may mean that the lower the film thickness, the higher the expected amount and the role of impurities. In addition, the crystal growth naturally enhances with the increase in film thickness, because the processes treated within the present context are not epitaxial. Moreover: the lower the thickness of high-k layers, the stronger the effect of interface on the net capacitance. This is the likely reason why the CET of 2–3 nm thick HfO₂ films could not quite be decreased below 2 nm [96]. Other reference studies based on alternative growth methods such as MOCVD of HfO₂ are quite rare. In a paper describing a CVD-process of HfO₂ films using (MeCp)₂HfMe(OⁱPr) and (MeCp)₂HfMe(mmp), where mmp = OCMe₂CH₂OMe, EOT as low as 0.78 nm was claimed, although the physical thickness of the HfO₂ layers was also as low as 1.7 nm [108].

Regarding the ZrO₂ films as those more promising in terms of capacitance at least compared to HfO₂, earlier studies have been conducted using Cp₂Zr(CH₃)₂ and H₂O [97] or Cp₂Zr(CH₃)₂ and O₃ [23] as metal and oxygen precursors, respectively. The CET values ranged from 5.8 to 2.0 nm for the films grown to physical thicknesses ranging from 19.0 to 3.3 nm, respectively. It was also noticed that the exploitation of ozone instead of water has initiated faster growth of ZrO₂ on clean silicon, compared to the water-assisted process, possibly due to the quick pre-oxidation of silicon under O₃ pulses [23]. A recent DLTS study exploring the ZrO₂ films grown from (CpMe)₂ZrMe₂, (CpMe)₂Zr(OMe)Me, CpZr(NMe₂)₃, and O₃ has shown that the last Zr precursor containing only one Cp-group instead of two appeared quite promising in terms of interface trap densities, remaining below $1 \times 10^{11} - 1 \times 10^{12} \text{ cm}^{-2} \text{ eV}^{-1}$ in 6.8–9.0 nm thick annealed films [105]. The leakage current densities were $5 - 10 \times 10^{-8} \text{ A/cm}^2$ at 0.7 V and the current mechanisms were dominantly bulk-limited.

6.1. Doped high-k oxides

Dielectric properties, including the permittivity, of HfO₂ and ZrO₂ are dependent on their crystallographic phases [109–111]. The highest permittivities are characteristic of metastable polymorphs, i.e. cubic and tetragonal. In order to artificially stabilize crystallographic phases with elevated dielectric permittivity mixing or doping of oxides with other elements is practiced. Doping, although certainly introducing defects and gap states, still does not destroy the energetic band structure and wide band gap is thus retained as an essential quality of insulators [82, 101]. It has been known for some time already, that the addition of foreign cations (Y, Ca, Mg, Ce) to the monoclinic zirconia or hafnia stabilizes the cubic and/or tetragonal phases of ZrO₂ or HfO₂ and gives rise to the permittivity up to the values ranging from 32 to 42, depending on dopants [25]. It was also suggested [25] that the permittivity was principally determined by the crystallographic phase of ZrO₂ or HfO₂, rather

than by the nature and amount of the dopants. More recently, ZrO₂ films prospective as gate or memory capacitor dielectrics have been modified or doped using a variety of metal oxides, e.g. Al₂O₃ [66,81] and La₂O₃ [112]. In order to stabilize higher-permittivity cubic or tetragonal ZrO₂ or HfO₂ also rare-earth metals have been introduced and exploited in past few years. ZrO₂ has been doped or mixed with several rare earths like La, Sm, Eu, Gd, Er, etc. [35–37, 112–115] and HfO₂ with Y₂O₃ [30,32] or Er₂O₃ [28].

Since the tetragonality of the lattices of ZrO₂ and HfO₂ is low, i.e. the unit cell parameters of cubic and tetragonal phases are quite similar, the distinction between cubic and tetragonal polymorphs grown is quite complicated. In thin nanocrystalline films, the phase should often be determined on the basis of a very few and broad diffraction peaks. At the same time, the difference between monoclinic and cubic/tetragonal phases is distinct and metastability can immediately be recognized. Often it was observed and reported that the cubic polymorph of ZrO₂ or HfO₂ appeared and retained upon annealing in the doped films, whereas lower-permittivity monoclinic phase became apparent in the non-doped films already in as-deposited state. In HfO₂, the monoclinic phase appears earlier, i.e. at lower film thicknesses compared to that in ZrO₂. Lattice mismatch between Si and HfO₂/ZrO₂ has been studied theoretically and found to be small enough for the possible stabilization of high-permittivity phases by epitaxy [111]. However, even if the native SiO₂ is removed from Si surface by etching with HF, these cubic oxides still do not grow epitaxially due to the regrowth of interfacial SiO₂ in certain extent, i.e. the reoxidation of silicon before the growth of metal oxide can even start.

There are few studies available, devoted to the cyclopentadienyl-based ALD processes of doped HfO₂ and/or ZrO₂ films. Cyclopentadienyls were used as either dopant oxide or host oxide precursors. HfO₂ was doped with Gd₂O₃ in a study where tris(isopropyl-cyclopentadienyl)gadolinium, (iPrCp)₃Gd, and HfCl₄ were used as metal precursors and H₂O as water precursor at 300°C [116]. Tris(ethylcyclopentadienyl)yttrium, (CpMe)₃Y, and hafnium tetrakis(diethylamide), Hf[N(C₂H₅)₂]₄, were used with H₂O to deposit HfO₂:Y₂O₃ films at 250°C [117]. Another study was devoted to the growth of Y-doped HfO₂ from (CpMe)₃Y, and either hafnium tetrakis(ethylmethylamide), Hf[N(C₂H₅)(CH₃)]₄, or bis(cyclopentadienyl)methoxymethylhafnium, (CpMe)₂Hf(OMe)Me [31]. In the latter study, the films were grown at 275 and 350°C from the alkylamide and cyclopentadienyl precursor, respectively, on TiN electrodes with O₃ and the results indicated somewhat better leakage-versus-CET properties for the films grown at lower temperature. A more recent study was devoted to the growth of HfO₂ using monocyclopentadienyls, i.e. cyclopentadienyl-alkylamido precursors [86] in which the films were grown from CpHf(NMe₂)₃, (CpMe)Hf(NMe₂)₃ and O₃, i.e. in the process similar to one of those also described in the present thesis. These films were grown on TiN substrates and the preliminary analysis has indicated some decrease in CET values after doping with Y₂O₃ and annealing, although the leakage current densities were somewhat increased. Yet

another recent study reported the ALD of Er-doped HfO₂ films grown using (¹PrCp)₃Er, (CpMe)₂Hf(OMe)Me and O₃ at 300°C on Si [118]. Regarding ZrO₂ films, tris(2,2,6,6-tetramethyl-3,5-heptanedionato)lanthanum, La(thd)₃, and bis(cyclopentadienyl)methoxymethylzirconium, (CpMe)₂Zr(OMe)Me, were used with O₃ to grow La_yZr_{1-y}O_x thin films at 300°C [36,119]. La-doped ZrO₂ films were grown from (¹PrCp)₃La, (CpMe)₂Zr(OMe)Me and O₃ at 300°C on Ge [120]. A result common to the works reviewed above has been the stabilization of either cubic or tetragonal lattice of the host oxide withstanding heat-treatment without transformation into monoclinic phase, even up to temperatures 900–1000 °C. Another common result was that the permittivity value was increased upon doping compared with non-doped oxides, together with the decrease in EOT/CET in certain extent. The interest in explorations of doped oxide films grown using alternative precursors and/or on different substrate materials is thus retained.

6.2. Nanolaminates

An interest has appeared concerning memory dielectric insulators deposited in the form of sandwiched stacks or multilayers, i.e. nanolaminates [54]. Nanolaminates consist of periodically deposited 2–20 nm thick layers of distinct, chemically defined elements or compounds such as ZrO₂-Al₂O₃-ZrO₂-Al₂O₃-ZrO₂-..., Al₂O₃-TiO₂-Al₂O₃-TiO₂-Al₂O₃-.... etc., reminding superlattices. It is worth noting that cubic and/or tetragonal ZrO₂ can be stabilized in 100–200 nm thick nanolaminate structures, if 5–20 nm thick ZrO₂ layers are repeatedly deposited between films of different chemical composition, e.g. Ta₂O₅ [26], actually giving rise to the dielectric permittivity of the whole laminate. Those nanolaminates were initially grown for different purposes, such as that related to the attempt to improve the performance of thin-film electroluminescent displays by using high-permittivity and well-insulating materials. Also some later studies have indicated that, in nanolaminates, the increase in the thickness of interlayers of higher permittivity additionally increased the net permittivity of the whole multilayer [121]. In addition, due to the multiple interfaces between the constituent oxide layers, multilayer structures could also assist in lowering of the leakage currents. Regarding the contemporary applications, ZrO₂-Al₂O₃-ZrO₂ (also known and denoted as ZAZ) films are probably scaled up for the real application in DRAMs [44]. In the latter structures, cubic/tetragonal ZrO₂ phase was stabilized by applying a very thin Al₂O₃ interlayer deposited between ZrO₂ layers, and also leakage currents were reduced compared to ZrO₂ films. Such kinds of stacks could in principle be taken for nanolaminates, although these films (ZAZ) are not really periodical structures. It however seems, that there are no other studies yet conducted and published describing ZrO₂ or HfO₂ films combined with rare earth oxides in the form of nanolaminates, other than those described in this thesis work.

7. THIN FILM GROWTH PROCESSES EXAMINED IN ARTICLES INCLUDED IN THIS THESIS

Paper I: ZrO_2 and HfO_2 thin films were grown from $(\text{CpMe})_2\text{ZrMe}_2$ and $(\text{CpMe})_2\text{Zr}(\text{OMe})\text{Me}$ as Zr precursors, and O_3 as the oxidant at 300 or 350°C. HfO_2 films were grown from $(\text{CpMe})_2\text{Hf}(\text{OMe})\text{Me}$ and O_3 at 350°C on planar Si as well as deep trenched Si with an aspect ratio of 60:1. Complementarily to the parallel studies on the films processed from the same precursors [19,21,96], TEM and comparative XRD characterization of the phase contents was provided, revealing higher contribution from the monoclinic phase in HfO_2 . Additionally, capacitance and leakage current properties were evaluated. Interface trap densities were estimated. The structural and electrical behavior of the films was somewhat precursor-dependent, revealing better insulating properties in the films grown from oxygen-containing precursors. Also the HfO_2 films showed lower leakage compared to ZrO_2 . Conduction mechanisms prevailing in the films were evaluated.

Paper II: The study was focused on ZrO_2 films as those promising the phase content dominated by cubic/tetragonal phase and thus possibly higher capacitances compared to HfO_2 . $(\text{CpMe})_2\text{ZrMe}_2$ and $(\text{CpMe})_2\text{Zr}(\text{OMe})\text{Me}$ were used as Zr precursors, and O_3 as oxygen precursor. Changes in growth rates against the growth temperature were evaluated comparatively. Crystalline structure of the films was determined. The films were grown also in deep trench substrates with aspect ratio 1:60. Capacitance-voltage and capacitance-dissipation characteristics were measured and relative interface trap densities estimated. Conduction mechanisms dominated either by interface barriers or film bulk were examined as well.

Paper III: In order to seek alternatives to known Zr and Hf cyclopentadienyls, containing two C_5H_5 ligands, growth of ZrO_2 films from novel precursors containing one C_5H_5 ligand and three alkylamine groups, such as $\text{ZrCp}(\text{NMe}_2)_3$, $\text{Zr}(\text{CpMe})(\text{NMe}_2)_3$, and $\text{Zr}(\text{CpEt})(\text{NMe}_2)_3$ was examined. The precursors with mixed ligands have been developed in order to improve the stability and reactivity of the precursors. The films demonstrated conformal growth in trenches achieving step coverage of 80–90%. ZrO_2 films crystallized either after exceeding threshold thickness or upon annealing dominantly in the cubic or tetragonal polymorph. Stability of the cubic phase in 5–7 nm thick films against annealing was demonstrated. Main structural and dielectric properties of these films were described, including CET, interface trap densities, conduction mechanisms and current density versus CET behavior.

Paper IV: The studies were continued on doped films in order to stabilize the cubic/tetragonal phases of $\text{ZrO}_2/\text{HfO}_2$ against annealing. In an earlier and parallel paper, growth of HfO_2 films from a novel cyclopentadienyl-alkylamido

precursor $\text{CpHf}(\text{NMe}_2)_3$ and O_3 was studied, with also some HfO_2 and $\text{HfO}_2\text{:Y}$ -based capacitors preliminarily fabricated on TiN [31]. $(\text{CpMe})_3\text{Y}$ was applied as yttrium precursor. In the present paper HfO_2 and $\text{HfO}_2\text{:Y}$ thin films with Y content of 7–11 at.% were grown from the same precursors at 300°C on moderately doped silicon enabling the evaluation of C-V curves characteristic of MOS structures together with relative interface trap densities. Stabilization of the cubic phase together with the increase in accumulation capacitance was established. Current conduction mechanisms were estimated.

Paper V: The further studies were conducted on doped or mixed ZrO_2 films. Since yttrium is a too common dopant for ZrO_2 (although for different purposes), we preferred to explore alternative rare earth metal oxide dopants and studied the ALD of $\text{ZrO}_2\text{-Gd}_2\text{O}_3$ nanolaminates and $\text{ZrO}_2\text{:Gd}$ mixtures. The films were grown from $(\text{CpMe})_2\text{Zr}(\text{OMe})\text{Me}$, $\text{Gd}(\text{thd})_3$ and O_3 at 300°C on planar substrates. The substrates were highly doped n-Si covered with thin layer of SiO_2 , SiN_x , TiN or Ru. Pure ZrO_2 films possessed mixed phase composition of monoclinic and higher permittivity cubic or tetragonal phases whereas the inclusion of Gd_2O_3 resulted in the disappearance of the monoclinic phase. The structure of the films, current densities, conduction mechanisms and capacitive properties were evaluated. Also the effect of the electrode material on the capacitor performance was evaluated

Paper VI: Search for alternative rare earth dopants was continued and Er_2O_3 chosen as the next candidate, not yet examined in combination with ZrO_2 for high-k purposes. At first ZrO_2 and Er_2O_3 were combined in the form of multi-layer or nanolaminates. $\text{ZrO}_2\text{-Er}_2\text{O}_3$ laminates were grown from $(\text{CpMe})_2\text{Zr}(\text{OMe})\text{Me}$, $\text{Er}(\text{thd})_3$ and ozone as precursors at 350°C on SiO_2/Si and SiN_x/Si substrates, and on 3D substrates with aspect ratio of 1:20. The structure of the laminates and possible effect of cubic structures of both constituent oxides on each other were evaluated by X-ray methods, also against annealing. Complementarily, capacitances, leakage current densities and conduction mechanisms were described.

Paper VII: Studies were continued with depositions of $\text{ZrO}_2\text{:Er}_2\text{O}_3$ doped films from $(\text{CpMe})_2\text{Zr}(\text{OMe})\text{Me}$, $\text{Er}(\text{thd})_3$ and ozone as precursors at 350°C on SiO_2/Si and SiN_x/Si substrates, and on 3D substrates with aspect ratio of 1:20. The content of erbium was tuned by the relative amounts of ZrO_2 and Er_2O_3 deposition cycles. Structure of the films grown was determined in both as-deposited and annealed states. Capacitive behavior as well as current and conduction mechanisms were evaluated.

8. GROWTH RATE, STRUCTURE AND CHARACTERIZATIONS

The oxide films grown within the framework of the present thesis were analyzed using different techniques in order to cover and describe their most essential physical and chemical properties. The measurements have been performed either by the author or her co-authors in order to characterize the samples as completely as possible in terms of the film growth rate, morphology, crystallinity, chemical composition and purity, capacitive and leakage properties. Table 2 lists the techniques used.

Table 2. Film characterization techniques used for the evaluation of the chemical and physical qualities of ZrO₂ and HfO₂ based films within the thesis work. The techniques and data in bold denote the analysis either partially or entirely carried out by the author.

| <i>Technique</i> | <i>Information obtained</i> | <i>Publications</i> |
|--------------------------|---|-----------------------------------|
| UV-VIS spectrometry | Thickness of films grown to thickness exceeding 50–80 nm | II |
| XRR | Thickness, density, and nanolaminated configuration of the films grown to thickness less than 40–50 nm. | I, II, III, IV, V, VI, VII |
| GIXRD | Detection of crystal growth and determination of crystalline polymorphs stabilized in the films | I, II, III, IV, VI, VII |
| EDX | Elemental detection of the composition of the films, estimation of cation and dopant concentrations in per cents | V, VI, VII |
| RBS | Elemental detection of the composition of the films, precise measure of cation and dopant contents | II, V, VII |
| XPS | Recognition of chemical composition concerning the cation-anion bonding affecting the band structure of solids deposited. | VII |
| SEM | Bird-eye view on the film surface, cross-section images of the films grown into 3D substrates | I, II, III, V, VI, VII |
| TEM | Visualization of thickness, crystallinity, interface layers, and nanolaminate configurations of 5–30 nm thick films | I, II, IV, V |
| AFM | Surface morphology, rms roughness | IV, VI, VII |
| C-V and C-D measurements | Capacitance equivalent oxide thickness, dielectric permittivity, interface trap densities | I, II, III, IV, VI, VII |
| I-U measurements | Leakage current densities, conduction mechanisms | I, II, III, IV, VI, VII |

8.1. Growth per cycle

8.1.1 Growth of undoped films

The growth rate of ZrO_2 and HfO_2 films depends mostly on the growth temperature and the precursors used. In the case of the cyclopentadienyl-type precursors applied in the optimized substrate temperature range (ca. 300–350°C), the growth per cycle (GPC) typically remains between 0.045 and 0.065 nm/cycle. This is close to the growth rates of ZrO_2 [12] and HfO_2 [92] films grown from metal chlorides and water around 300°C, if the processes are carried out under similar conditions in a F120 reactor (Figure 4) used throughout the present work.

The F120 is a flow-type hot-wall reactor. In F-120 (Microchemistry Ltd) reactor the reaction chamber is typically formed by the 1mm spacing between two $50 \times 50 \text{ mm}^2$ substrate surfaces placed face-to-face. Material growth on the walls of the reactant supply tubes is avoided by supplying the different reactants through different tubes as close to the reaction chamber as possible. A great advantage of that reactor is that the processes optimized in this reactor are usually easily scalable to large substrates and to very large batches [122,123].

Actually the growth rates with cyclopentadienyls are somewhat higher than those in the case of chloride precursors. Herewith it is worth noting that the growth rates in chloride processes decrease with the increase in substrate temperature, probably due to the decrement in the density of surface $-\text{OH}$ groups, whereas in the case of cyclopentadienyls GPC increases with the temperature, affected by the thermal decomposition of precursors initiated and intensifying above 350–400°C. On the other hand, the growth rates in the cases of both cyclopentadienyl and chloride precursors remain inferior to those obtained with alkylamide-type precursors [124]. In the case of alkylamides, GPC values reach 0.9–1.0 at around 250–275°C, i.e. at the temperatures optimized for this kind of precursors avoiding too strong thermal decomposition. GPC values for several ZrO_2 and HfO_2 processes using cyclopentadienyl precursors as well as for some reference processes are shown in Table 3 in the ascending order. One can see that the beta-diketonate (thd) type precursors provide the lowest growth rate, although ozone was used as the oxygen precursor. It is also to be noted, that for a diketonate-based process, water is not reactive enough and the films can not be grown effectively. Further, it can be seen, that all cyclopentadienyls work with both water and ozone, but ozone enables the growth with slightly higher rate. However, growth rates characteristic of alkylamide processes could not be achieved.

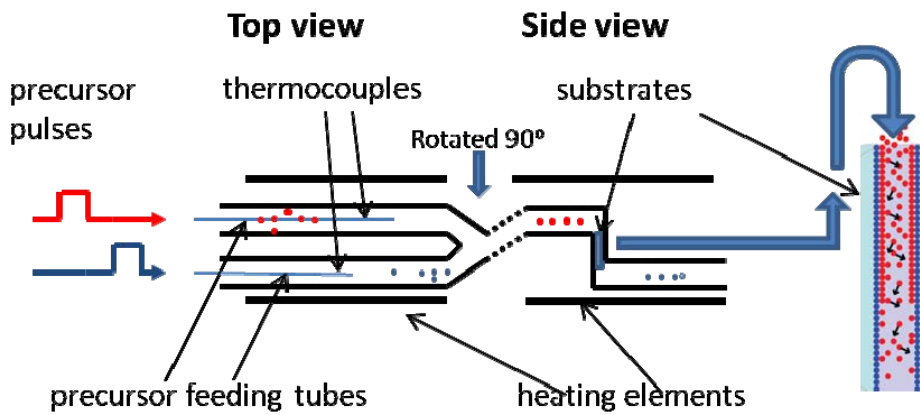


Figure 4. Schematics of hot-wall F-120 type reactor (top) and picture of a real reactor (bottom).

The term “growth per cycle”, i.e. the growth rate, as expressed in the units of Å/cycle or nm/cycle, may remain somewhat undetermined or unclear unless the cycle time parameters are revealed. The exposure times typical for the processes carried out in a F120 reactor remain in the range of 0.5–2.0 s for the metal and oxygen pulse lengths, and ca. 0.5–1.0 s for both purge times. These are the pulse/purge lengths common to the experiments providing samples on planar substrates for structural and electrical studies, established after the examinations of thickness-versus-pulse length dependences and self-limitation. These cycle times are somewhat reactor-dependent. In an open-type F120 reactor, where the substrates are not placed face-to-face in the quartz susceptor forming a narrow flow channel but are fixed into a larger reaction chamber, two-three times longer pulses may be required.

Table 3. Some published ALD experimental data concerning growth rates of ZrO₂ and HfO₂ thin films grown from different precursors in F120 reactors.

| <i>Metal precursor/ oxygen source</i> | <i>Growth per cycle, nm/cycle</i> | <i>Reference</i> |
|--|-----------------------------------|--------------------|
| Zr(thd) ₄ /O ₃ | 0.022 | [18] |
| (CpMe) ₂ HfMe ₂ /H ₂ O | 0.040 | [21] |
| (CpMe) ₂ Hf(OMe)Me/H ₂ O | 0.050 | [21] |
| (CpMe) ₂ ZrMe ₂ /H ₂ O | 0.050 | [21] |
| (CpMe) ₂ Zr(OMe)Me/H ₂ O | 0.050 | [21] |
| HfCl ₄ /H ₂ O | 0.050 | [92] |
| Cp ₂ ZrCl ₂ /O ₃ | 0.053 | [18] |
| ZrCl ₄ /H ₂ O | 0.053 | [92] |
| Cp ₂ Zr(CH ₃) ₂ /O ₃ | 0.055 | [18], [97] |
| (CpMe) ₂ ZrMe ₂ /O ₃ | 0.055 | [I, II] |
| (CpMe) ₂ Hf(OMe)Me/O ₃ | 0.060 | [20] |
| CpZr(NMe ₂) ₃ /O ₃ | 0.065 | [III] |
| (CpMe) ₂ Zr(OMe)Me/O ₃ | 0.065 | [I, II, IV, V, VI] |
| Hf[N(C ₂ H ₅)(CH ₃) ₄]/H ₂ O | 0.090 | [123] |
| Hf[N(CH ₃) ₂] ₄ /H ₂ O | 0.090 | [124] |

In addition, exploitation of deep trench substrates with aspect ratio 1:40–1:90 may require cycle times up to ten times longer than those suited to the planar substrates. In the present work and for the samples fabricated for electrical analyses, the length of a single complete cycle could reach 6–8 seconds.

8.1.2. Growth of nanolaminates and doped films

In the present thesis work, doping of ZrO_2 with erbium and gadolinium was carried out using *beta*-diketonate based processes for Gd_2O_3 and Er_2O_3 , using $Gd(thd)_3$ and $Er(thd)_3$ as precursors, respectively. As implied above, the *beta*-diketonate based ALD does not work by using water but ozone is required for the effective growth. Even when using ozone, the growth rate remains rather low. The growth rates of pure Er_2O_3 and Gd_2O_3 films were only 0.022 and 0.036 nm/cycle, respectively. Thus, upon doping the average growth rate of the ZrO_2 -based dielectric films decreased, as shown in next Figure (Figure5). The higher the amount of the rare earth cycles relative to ZrO_2 cycles, the longer the time necessary to grow the films to target thicknesses.

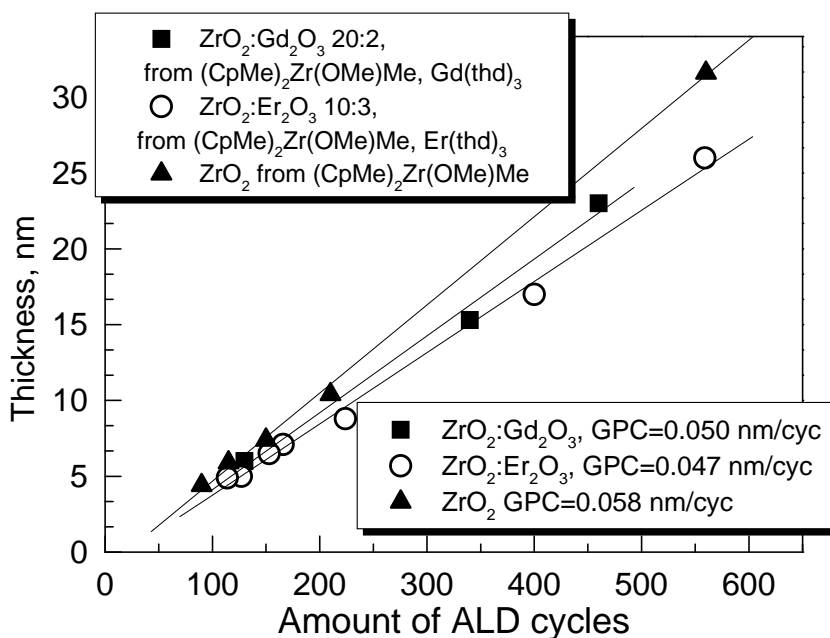


Figure 5. Dependence of film thickness on amount of ALD cycles for undoped ZrO_2 , $ZrO_2:Gd_2O_3$ and $ZrO_2:Er_2O_3$ films grown with different cycle ratios given by inset. The amount of ALD cycles denotes the sum of ZrO_2 and rare earth growth cycles.

The deposition of laminates in the framework of the thesis has resulted in films with well-defined structure, allowing the distinction between the constituent oxide layers. Nanolaminate structures could be recognized either by transmission electron microscopy (TEM) [V] or X-ray reflectivity (XRR) [V, VI]. TEM enables direct visualization of the single layers and estimation of their

thickness, while the XRR patterns are to be modeled in order to calculate the layer thicknesses. In the case of $\text{ZrO}_2\text{-Er}_2\text{O}_3$ laminates, the thickness was determined by XRR only. Figure 6 represents selected XRR patterns of a nanolaminate.

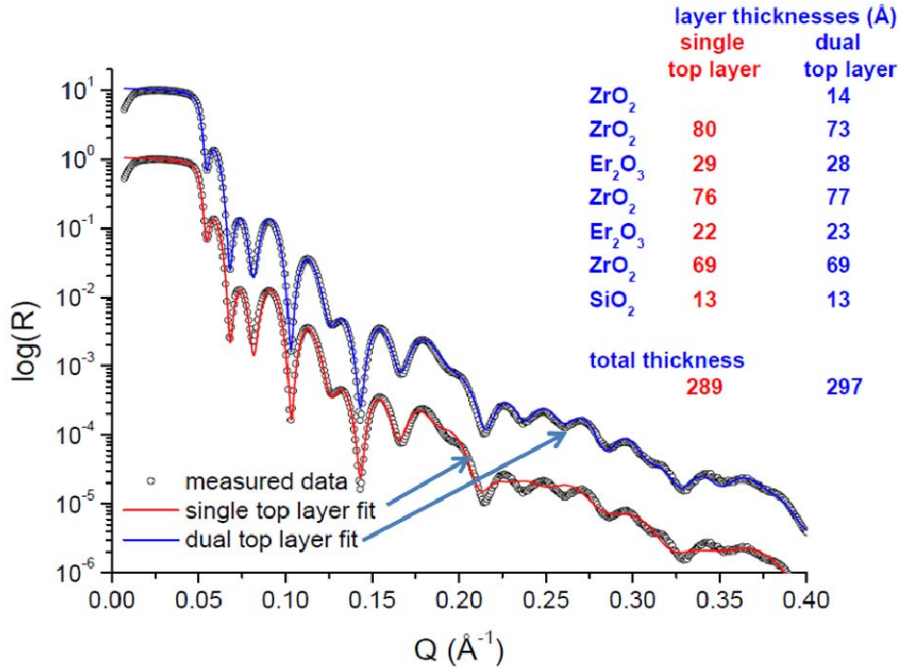


Figure 6. Measured (open circles) and modeled (solid lines) XRR patterns from a nanolaminate grown using the sequence of growth cycles $2 \times (150 \times \text{ZrO}_2 + 115 \times \text{Er}_2\text{O}_3) + 150 \times \text{ZrO}_2$. The thickness profile follows a periodical laminate structure. The thicknesses of layers are shown in two different cases of modeling. The patterns are shifted vertically for the sake of clarity. The total thickness was 28.4 nm (on Si with 1.9 nm thick SiO_2).

XRR can be regarded as quite a trustful and precise method for the determination of thicknesses of very thin layers, also very sensitive to the layer density. In the case of the present example (Figure 6), one can see that the best fit of the XRR patterns was achieved by modeling the topmost ZrO_2 layers with two layers, one with the same density as the other ZrO_2 layers, and another, the outermost and thinner layer, with much lower density. The low density surface layer with a thickness of 0.8–1.8 nm might be due to the surface roughness, though not as good fit could be achieved by just adding roughness to the dense ZrO_2 layer. The reason for the lower density may be found in water and hydrocarbons adsorbed on the surface after the growth.

Table 4. represents the growth recipes and growth rates of the $\text{ZrO}_2\text{-Gd}_2\text{O}_3$ [V] and $\text{ZrO}_2\text{-Er}_2\text{O}_3$ [VI] nanolaminates, determined by XRR. One can see that

the growth rate of the films seems to be slightly accelerating during the deposition. For instance, the mean growth rate of ZrO_2 during the formation of the first layer on SiN_x or SiO_2 was 0.05 nm/cycle. The second ZrO_2 layer on a rare earth oxide interlayer grew with a rate of 0.06 nm/cycle, and the growth rate of the third ZrO_2 layer was 0.06 (in Gd_2O_3) or 0.08 (in Er_2O_3) nm/cycle.

Table 4. Growth cycle sequences and thicknesses of the ZrO_2 - Er_2O_3 and ZrO_2 - Gd_2O_3 films. The thicknesses were measured from films grown on Si covered with 1.0–2.0 nm thick SiO_2 . Thicknesses for single interlayers are listed in the order beginning from the metal oxide first deposited on SiO_2/Si .

| Sequence of deposition cycles, composition, and total thickness | Cycles | Oxides | Thickness Nm | Growth rate, nm/cycle |
|--|--------|-----------|--------------|-----------------------|
| $2 \times [95 \times ZrO_2 + 280 \times Er_2O_3] + 95 \times ZrO_2$ | 95 | ZrO_2 | 5.3 | 0.05 |
| | 280 | Er_2O_3 | 5.7 | 0.02 |
| | 95 | ZrO_2 | 5.8 | 0.06 |
| Film thickness 31.6 nm (Si with 1.0 nm thick SiO_2) | 280 | Er_2O_3 | 7.6 | 0.03 |
| | 95 | ZrO_2 | 5.8 + 1.4 | 0.08 |
| | 150 | ZrO_2 | 8 | 0.05 |
| $2 \times (150 \times ZrO_2 + 50 \times Gd_2O_3) + 150 \times ZrO_2$ | 50 | Gd_2O_3 | 1.2 | 0.02 |
| | 150 | ZrO_2 | 8.4 | 0.06 |
| | 50 | Gd_2O_3 | 1.5 | 0.03 |
| Film thickness 28 nm (Si with 1.3 nm thick SiO_2) | 150 | ZrO_2 | 7.6 + 1.3 | 0.06 |

It is possible, that the growth rate of each subsequent oxide layer slightly increases upon the crystal growth and development in the structure. However, the average growth rate of the nanolaminate has been affected by the relatively low growth rate of the rare earth oxide process based on *beta*-diketonates.

8.2. Morphology and conformal growth of thin films

Surface roughness of thin films is an important property, because too high roughnesses may affect the electronic quality of the contact between dielectric layer and the electrode. High roughness is connected to the formation of polycrystalline structure, likely with sharp edges of crystallites on which the electric field is increased with the probability of the breakdown. Although XRR can also provide surface roughness values besides the film thickness, the surface roughness is most commonly evaluated by using atomic force microscope (AFM). In some cases, also the size of crystallites formed in the films can be estimated, provided that the lateral dimensions of the crystallites are recognized and the features scanned on the surface match the crystallite boundaries. The surface roughness of thin films could be affected by many parameters of the process such as precursors, cycle times, growth temperature, and doping. The

surface roughness correlates primarily to the crystallinity of films, and at similar thickness values the surfaces become rougher in the case of films with higher degree of crystallinity [126]. Usually, different precursors are used at different, optimized, temperatures for the growth of materials of different chemical composition and ability to crystallize. Thus, the effect of a single deposition parameter may not to be easily separated from other factors such as the choice of the precursor. For example, on 130–140 nm thick ZrO_2 films grown from $\text{Zr}(\text{thd})_4$ at 375°C, $\text{Cp}_2\text{Zr}(\text{CH}_3)_2$ at 350°C, and Cp_2ZrCl_2 at 300°C (all with O_3), the rms roughnesses were 4.0, 2.9 and 4.9 nm, respectively [18]. The exact effect of the process conditions on the morphology can hardly be predicted before the experiments. For instance, increase in the growth temperature alone does not necessarily result in the increase in the roughness. Thus, rms roughness values 4.3 and 2.9 nm were measured on 100 nm thick HfO_2 films grown from $\text{Cp}_2\text{Hf}(\text{CH}_3)_2$ and H_2O at 350 and 400°C, respectively [96]. On 50 nm thick HfO_2 films grown from $\text{CpHf}(\text{NMe}_2)_3$ and O_3 on Si at 250, 300 and 350°C, rms roughness values are 2.4, 2.6, and 1.5 nm were measured, respectively [86]. As a general but not necessarily an ultimate rule, much lower roughnesses are characteristic of much thinner films. Roughness as low as 0.2 nm was measured on 5.5 nm thick HfO_2 films grown from $\text{CpHf}(\text{NMe}_2)_3$ and O_3 [86]. Commonly, the surface roughness increases with the film thickness and/or crystal growth. In the case of the films grown for electrical applications, the thickness range of the utmost interest lies between 3–4 and 20–30 nm and, thus, the roughness values may not grow too high. Nevertheless, since the morphology is sensitive to both process and substrate used, the corresponding measurements appear to be necessary.

In the present work, AFM was used for the evaluation of the surface roughness of doped $\text{HfO}_2\text{:Y}$ films [IV], $\text{ZrO}_2\text{-Er}_2\text{O}_3$ nanolaminates [VI] and doped $\text{ZrO}_2\text{:Er}$ films [VII]. Some contact-mode AFM images taken from annealed HfO_2 and $\text{HfO}_2\text{:Y}_2\text{O}_3$ films and as-deposited ZrO_2 and $\text{ZrO}_2\text{:Er}_2\text{O}_3$ films are presented in Fig 7. These films were grown either at 300 °C (HfO_2 , $\text{HfO}_2\text{:Y}_2\text{O}_3$) or 350 °C (ZrO_2 , $\text{ZrO}_2\text{:Er}_2\text{O}_3$) on planar SiO_2/Si substrates from $\text{CpHf}(\text{NMe}_2)_3$, $(\text{CpMe})_3\text{Y}$, $(\text{CpMe})_2\text{Zr}(\text{OMe})\text{Me}$, and $(\text{Er}(\text{thd})_3)$ as metal precursors. O_3 was used as an oxygen precursor. The $\text{ZrO}_2\text{:Er}_2\text{O}_3$ cycle ratio was a 6:4 and the $\text{HfO}_2\text{:Y}_2\text{O}_3$ cycle ratio was a 20:1, i.e. these samples were rather strongly mixed with erbium and quite lightly doped with yttrium.

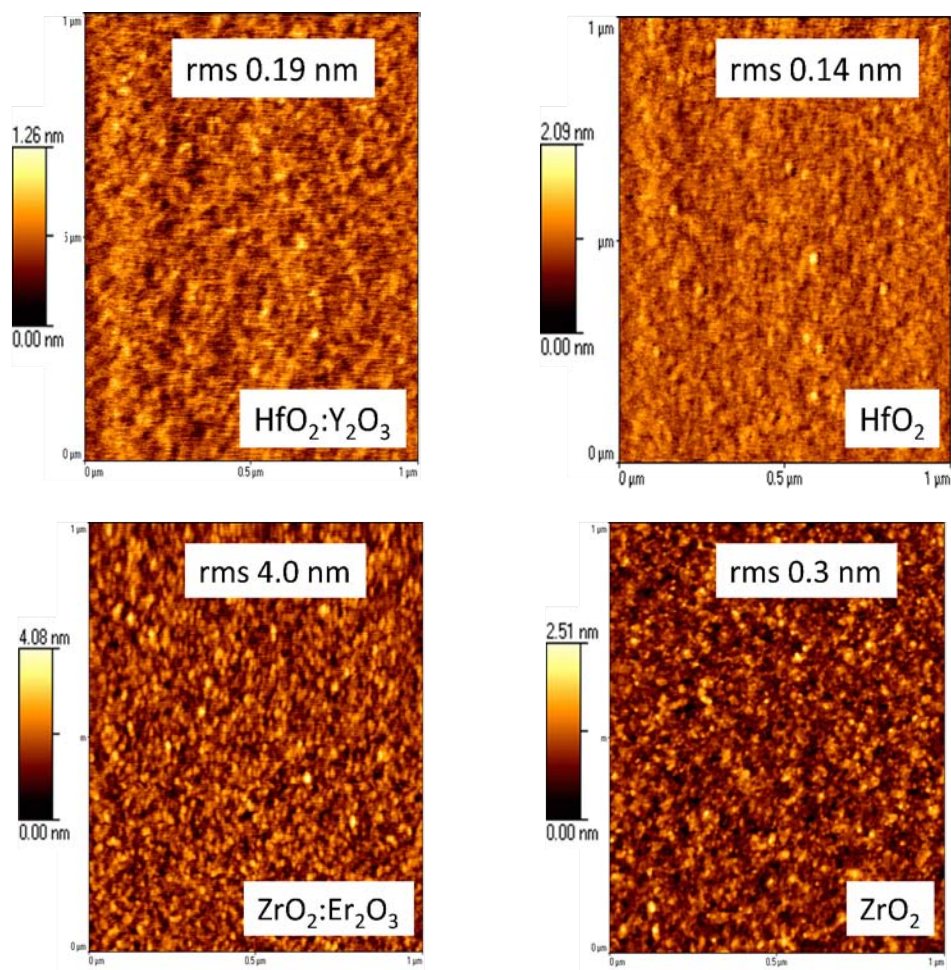


Figure 7. AFM images of 6.7 nm thick $\text{HfO}_2:\text{Y}_2\text{O}_3$ films annealed at 500°C 2 min. in N_2 (top left panel), 6.7 nm thick annealed undoped HfO_2 (top right panel), 7.1 nm thick as-deposited $\text{ZrO}_2:\text{Er}_2\text{O}_3$ (bottom left panel), and 7.4 nm thick as-deposited ZrO_2 film (bottom right panel).

In the present case, HfO_2 and $\text{HfO}_2:\text{Y}$ films were relatively smooth compared to ZrO_2 , and $\text{ZrO}_2:\text{Er}_2\text{O}_3$ films. After annealing the surfaces of $\text{HfO}_2:\text{Y}$, ZrO_2 and $\text{ZrO}_2:\text{Er}_2\text{O}_3$ films roughened possibly due to the growth of single phase nanocrystallites (IV, VI, VII), whereas in the non-doped HfO_2 films the surface could become smoother due to the simultaneous and competing formation of cubic/tetragonal and monoclinic phases (IV) which suppressed the growth of relatively large crystallites able to increase the roughness [114].

As mentioned above, surface roughness tends to increase with the crystal growth. The average sizes of crystallites, D , can be evaluated from the broadening of the (GI)XRD peaks, using the Debye-Scherrer formula:

$$D = 0.9 \cdot \lambda / (FWHM \cdot \cos \theta_B),$$

where λ is the X-radiation wavelength (1.54 Å for Cu K_α), FWHM is the full-width of the diffraction peak at half-maximum, and θ_B is the diffraction angle. The interdependence between film thickness, rms roughness and size of crystals calculated with Debye-Scherrer formula of ZrO_2 and $ZrO_2:Er$ films is shown in Figure 8.

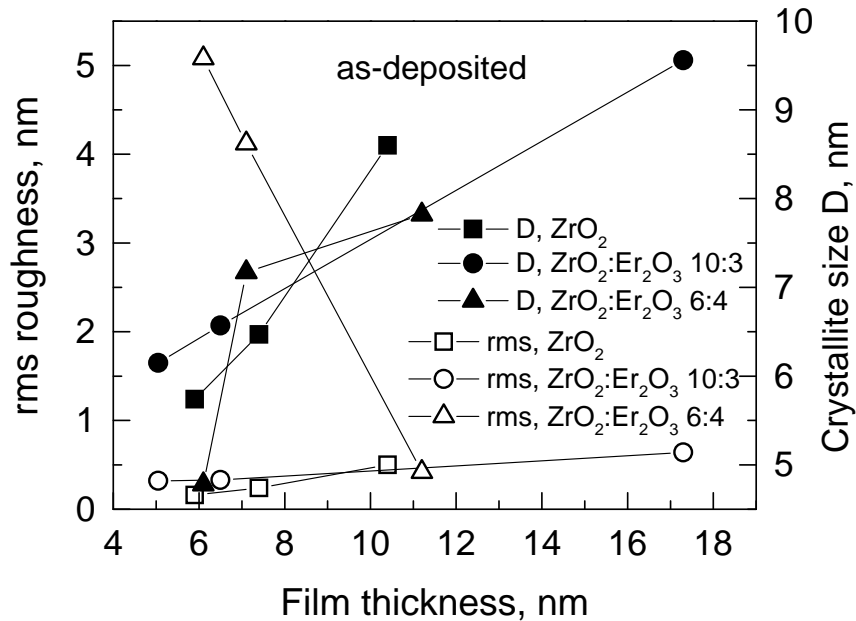


Figure 8. Dependence of rms roughness and size of crystals on thickness of as-deposited ZrO_2 and $ZrO_2:Er$ films.

One can see that the roughness of both undoped and doped films indeed increases with the crystallite size, which in turn increases with the film thickness. It is worth noting that the roughness of undoped ZrO_2 films increases faster with the thickness, compared to the relatively lightly doped $ZrO_2:Er$ films (cycle ratio 10:3). On the other hand, rather strong doping (actually mixing) with erbium using cycle ratio of 6:4 has caused a dramatic increase in the roughness at the very early stages of the growth (Figure 8.), with rms values

almost comparable to the physical thickness. The reasons to the increasing roughness are not yet clarified, but one can assume the effect of some kind of the phase segregation and inhomogeneous incubation of the growth of Er_2O_3 on ZrO_2 and/or vice versa, during just a few consequent growth cycles applied for both constituents (6 and 4). It is to be noted again, that these roughness values are relevant to the surfaces which will later be supplied with the top electrodes in order to carry out the electrical evaluation. Capacitors based on the films with smoother surfaces have demonstrated lower leakage currents [97,127,128, **IV,VI,VII**].

Surface morphology as well as the conformity of the films grown on 3D substrates was also visualized by scanning electron microscope (SEM). The conformality on 3D substrates (AR 1:20 and higher) depends on the precursor chemistry and structure of films: the laminated films may not that easily be grown uniformly, whereas the non-laminated or lightly doped ZrO_2 can be grown uniformly in terms of thickness on nanostructured 3D surfaces. Undoped ZrO_2 films were grown from $(\text{CpMe})_2\text{ZrMe}_2$ and $(\text{CpMe})_2\text{Zr}(\text{OMe})\text{Me}$ and O_3 in deep trenches with aspect ratio of 1:60 with nearly perfect step coverage (actually even resulting in films thicker at the bottom of the trench compared to the thickness at the wafer level) [**I,II**]. Step coverage of ZrO_2 films approaching 90–100% was also achieved with $(\text{CpEt})\text{Zr}(\text{NMe}_2)_3$ and O_3 precursors in deep trenches with aspect ratio of 1:60 [**III**]. It is to be admitted, that the growth of HfO_2 and $\text{HfO}_2\text{:Y}$ on 3D substrates using $(\text{CpMe})_2\text{Hf}(\text{OMe})\text{Me}$, $\text{CpHf}(\text{NMe}_2)_3$, $\text{Hf}[\text{NEtMe}]_4$, $(\text{CpMe})_3\text{Y}$ and O_3 [31,86,**IV**] has not been examined on deep trenched substrates neither in the framework of the present thesis, nor in the parallel studies or in the preceding studies. It is also to be noted, that the effective growth in deep trenches has required the application of cycle times of about ten times exceeding those providing flat films on planar substrates [20,22,**I,III**]. This is basically connected to the growth into deep pores or holes etched into silicon substrates below the wafer level. Regarding the stacked configuration of DRAM prototypes with somewhat weaker demands on the aspect ratio, beginning from ca. 1:20, one could examine the possibilities to deposit the films into the 3D structures using the cycle time parameters close to those providing flat films on 2D substrates. The flatness of the films may, however, heavily depend on the relative amount of the additional oxide used as the constituent for mixing or doping the host material.

Figure 9. represents images of 3D substrates with the empty holes (the top left panel) as well as the films grown from $(\text{CpMe})_2\text{Zr}(\text{OMe})\text{Me}$ and $\text{Er}(\text{thd})_3$ (the top right panel) with relatively large erbium content (12 at.%), i.e. that of the film grown as nanolaminate using cycle sequence $2 \times [95 \times \text{ZrO}_2 + 280 \times \text{Er}_2\text{O}_3] + 95 \times \text{ZrO}_2$. [**VI**]. It can be seen that the thickness of the films could reach the value measured by XRR on planar substrates (28–32 nm) only on the top of the substrate, whereas at the bottom of the hole the thickness of the nanolaminate was 15 nm, as maximum. The step coverage was less than 50%

(Figure 9, the bottom left panel). In figure 9 bottom left panel represents SEM-FIB images from the 26.5 nm thick ZrO_2 : Er_2O_3 films with low erbium content (>1 at.%), grown in the process using the same precursors and cycle ratios of 15:2 using the cycle sequence of $30 \times [15 \times \text{ZrO}_2 + 2 \times \text{Er}_2\text{O}_3] + 30 \times \text{ZrO}_2$ [VII]. The step coverage achieved was nearly 90–100%. The bird-eye view on the three-dimensional substrate demonstrated that the holes were not closed by the oxide film on top (Figure 9, bottom right panel).

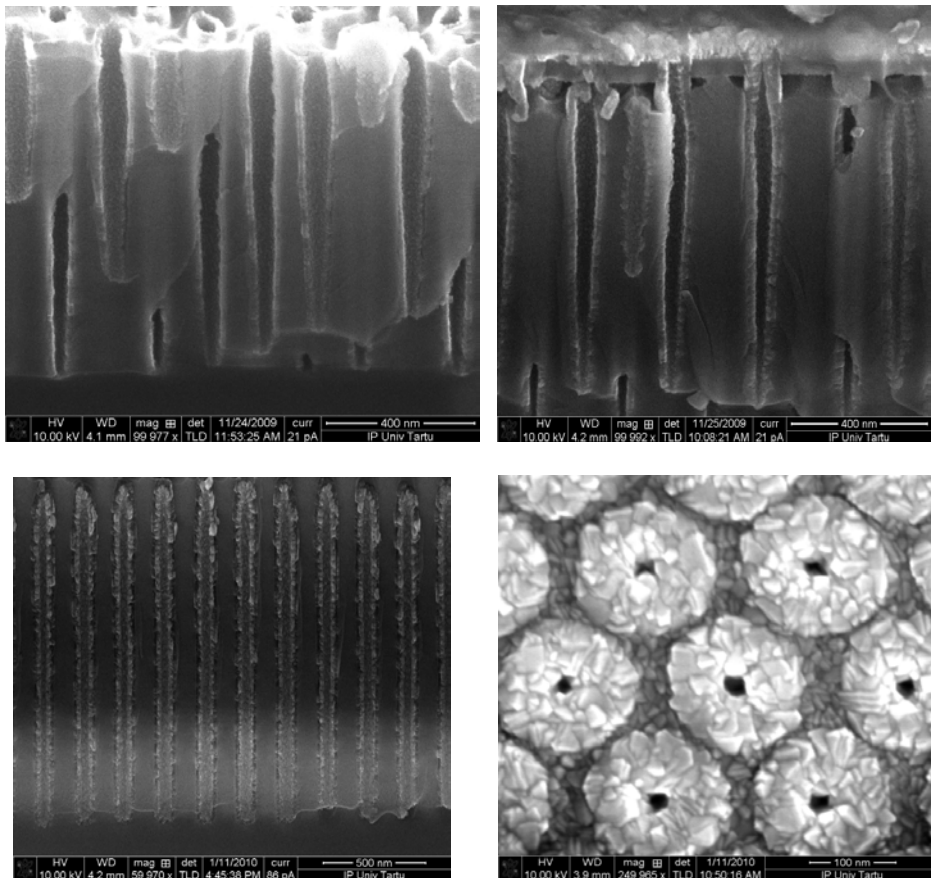


Figure 9. Representative SEM-FIB images from 3D substrates with the empty hole (the top left panel), 31.6 nm thick ZrO_2 - Er_2O_3 nanolaminates (the top right panel), the 26.5 nm thick ZrO_2 : Er_2O_3 films cycle ratios 15:2 (the bottom left panel) and the bird-eye view on the wafer with films (the bottom right panel).

8.3. Structure

The crystal structure of the films grown was evaluated by grazing incidence X-ray diffractometry (GIXRD). GIXRD was used instead of *theta-2theta* (Bragg-Brentano) scans in order to increase the probed area and, consequently, the sensitivity of the analysis, considering the low values of film thickness in the order of a few nanometers. The patterns obtained do not essentially differ from those perhaps more commonly recorded by *theta-2theta* scans unless the films are crystallized with strong orientation along the surface normal. It is known that the diffraction vector is perpendicular to the diffracting planes. The diffraction geometry is always symmetric with respect of the diffracting planes, i.e. the incoming and outgoing beams make each an angle *theta* with respect of the lattice planes (Figure 10). In *theta-2theta* geometry this means that the diffraction vector is perpendicular to the sample surface, i.e. both lattice orientation (if present) and crystallite size is determined in the growth direction of the film. Regarding the HfO₂ and ZrO₂ based materials studied within the present thesis work, the diffraction peaks most intense and most characteristic of these materials appear in the *2theta* range of 28–35°. For instance, if one uses peaks at *2theta* value of 30° (*theta* = 15°) for the recognition of the presence of metastable phases and for the determination of crystallite size, then the change from the *theta-2theta* geometry to the grazing incidence mode with the incident angle of one degree means tilting of the incident angle from 15 to 1 degree, i.e. by 14 degrees (Figure 10). This means that the diffraction vector is tilted 14 degrees away from the surface normal. In a very rough approximation, the tilt within 10–15 degrees may still indicate the orientation close to the surface normal, i.e. in the growth direction.

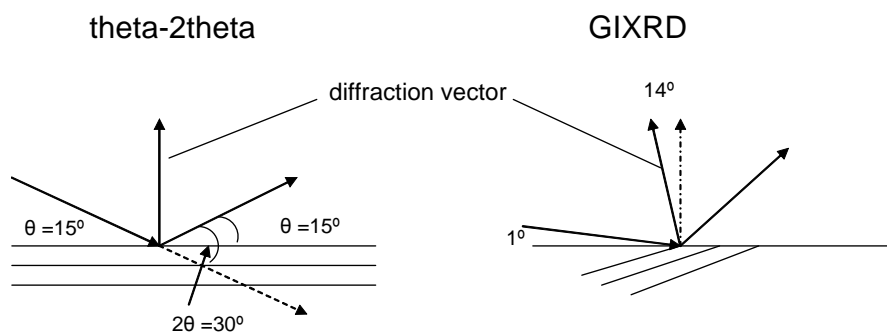


Figure 10. Schematic representation of the difference between *theta-2theta* and grazing incidence X-ray diffraction (GIXRD) scans applied for the detection of possible peaks apparent at 30°. Grazing incidence beam is fixed at 1°.

GIXRD studies have revealed that HfO_2 and ZrO_2 films deposited using $(\text{CpMe})_2\text{ZrMe}_2$, $(\text{CpMe})_2\text{Zr}(\text{OMe})\text{Me}$, $(\text{CpMe})_2\text{Hf}(\text{OMe})\text{Me}$ and ozone to thicknesses ranging from 3.6 to 13.1 nm were X-ray amorphous when the thickness remained below 5–6 nm, and crystallized after exceeding the critical thickness limit [I]. It was also observed, that the ZrO_2 films apparently contained only metastable polymorphs (cubic/tetragonal) until the thickness of 13.1 nm was reached, whereas in the HfO_2 films the monoclinic phase became apparent at lower thicknesses (8.3 nm) [I,IV,VII]. Figure 11 represents the results of structural analysis of ZrO_2 and HfO_2 films grown from different precursors.

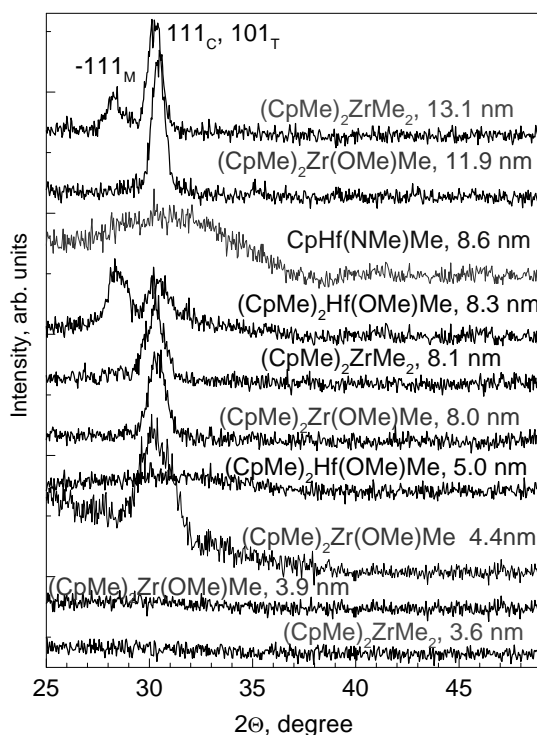


Figure 11. Grazing incidence X-ray diffraction patterns of as-deposited films grown from different precursors at temperatures of 300° and 350°C. Monoclinic, cubic and tetragonal polymorphic phases are denoted with “M”, “C”, and “T”, respectively.

In such thin films, annealing at 650 °C in nitrogen for 10 min did not change the phase composition [I]. Of course the films grown to the thicknesses of 60–70 nm using $(\text{CpMe})_2\text{ZrMe}_2$ and $(\text{CpMe})_2\text{Zr}(\text{OMe})\text{Me}$ as Zr precursors contained quite a significant amount of the monoclinic polymorph [III]. The ZrO_2 films grown using $\text{CpZr}(\text{NMe}_2)_3$ and O_3 to the thicknesses ranging from 5.2 to 7.8

nm retained the cubic/tetragonal structure also after annealing at 550 °C [III], even without doping.

8.3.1. Structure in doped films

In the HfO₂ and in doped HfO₂ with Y grown from CpHf(NMe₂)₃, (CpMe)₃Y and O₃ at 300 °C, the structural analysis has revealed the stabilization of cubic/tetragonal HfO₂ upon annealing at 500 °C, whereas in the undoped films of comparable thickness the contribution from monoclinic phase became obvious [IV] (Figure 12).

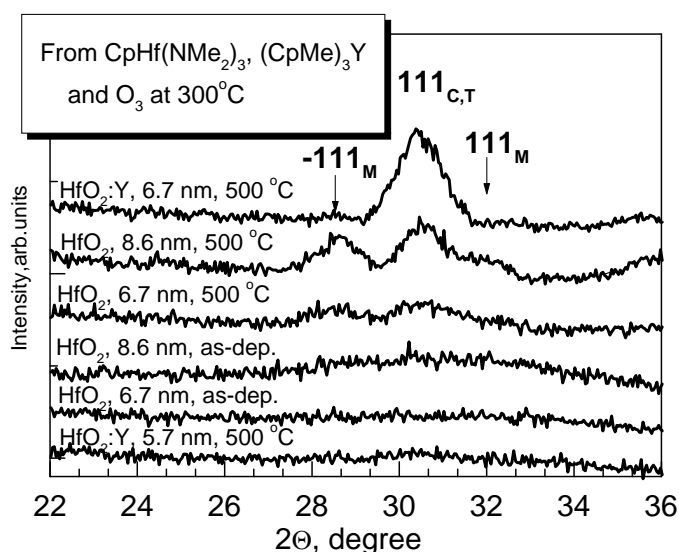


Figure 12. Selected GIXRD patterns demonstrating the development of crystalline structure in HfO₂ and HfO₂:Y films upon changes in thickness and annealing status given by labels.

Yttrium doping had a significant impact on the crystallinity, especially after annealing. The thinnest (5.7 nm) films were amorphous when doped with yttrium, and the amorphous structure was stable also against the annealing procedure. In the HfO₂:Y films thicker than 5.7 nm the only but a rather intense reflection determined after annealing was that of 111 belonging to the cubic or tetragonal HfO₂. In non-doped HfO₂ films the monoclinic reflections were enhanced.

In the ZrO₂ films mixed or doped with erbium or gadolinium oxides [V,VII] only the cubic phases of the constituent oxides were recognized, whereas in the

undoped ZrO_2 the significance of the monoclinic phase reflections increased especially in the films with thickness exceeding 10–13 nm [I,VII]. The $\text{ZrO}_2:\text{Er}_2\text{O}_3$ [VII] and $\text{ZrO}_2:\text{Gd}_2\text{O}_3$ [V] films were not amorphized by doping but crystallized already in the as-deposited state (Fig. 13). The dominant reflections were again found at 30.3° , referring to the metastable ZrO_2 phases prevailing in the doped films. Broad and weak reflections at 35.5° (Figure 13) are attributable to tetragonal 002 and tetragonal or cubic 200 reflections of ZrO_2 . In the films doped with relatively low amounts of erbium or gadolinium, the reflections at 28.3 and 34.7° attributable to the -111 and 002 reflections of monoclinic ZrO_2 were visible even in the as-deposited state. However, the cycle ratios providing relatively high contents of dopant could stabilize the cubic ZrO_2 against the transformation to the monoclinic phase because no traces of monoclinic ZrO_2 appeared in such films.

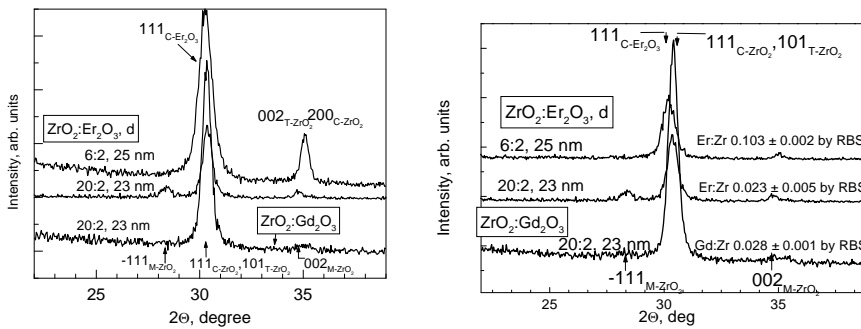


Figure 13. GIXRD patterns of as-deposited (left side) and annealed at 650°C (right side) doped $\text{ZrO}_2:\text{Er}_2\text{O}_3$ and $\text{ZrO}_2:\text{Gd}_2\text{O}_3$ films. Thicknesses and Millers indexes are attributed to distinct either oxides, doped ratio, the contents of dopant and annealing conditions are given by labels, 111 tetragonal or cubic phases of ZrO_2 at 30.2° and 111 cubic reflection of Er_2O_3 at 29.7° . Monoclinic ZrO_2 phase could still appear provided the rare-earth oxide to ZrO_2 cycling ratio was low enough.

8.3.2. Structure of nanolaminated films

In the ZrO_2 films nanolaminated with erbium or gadolinium oxides [V, VI] only the 111 cubic phases and 111 monoclinic phase of the constituent oxides were recognized (Figure 14).

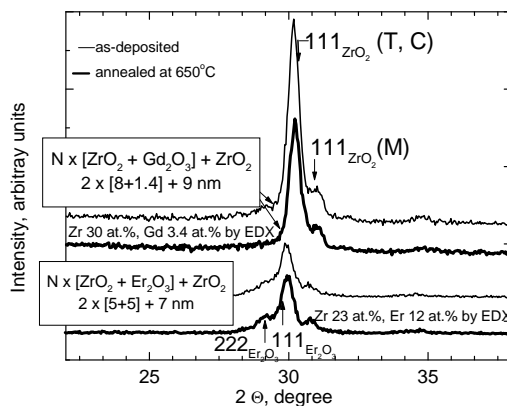


Figure 14. GIXRD patterns of as-deposited and annealed ZrO_2 , Er_2O_3 and Gd_2O_3 films. Film thicknesses, Miller indexes attributed to either oxides, and annealing conditions are given by labels. The 111 and 222 peaks of Er_2O_3 belong to different phases.

The presence of rare earth oxides in nanolaminates with ZrO_2 resulted in the disappearance of the -111 monoclinic reflection at 28.5° and this reflection did not appear in the XRD patterns even after annealing at 650°C .

The structure and phase transformation in ZrO_2 - Er_2O_3 films was also evaluated by high-temperature X-ray diffractometry (HTXRD) [129] between 100 and 1000°C . The HTXRD patterns were taken in N_2 with 50 degrees intervals with heating rate between temperature steps of $5 \text{ min}/50^\circ\text{C}$ and measuring time of 40 min per pattern at each temperature. Figure 15 demonstrates the stability of cubic ZrO_2 deposited either on Er_2O_3 layer or between Er_2O_3 constraint layers [VI]. The cubic ZrO_2 is stabilized at least until annealing temperatures of ca. 1000°C .

In thin films structures we must consider the effect of substrate. The most notable differences appeared in the case of Ru [V]. Usually, the 111 cubic, tetragonal peak at 30.5° was smaller whereas the peaks around 35° attributable to tetragonal 002 and tetragonal or cubic 200 reflections were more pronounced. The presence of Gd_2O_3 in laminates with ZrO_2 resulted in the disappearance of -111 monoclinic peak at 28.5° and this peak did not appear in XRD patterns even after annealing at 650°C (Figure 16). Similar results were characteristic for all used substrates. The peaks attributable to Gd_2O_3 not shown.

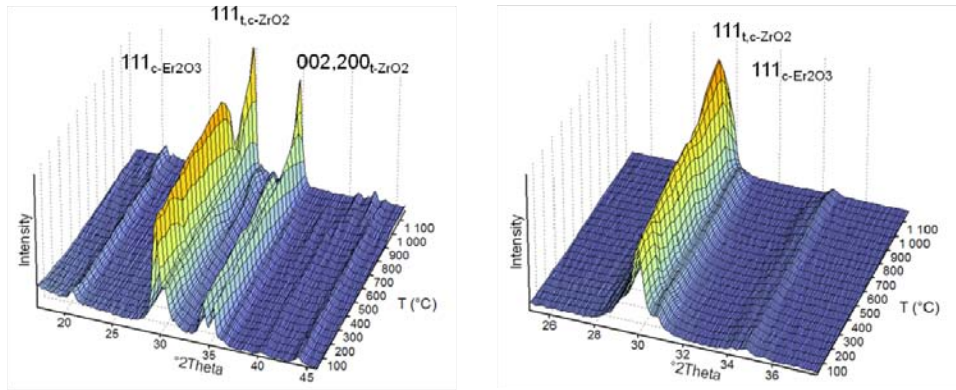


Figure 15. High-temperature three-dimensional XRD patterns of a 1000 + 450 cycles $\text{Er}_2\text{O}_3\text{-ZrO}_2$ double layer (15 at.% Er) (left column) and of a 5 layers $2 \times [95 \times \text{ZrO}_2 + 280 \times \text{Er}_2\text{O}_3] + 95 \times \text{ZrO}_2$ cycles nanolaminate (12 at.% Er) (right column). Picture from [VI].

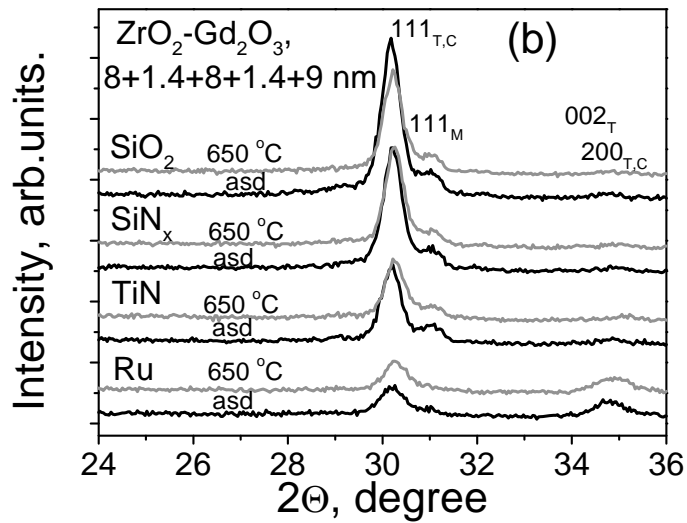


Figure 16. XRD patterns of as-deposited $2 \cdot (\text{ZrO}_2 + \text{Gd}_2\text{O}_3) + \text{ZrO}_2$ laminates on different substrates. The subscripts M, T and C denote monoclinic, tetragonal and cubic phase respectively.

8.4. Composition

Determination of the composition of the thin films is an important part of the materials research. The real chemical composition differs from the target composition already due to the exploitation of a chemical deposition method resulting in contamination with residual impurities always present in the films in certain extent. Also the metal to oxygen atomic ratio in oxides just might deviate from that of the target stoichiometry especially if the surface exchange reactions have not proceeded until completion or too much water has remained in the films. Impurities are always to be regarded as sources of electronic defects, inevitably inducing states in the band-gap of the dielectrics as well as causing surface defects at dielectric/electrode interface. Therefore, it is important to know the content of impurities. The most common impurities in our context are the light elements – hydrogen and carbon – as inherent constituents of the cyclopentadienyl or *beta*-diketonate ligands. There are not many methods available, enabling the exact quantification of light elements in thin films. Possibly, the most adequate method is time-of-flight elastic recoil detection analysis (ToF-ERDA) [130,131]. Growth processes resulting in thin films explored in this thesis have earlier been evaluated namely by ToF-ERDA. Table 5 represents the results of the reference works relevant to both host and dopant materials of current interest. One can see that the hydrogen and carbon contents in the HfO₂ and ZrO₂ films are rather low. For comparison, in the HfO₂ films grown using the competing alkylamide precursors, Hf[N(C₂H₅)(CH₃)₂]₄ and Hf[N(CH₃)₂]₄ [124], the carbon and hydrogen contents could reach 1 and 5–6 at.%, respectively. Also in the rare earth metal oxides, used in this thesis work as dopant materials, especially the hydrogen content tended to be somewhat higher compared to those in the HfO₂ or ZrO₂ films. At the same time, the metal to oxygen atomic ratio in these ZrO₂, HfO₂ and rare earth sesquioxide films has always been very close to the target stoichiometry according to ToF-ERDA, in the reference studies.

Table 5. List of materials deposited and investigated within the present thesis work with the content of hydrogen and carbon impurities measured by ToF-ERDA in parallel studies.

| Film | Precursors | T _{growth} , °C | Hydrogen, at.% | Carbon, at.% | Reference |
|------------------------------------|---|--------------------------|----------------|--------------|-----------|
| HfO₂ | (CpMe) ₂ Hf(OMe)Me/O ₃ | 350 | < 0.1 | < 0.1 | [20] |
| HfO₂ | CpHf(NMe ₂) ₃ /O ₃ | 300 | < 1.0 | < 0.5 | [86] |
| ZrO₂ | (CpMe) ₂ ZrMe ₂ /H ₂ O | 350 | 0.38±0.02 | < 0.5 | [21] |
| ZrO₂ | (CpMe) ₂ Zr(OMe)Me/H ₂ O | 350 | 0.49±0.02 | < 0.5 | [21] |
| Y₂O₃ | (CpMe) ₃ Y/H ₂ O | 300 | 3.1 | 0.2 | [132] |
| Gd₂O₃ | Gd(thd) ₃ /O ₃ | 300 | 1.7 | 2.3 | [133] |
| Er₂O₃ | Er(thd) ₃ /O ₃ | 350 | 3.0 | 0.8 | [134] |

The basic compositions of the host films studied in this thesis were thus analysed earlier and the compositional analysis was therefore provided in order to estimate the ratio of dopant metals to the host only. Energy dispersive X-ray spectrometry (EDX) and Rutherford backscattering spectrometry (RBS) were applied for the determination of the composition of the doped or mixed films, in terms of the relative contents of cations. EDX analysis revealed the presence of dopants in the films, but EDX was not able to quantify the dopants in the relatively lightly doped films grown using the highest $\text{ZrO}_2\text{:Er}_2\text{O}_3$ or $\text{ZrO}_2\text{:Gd}_2\text{O}_3$ cycle ratios. Anyhow, the content of gadolinium in the doped ZrO_2 films [V] was, after the EDX and RBS analyses, clearly correlated to the relative amount of the Gd_2O_3 deposition cycles in between those of binary ZrO_2 (Figure 17).

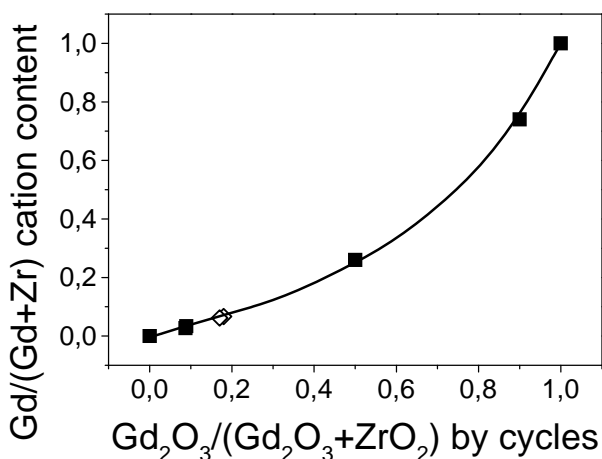


Figure 17. Composition of nanolaminated or doped $\text{ZrO}_2\text{-Gd}_2\text{O}_3$ films, measured either by EDX or RBS, against the ratio of constituent oxide deposition cycles, Figure from V, with the permission of Electrochemical Society.

The same is valid for $\text{ZrO}_2\text{:Er}_2\text{O}_3$ films [VII].

Some of the RBS spectra taken from the $\text{ZrO}_2\text{:Er}_2\text{O}_3$ films are demonstrated in Figure 18.

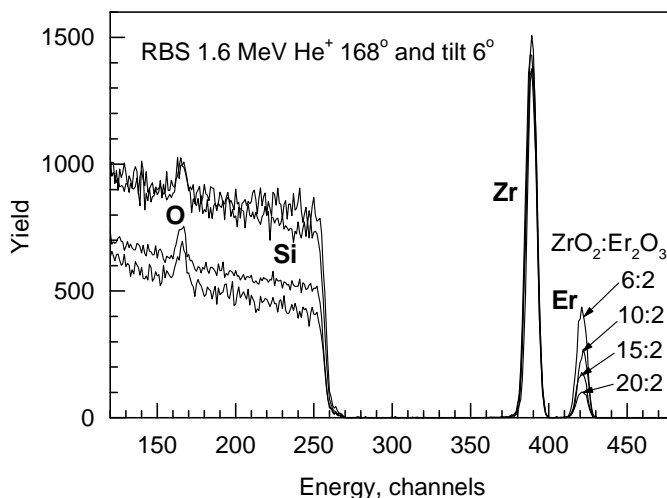


Figure 18. RBS spectra from selected $\text{ZrO}_2:\text{Er}_2\text{O}_3$ films grown using different cycle ratios indicated by labels. One can see, that the erbium signal was clearly detectable in all the doped films and erbium could be quantified in relation to the zirconium.

8.5. Capacitance-voltage measurements

The electrical properties of the films may depend on precursors, substrate, substrate pretreatment and capacitor structure [75,85,105,135,136,**I,II**]. The electrical properties of dielectric films are mainly evaluated on the basis of capacitance-voltage (C-V) and current-voltage (I-U) measurements, providing information about dielectric permittivity and leakage currents as the most important characteristics of a capacitor material. C-V curves were measured to characterize the electrical behavior of the films, estimating the dielectric permittivity as well as interface traps densities. In this study, capacitors were made of dielectric films grown directly on semiconducting or metallic substrate electrodes. Top electrodes (100 nm Al or 20 nm Ti + 100 nm Al) with an area of 0.204 mm² were electron beam evaporated (shadow masked) on the dielectrics either in their as-deposited state or after annealing (Figure 19). In this way an array of parallel-plate planar capacitors was formed on each thin film sample.

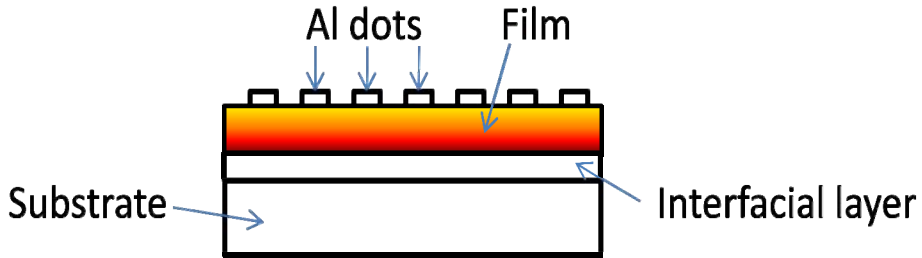


Figure 19. Scheme of capacitor structures with aluminum electrodes. Interfacial layer denotes a dielectric film of chemical composition differing from that of the target high-k material. In the case of silicon substrates, the interfacial layer is mostly formed as native 1-5-2.0 nm thick SiO₂, chemically grown SiO₂ or SiO₂ re-grown on etched silicon during the deposition of the high-k film. Alternatively, the interfacial layer may be formed as Si₃N₄ film or, for instance, oxidized TiN.

The capacitance of the parallel-plate capacitors, C_{total} , is simply expressed as:

$$C_{total} = \frac{\epsilon_{total} \cdot \epsilon_0 \cdot A}{t_{total}}$$

Here ϵ_0 is the permittivity of the free space, ϵ_{total} is the permittivity of all dielectric film between electrodes, A is the capacitor area and t_{total} is the thickness of dielectric layer. In a good approximation, after the capacitance measurements, and knowing the thickness of the dielectric layer, the permittivity can be directly calculated using this formula. However, this is then some kind of average permittivity characterizing the dielectric material consisting of high-k film and interfacial layers, which must be lower than that of the target material. Especially on silicon, one should consider the parasitic interfacial layer of SiO₂, or other layers at interface sometimes grown to unknown thickness and with graded composition especially when the SiO₂ layer was removed by etching prior to high-k deposition. The regrowth of interfacial layer may depend on the material grown into contact to silicon. For instance, the interfacial layers of lower permittivity form more easily between ZrO₂ and Si, compared to HfO₂ and Si [137]. Additional interfacial layers of unknown composition and thickness may form between top electrodes and high-k film. For instance, Al₂O₃ is chemically more stable oxide than ZrO₂, and formation of lower-k interfacial layers may thus be considered, in certain extent, at both sides of the high-k ZrO₂ film. On the other hand and differently from the growth of high-k film on substrate, the deposition of top electrodes is not a thermal process and, therefore, the formation of the interface layer may not be too extensive. For this reason the significance of the top interface layer is often neglected. Nevertheless, in order to avoid the formation of lower-permittivity

layers also between top electrode and the high-k, thin Ti metal layer was often deposited before the Al dots. In the latter case, if any additional oxide (TiZrO_x) could form between Al and ZrO₂, its permittivity would likely exceed that of ZrO₂.

In the case of high-k films grown on silicon with some SiO₂ between Si and high-k film, the total capacitance, C_{tot}, is regarded as a series connection of capacitors:

$$\frac{1}{C_{tot}} = \frac{1}{C_{ox}} + \frac{1}{C_{SiO_2}}$$

Here C_{ox} is the capacitance of high-k oxide layer and C_{SiO₂} is the capacitance of the interfacial layer. The latter is also a parallel-plate capacitor and its capacitance can be expressed as:

$$C_{SiO_2} = \frac{\epsilon_{SiO_2} \cdot \epsilon_0 \cdot A}{t_{SiO_2}}$$

Here ϵ_{SiO_2} is the relative dielectric permittivity of SiO₂ (3.9) and t_{SiO_2} the basically unknown thickness of the SiO₂ interfacial layer. Similarly, the capacitance of the high-k oxide layer, C_{ox}, expressed as:

$$C_{ox} = \frac{\epsilon_{ox} \cdot \epsilon_0 \cdot A}{t_{ox}}$$

where ϵ_{ox} is the unknown relative dielectric permittivity of high-k oxide, and t_{ox} is the thickness of the oxide, which can be determined after XRR measurements. Further, considering that the equivalent oxide thickness EOT (CET), i.e. the value which can be directly calculated from the measured capacitances, was

$$EOT_{total} = \frac{\epsilon_{SiO_2} \cdot t_{total}}{\epsilon_{total}}$$

and after substituting these formulae in the series capacitor equation, one obtains a practically useful relationship between the equivalent oxide thickness and the physically measurable thickness of the high-k oxide:

$$EOT_{total} = \left(\frac{\epsilon_{SiO_2}}{\epsilon_{ox}} \right) \cdot t_{ox} + t_{SiO_2}$$

Provided that one has grown a series of films of similar chemical composition to different thicknesses, it becomes obvious, that the linear dependence between equivalent oxide thickness (EOT or CET) and physical thickness of high-k layers would allow one to extract the permittivity of the high-k material grown from the slope of the relationship, together with the interfacial layer thickness as the intercept with the Y-axis. The interfacial layer thickness may remain somewhat fictive, since the relationship assumes the formation of SiO₂ with fixed permittivity (3.9). The permittivity of the high-k films may, on the other hand, become evaluated more adequately, although even in this case the value obtained must represent an averaged quality without considering the possible changes in film composition and structure in the thickness range of 2–20 nm. Nonetheless, the CET-vs-thickness dependence is the most recognized approach to the estimation of the permittivity [105–107,136] and has also been used in this study to evaluate the ZrO₂:Er₂O₃ dielectrics.

8.6. Capacitance-voltage measurements on metal-oxide-semiconductor (MOS) structures

Both ZrO₂ and HfO₂ based capacitors formed on moderately doped ($1 \times 10^{15} - 1 \times 10^{16} \text{ cm}^{-3}$) silicon substrates demonstrated C-V curves characteristic of metal-oxide-semiconductor capacitors, with accumulation, depletion and inversion regions [75, I]. Besides capacitance values, dielectric loss (dissipation factor, D) was recorded against bias voltage. Figure 20 represents some C-V and D-V curves typical HfO₂ and ZrO₂ films grown in cyclopentadienyl-based ALD processes as well as the curves obtained after measurements on yttrium-doped HfO₂ films.

From the accumulation capacitance, the high-k oxide capacitance can be extracted in a good approximation, allowing one to estimate the CET values and prove that materials with permittivity higher than that of SiO₂ were grown using the given precursors. Thus ZrO₂ and HfO₂ films grown on HF-etched silicon from (CpMe)₂ZrMe₂, (CpMe)₂Zr(OMe)Me and (CpMe)₂Hf(OMe)Me to thicknesses between 3.6 and 13.1 nm possessed CET values ranging from 2.6 to 5.2 nm [I,II]. In connection to the films grown from CpZr(NMe₂)₃, (CpMe)Zr(NMe₂)₃, and (ZpEt)Zr(NMe₂)₃ [III], clear MOS-like behavior was established on silicon substrates, but the CET values were evaluated preferably using the films grown on metallic substrates as will be described below.

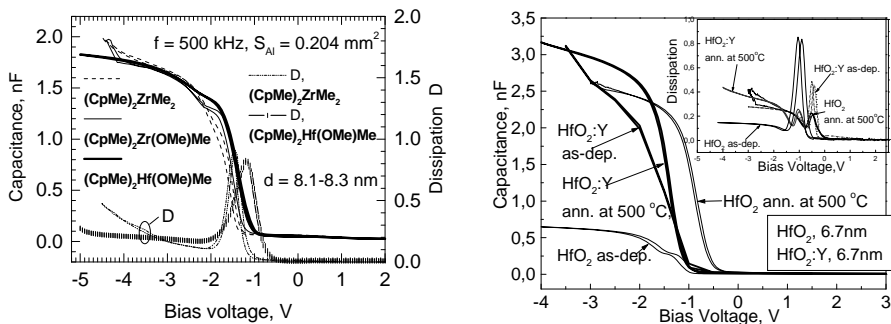


Figure 20. Representative capacitance–voltage and dissipation–voltage curves of the Al/oxide/Si MOS capacitors with dielectric films grown from precursors indicated by labels (left panel), and with doped dielectric films grown from CpHf(NMe₂) and (CpMe)₃Y at 300°C (right panel).

In order to achieve the increased permittivity, the cubic or tetragonal polymorph of HfO₂ ($\epsilon \sim 25\text{--}30$) [27,28,34,101] was stabilized by doping with yttrium [IV]. The yttrium doping caused a prominent increase (0.5nF) in the capacitance compared to the undoped HfO₂ films grown to the same thicknesses. The increase in the capacitance became obvious after annealing. In addition, an obvious shift in the flat-band voltage towards negative bias voltages by approximately 1 V was recorded (Figure 20 right side). The dielectric losses decreased a little with doping especially in as-deposited films.

8.7. Capacitance-voltage measurements in metal-insulator-metal structures

C-V and D-V curves were also obtained from ZrO₂-based capacitors and from doped ZrO₂ films deposited on highly-doped semiconductor substrates ($5 \times 10^{19} \text{ cm}^{-3}$), covered by either 10 nm thick TiN layers or with ca. 1.5 nm thick SiN_x top layers. Such capacitors, although based on semiconductor base electrodes, demonstrate essentially MIM-like behaviour due to the absence of defined band-gap in the substrate material. The C-V curves from such capacitors do not allow one to distinguish between accumulation, depletion and inversion regions [75,104,138]. The curves recorded while measuring the Al/ZrO₂/TiN/Si capacitors with ZrO₂ layers deposited to the thickness of 6.4 nm from the monocyclopentadienyl precursor (CpMe)Zr(NMe₂)₃ clearly exhibited a behavior rather typical for metal-electroded capacitors [III]. The lowest CET values achieved occurred in the range of 0.73–0.85 nm.

Higher capacitances were measured in the $\text{ZrO}_2\text{:Er}$ doped films compared to ZrO_2 doped with Gd (Figure 21 left side). Somewhat expectedly, higher polarizability of cubic ZrO_2 has stronger influence on the capacitance in the films with lower erbium content. After annealing at 650°C in some of the films the capacitance was somewhat decreased in both $\text{ZrO}_2\text{:Er}$ and $\text{ZrO}_2\text{:Gd}$ doped films, probably due to the development of lower- k interfacial layers. The films also exhibited dielectric dispersion, because the measurements at 100 kHz, 500 kHz and 1 MHz revealed capacitances decreasing systematically with the increase in frequency (Figure 21 right side). The dielectric losses expressed by dissipation factor did not exceed 0.1 at 100 and 500 kHz, while at 1 MHz the losses could approach 0.5.

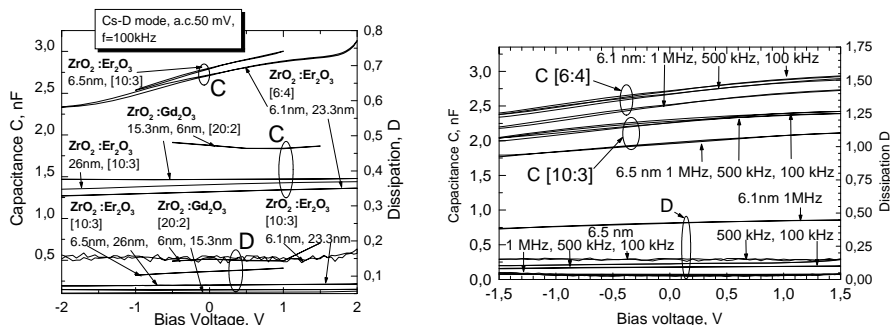


Figure 21. Selected C-V and D-V curves of ZrO_2 films doped with erbium and gadolinium grown with different cycle ratios given by labels (left side), and C-V and D-V curves from the two selected ZrO_2 films doped with erbium and grown to certain thicknesses measured at different frequencies (right side). Cycle ratios and measurement frequencies are denoted by labels.

8.8. The Capacitance Equivalent Oxide Thickness

CET of both ZrO_2 and HfO_2 films indicated the permittivity of these dielectric layers being higher than that of pure SiO_2 . The ZrO_2 films grown from $(\text{CpMe})_2\text{ZrMe}_2$ possessed generally lower CET compared to the films obtained from $(\text{CpMe})_2\text{Zr}(\text{OMe})\text{Me}$ [I]. CET in ZrO_2 films normally increased with the thickness. CET measured for 5–8 nm thick ZrO_2 films as-deposited on highly doped SiO_2/Si substrates was 2.32 ± 0.3 nm [III]. The CET was not strictly proportional to the ZrO_2 thickness, possibly due to the amorphicity of the thinnest films. After annealing the corresponding CET values decreased somewhat to 2.23 ± 0.30 nm. In the HfO_2 films as-deposited from $\text{CpHf}(\text{NMe}_2)_3$ and $(\text{CpMe})_2\text{Hf}(\text{OMe})\text{Me}$, CET varied between 2.4 and 5.2 nm, decreasing with film thickness and decreasing upon crystallization [I, III, IV].

Figure 22 depicts the dependence of CET on the physical thickness for ZrO₂ and HfO₂ films. The chemical composition and annealing status of the oxide are the parameters. One can see, that the CET of the films generally follows the typical linear dependence on the physical thickness. CET of the thinnest annealed films was markedly higher compared to that of as-deposited films, which can be explained by the amorphous structure of these films, in addition to the possible growth of the Si-rich interface layer. Evidently, clear and intense crystallization is the pre-requirement for high capacitances. Upon annealing the permittivity increased in HfO₂ films, but decreased in ZrO₂ films. Permittivity values were nevertheless estimated on the basis of linear relationship between CET and physical thickness [28,107,139] in the whole range deposited.

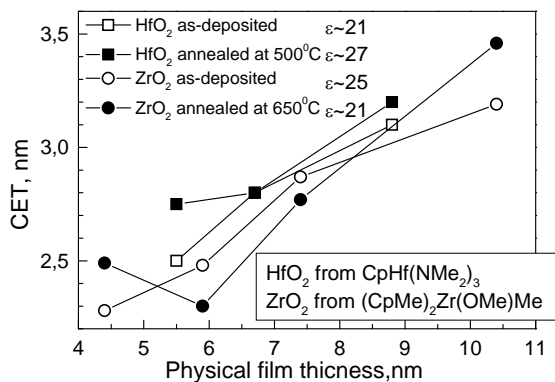


Figure 22. Capacitance equivalent oxide thickness of HfO₂ and ZrO₂ films against film thickness in as-deposited (open symbols) and annealed (closed symbols) states. The materials and the permittivity of films extracted is given by the labels.

In as-deposited HfO₂:Y films the CET was similar to that of the undoped HfO₂ films [IV]. In the annealed films CET of HfO₂:Y occurred clearly lower than that of HfO₂ films, provided that the films became crystallized after annealing. Crystallization required growth to thicknesses exceeding 6 nm and the films were crystallized in the form of cubic polymorph of HfO₂.

ZrO₂:Er and ZrO₂ films possessed quite similar CET with values slightly lower for doped films. The best CET values were measured for ZrO₂:Gd films on Ru electrode: 0.97 nm for 6.1 nm thick film. The CET values of films deposited on SiO₂ were generally 1.5 to 2 nm higher than those of similar films on Ru. Commonly the CET increased with the physical film thickness. The trends are shown in Figure 23.

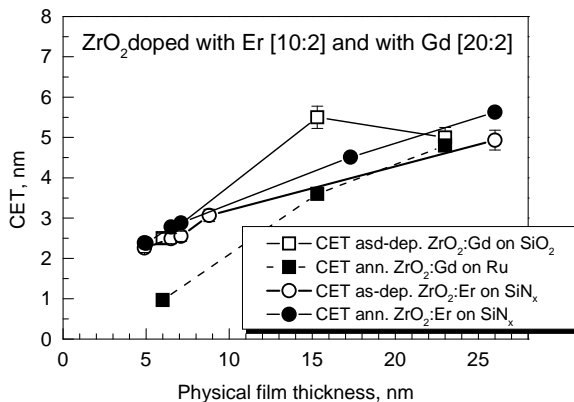


Figure 23. Capacitance equivalent oxide thickness against physical thickness of $\text{ZrO}_2\text{:Er}_2\text{O}_3$ and $\text{ZrO}_2\text{:Gd}_2\text{O}_3$ films. Annealing status, cycle ratios and substrate of films are denoted by labels.

Er_2O_3 -containing films could not be grown at 350°C on high-work-function ruthenium electrode, whereas $\text{ZrO}_2\text{-Gd}_2\text{O}_3$ laminates could be grown at 300°C on Ru. Ru indeed makes the difference in terms of CET and leakage current. Er_2O_3 just grew more uniform at 350°C , and Gd_2O_3 at 300°C . Probably 350°C was too high for the O_3 process. Ozone is able to etch ruthenium, forming volatile RuO_4 . Otherwise, ruthenium is actively studied as one of the most prospective electrode contacting capacitor dielectrics

8.9. Interface state densities

The conductance-voltage curves recorded in parallel with capacitance-voltage curves (Figure 24) refers to a method used for characterization of semiconductor materials and devices. The method is based on conductance measurements on a metal-semiconductor junction (Schottky barrier) and on the appearance of depletion region in the semiconducting substrate electrode, i.e. a region which is empty of conducting electrons and holes, but may contain ionized donors and electrically active defects or *traps*. The depletion region with its ionized charges behaves like a capacitor in series with the dielectric oxide. By varying the voltage applied to the junction it is possible to vary the depletion width. The dependence of the depletion width upon the applied voltage provides information on the semiconductor's internal characteristics, such as its doping profile and electrically active defect densities. The oxide films deposited on the semiconductor are also never free of defects but contain intrinsic defects (dependent on growth technology and precursor chemistry

resulting in residual contamination) and extrinsic defects (due to non-clean room conditions.) [75,138]. An intrinsic defect contains an interface trap or a donor if it can become neutral or positive by donating (giving up) an electron and acceptor interface trap can become neutral and negative by accepting electron. The electronic quality of the oxide/semiconductor interface is thus process-sensitive. When a voltage is applied, the interface-trap levels move up or down with the valence and conduction band while the Fermi level remained fixed. Charges are transferred from semiconductor to dielectric either from the conduction band of the semiconductor to the traps in oxide or between trap states. This charge contributes to the MOS capacitance and alters the ideal MOS curve [104].

Both capacitance and conductance measurements can be used to evaluate the interface trap densities (D_{it}), because both the input conductance and the input capacitance of the equivalent circuit (Figure 24) contain similar information about the interface traps. The capacitance measurements can give rapid evaluation of the interface-trapped charge [104].

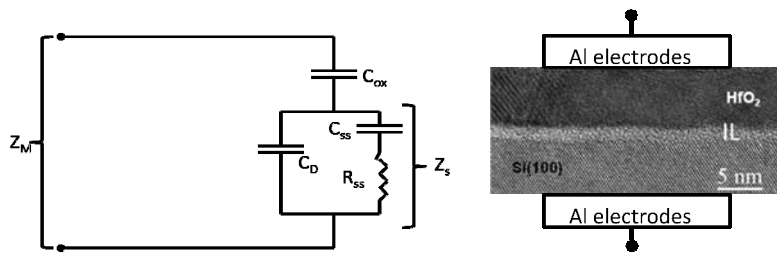


Figure 24. MOS capacitors with very simplified effective equivalent circuit. This circuit represents the behavior of a MOS capacitor. C_{ox} is the oxide capacitance, C_D is the voltage variable depletion capacitance, and C_{ss} - R_{ss} is the voltage and frequency dependent interface state branch (left side). Right side represents the scheme of the same MOS capacitor structures with aluminum electrodes and real film (TEM picture). Interfacial layer (IL) denotes a dielectric film of chemical composition differing from that of the target high-k material. In the case of silicon substrates, the interfacial layer is mostly formed as native 1-5-2.0 nm thick SiO_2 , chemically grown SiO_2 or SiO_2 re-grown on etched silicon during the deposition of the high-k film.

The conductance method was studied in detail by Nicollian [104,140]. The method requires quite an extensive data acquisition. For the estimation of D_{it} in the real oxide films grown within the present study, we have used somewhat simplified Hill's method [141]. Traditional detailed analysis requires elaborate frequency dependent techniques, but the Hill's methods use the single frequency technique as an approximation method which provides quantitative criteria on the quality of such interfaces. The data required comprise a single high frequency capacitance vs voltage measurement and a corresponding conductance vs voltage measurement [141].

In several papers, D_{it} is calculated from capacitance-voltage-dissipation measurements using conductance method. The conductance method [140] is one of the most reliable and commonly adopted interface trap density (D_{it}) extraction techniques used to evaluate the passivity of interfaces. The conductance method for semiconductors based on the Ge and Si was applied e.g. by Martens, Mahata and Maiti [142–144].

The equivalent parallel conductance, G_c [104,141,144] is expressed as:

$$G_c = \omega C_i / [(C_i(C_{ox})^2 + (1 - C_i/C_{ox})^2)],$$

where C_i is the measured capacitance and C_{ox} is the capacitance of the oxide, ω is the measurement frequency

Then

$$D_{it} = \max G_c / [0.402 \omega q A],$$

where A is the capacitor area, ω is the frequency and q is the electron charge, 1.69×10^{-19} eV. D_{it} in the vicinity of the film/substrate interface is responsible for the increase in the conductance signal and related dielectric loss [144]. There is a correlation between defect densities and the shape of C-V curves, D_{it} is at maximum behind to the flat-band voltage, indicating the strongest response of the interface traps to the measurement signal after the disappearance of the depletion region and before the formation of accumulation. In this region, the charges can most intensely tunnel through oxide/semiconductor interface between trap states. Maximum signal intensity is taken for the criterion of D_{it} . Figure 25 represents selected C-V, D-V and D_{it} curves as results measured from HfO_2 films grown from $CpHf(NMe_2)_3$ and O_3 [IV], at a picked frequency on SiO_2/Si .

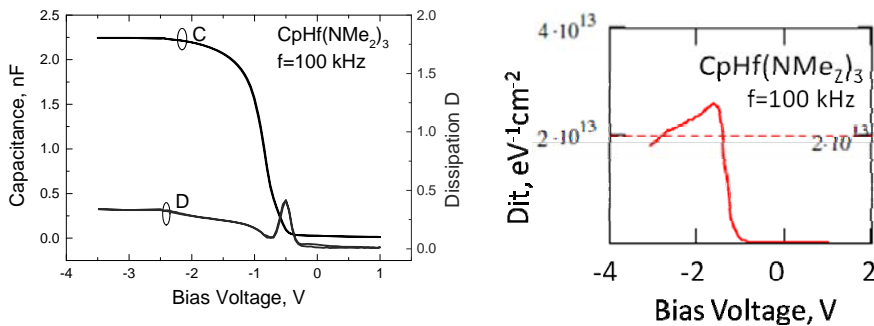


Figure 25. Capacitance-voltage and dissipation-voltage behavior of a typical 5.7 nm thick HfO_2 film (left panel) and the corresponding interface trap density-voltage curve (right panel). The hafnium precursor and measurement frequency are given by labels.

In practice, the density of electronic defects was in the order of magnitude of $1 \times 10^{12} \text{ eV}^{-1} \text{ cm}^{-2}$ in ZrO_2 films and $1 \times 10^{11} \text{ eV}^{-1} \text{ cm}^{-2}$ in HfO_2 films [I, III]. Dependence of D_{it} on the precursor chemistry was not obvious. At the same time, doping of HfO_2 with Y seemed to reduce the defect densities in MOS structures [IV].

The interface traps densities estimated for the films grown using different precursors are listed in Table 6.

Table 6. Precursors, thickness, d, and interface state densities, D_{it} of representative ZrO_2 and HfO_2 films grown from different precursors.

| Precursor | Thickness, nm | D_{it} , 100kHz ($\text{eV}^{-1} \text{ cm}^{-2}$) | Reference |
|--|---------------|--|-----------|
| $\text{ZrCp}(\text{NMe}_2)_3$ | 6.8 | 2.42×10^{13} | [III] |
| $(\text{CpMe})_2\text{ZrMe}_2$ | 13.1 | $4-7 \times 10^{12}$ | [I, II] |
| $(\text{CpMe})_2\text{Zr}(\text{OMe})\text{Me}$ | 11.9 | $4-7 \times 10^{12}$ | [I, II] |
| $(\text{CpMe})_2\text{Hf}(\text{OMe})\text{Me}$ | 8.3 | 1.50×10^{11} | [I] |
| $\text{CpHf}(\text{NMe}_2)_3$ | 5.5 | 1.1×10^{13} | [I, IV] |
| $\text{CpHf}(\text{NMe}_2)_3$ Doped with Y ($(\text{CpMe})_3\text{Y}$) | 6.7 | 8.6×10^{12} | [IV] |

The $\text{ZrO}_2:\text{Gd}$ and $\text{ZrO}_2:\text{Er}$ films were grown on substrates exhibiting metallic or semi-metallic conduction, thus not allowing the application of conductance methods suited to MOS-like structures. However, since the investigation of the doped and nanolaminated films was primarily focused on the studies of structure, composition and electrical performance of films which were at least possibly to be suited to memory capacitor technology, the estimation of D_{it} would be of secondary importance.

Capacitance measurements carried out on samples grown for the present study did not reveal any noticeable dependence of the capacitive properties or trap densities on the different cyclopentadienyl-based precursors. All of the precursors exploited enabled to produce good-quality dielectric films in terms of capacitance and equivalent oxide thickness. Qualitative differences in the electrical properties may appear upon doping or nanolaminating, i.e. mixing of different metal oxides, rather than upon changes in the chemistry within the particular class of precursors.

8.10. Conduction mechanisms

The conduction mechanisms in metal-insulator-metal or metal-insulator-semiconductor stacks can basically be divided to either electrode or bulk limited mechanisms [75,138]. In both cases, the charge carriers may be thermally excited from an electrode or trap to the insulator conduction or valence band. Then, in the “bulk” of the films, the excitation of the charge carriers from the trapping states in the band gap to the conduction band may also be favored by the electric field lowering the effective barrier to the excitation. Additionally, at possibly even higher electric fields, the charge carriers may tunnel either directly from electrode to the conduction band of the insulating oxide, or from electrode or defect levels in the band gap of the oxide at the interface.

The effective barrier for thermal excitation is decreased due to electric field and the respective current-density electric-field dependence is

$$J = A \cdot T^2 \cdot \exp[(\Phi_0 - \beta_{RS} \cdot E^{1/2})/kT]$$

for emission from electrode (Richardson-Schottky emission) and

$$J = \sigma_0 \cdot E \cdot \exp[(\Phi_d - \beta_{PF} \cdot E^{1/2})/rkT]$$

for emission from donors (Poole-Frenkel effect) [75,104,138,145]. Parameter A is a constant, Φ_0 is barrier height at the electrode dielectric interface, Φ_d is donor ionization energy, T is temperature, σ_0 conductivity at low electric fields, r is a factor between 1–2 taking into account trap compensation, and β_{RS} or β_{PF} are respectively Richardson-Schottky or Poole-Frenkel constants [104]. The latter two constants depend on the refractive index of the insulator materials n and are calculated respectively as

$$\beta_{RS} = (q^3/(4 \cdot \epsilon_0 \cdot n^2))^{1/2}$$

and

$$\beta_{PF} = (q^3/(\epsilon_0 \cdot n^2))^{1/2},$$

where ϵ_0 is the dielectric permittivity of free space and q is the electron charge, 1.69×10^{-19} eV. At relevant electric fields, both mechanisms should give linear trend in the Poole-Frenkel plot

$$\ln(J/E) \sim E^{1/2}$$

whereas the slope should depend only on n [104, 138]. Distinguishing one mechanism from the other is often complicated especially because of the factor r can be 1 for the normal Poole-Frenkel effect and 2 for a modified Poole-

Frenkel effect (trap compensation) [104,138]. In the latter case, the slope would be similar to the Richardson-Schottky emission. Since the temperature-dependences of the currents are different for these two different mechanisms, the measurements at different (low) temperatures could assist in better determination of the dominant current mechanisms. However, these films should function as capacitor dielectrics at room temperature and at higher temperatures. Thus the exact distinction between the mechanisms may not be of ultimate importance, especially if their coexistence is likely.

The tunneling current from the electrode is described by Fowler-Nordheim formula

$$J = a \cdot \Phi_0^{-1} \cdot E^2 \cdot \exp(-b \cdot \Phi_0^{3/2}/E),$$

whereas tunneling from traps may result in similar functional form

$$J \sim \exp(-b \cdot \Phi_t^{3/2}/E).$$

Tunnelling mechanisms are not sensitive to measurement temperature. Parameters a and b are constants which depend on effective mass. In the case of tunneling, the current density-electric field curves should be linear in the Fowler-Nordheim plot

$$\ln(J/E^2) \sim 1/E$$

whereas, the slope should give the barrier heights when effective mass is known. The thermal excitation and tunneling currents have similar functional forms for both electrode and bulk limited mechanisms, but electrode limited mechanisms should result in strong dependence on voltage polarity if the electrodes have different work function [75,104].

8.10.1. Conduction mechanism in MOS structures

Current-voltage relationships resulting in linear $\ln(J/U)$ versus $U^{1/2}$ plots can imply the dominance of Pool-Frenkel effect. Figure 26 shows Poole-Frenkel plots from selected ZrO_2 and HfO_2 films with fitted curves [I,II,IV]. These films probably gave the best Poole-Frenkel fits obtained in this work.

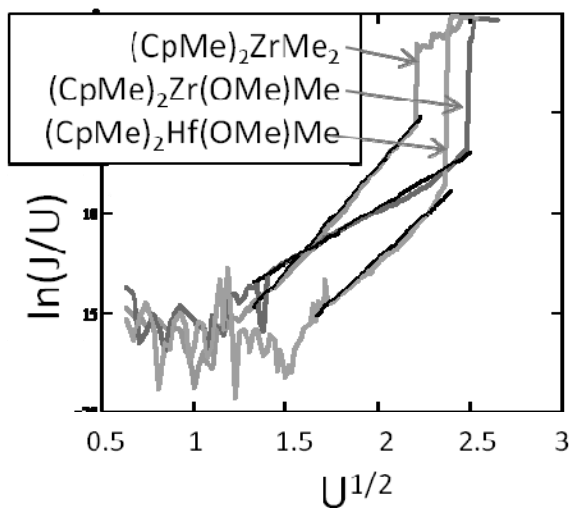


Figure 26. Poole-Frenkel plot from capacitors with 13.1 nm thick ZrO_2 films grown from $(CpMe)_2ZrMe_2$, 11.9 nm thick ZrO_2 films grown from $(CpMe)_2Zr(OMe)Me$ and 10 nm thick HfO_2 films grown from $(CpMe)_2Hf(OMe)Me$ and O_3 at 300 or 350°C. Electrical characteristics were measured on planar Al/ ZrO_2 (HfO_2)/p-Si(100)/Al capacitors with e-beam evaporated Al dot electrodes (shadow masked) with an area of 0.204 mm².

In most cases, typical shapes of J - E curves measured implied that various conduction mechanisms can be expected at different electric field ranges (Figure 27). The possibly dominating conduction mechanisms could depend on precursors, thickness, growth temperature, electrode material and film composition [105, I,III].

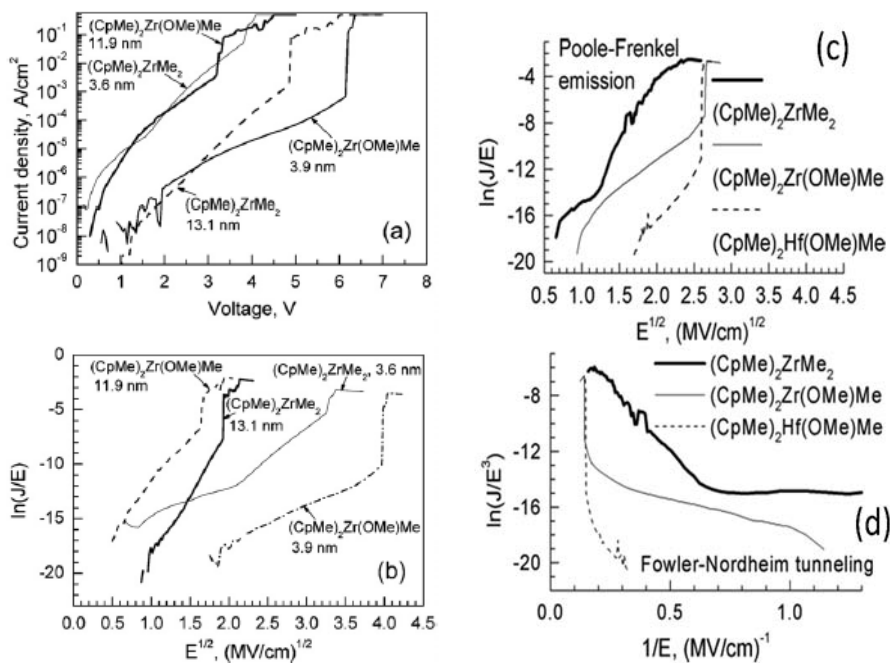


Figure 27. Current density–voltage (a) and Poole–Frenkel (b) plots of some ZrO_2 films deposited to different thicknesses (left column) [II], and representative Poole–Frenkel (c) and Fowler–Nordheim (d) plots of ZrO_2 and HfO_2 films grown to similar thicknesses (8.1–8.3 nm) [I]. Labels indicate the metal precursor and film thickness.

Conduction mechanisms usually assigned to undoped or “pure” ZrO_2 or HfO_2 films were the Poole–Frenkel effect [I,II,III], Fowler–Nordheim emission [I,IV]. The conduction mechanisms recognized in our films, depending on precursors are also listed in Table (Table 7.).

It seems, that the most common and most easily recognized conduction mechanism in ZrO_2 and HfO_2 films was the Poole–Frenkel (a bulk-limited) mechanism, especially in the films grown to thicknesses exceeding 6–8 nm. Clear dependences on the precursor chemistry were not established.

Table 7. Film structure, thickness, d , annealing status, and dominating conduction mechanisms in selected ZrO_2 and HfO_2 films grown from different precursors. All films were integrated to MOS structures.

| Precursor | Thickness, nm | Conduction mechanism As-dep/annealed | Reference |
|--|---------------|--------------------------------------|-----------|
| $ZrCp(NMe_2)_3$ | 6.8 | Poole-Frenkel / Schottky emission | [III] |
| $(CpMe)_2ZrMe_2$ | 13.1 | Poole-Frenkel | [I, II] |
| $(CpMe)_2Zr(OMe)Me$ | 11.9 | Schottky emission/Poole-Frenkel | [I,II] |
| $(CpMe)_2Hf(OMe)Me$ | 8.3 | Poole-Frenkel | [I] |
| $CpHf(NMe_2)_3$ | 5.5 | Fowler-Nordheim / Schottky emission | [I, IV] |
| $CpHf(NMe_2)_3$ Doped with Y ($(CpMe)_3Y$) | 6.7 | Schottky emission /Poole-Frenkel | [IV] |

8.10.2. Conduction mechanism in MIM structures

It is known, that the dominant conduction mechanisms can depend on applied voltage polarity, electrode material and film composition [81,146–150]. The impact of top-electrode metal on the conduction mechanisms of oxide thin films-based MIM capacitors was investigated by several groups [149–152] and in several MIM structures Au (or Al or Cr)/ HfO_2 /Pt [150], TiN/ $Zr_{(1-x)}Al_xO_2$ /TiN [152], TiN/ HfO_2 (or ZrO_2)/ TiN [147] and so on. They found that the density of currents through the samples depends on the work function (W) between film and electrode materials. The current density increases rapidly with temperature and decreases exponentially with the work function. Since the work function measurements between real film and electrode were difficult, they fitted the real measurement with most common conduction mechanism and from that fitting the barrier heights and most obvious conduction mechanism were derived. In our samples, only two different metals (Al $W=4.06$ – 4.26 eV and Ti $W=4.33$ eV) [153] were exploited as gate or top electrodes, irrespectively of the material grown, and the samples are thus appreciably comparable in terms of the configuration of the capacitors.

ZrO_2 – Er_2O_3 (Gd_2O_3) nanolaminates and ZrO_2 :Er(Gd) doped films were exclusively grown on highly-conducting silicon substrates forming MIM-like capacitors, with Al/Ti top electrodes e-beam evaporated, which enabled measurements of currents driven by the dielectric films under both polarities (Figure 28). Shape of the typical J - E curves measured shown in Figure 28 indicates that various conduction mechanisms can be expected at different electric field ranges and, possibly, under both polarities [V,VI,VII].

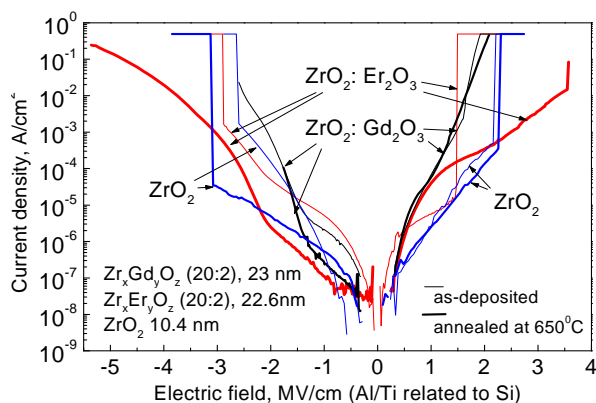


Figure 28. Selected current density–electric field curves of undoped ZrO_2 (on SiN_x), Er-doped and Gd-doped ZrO_2 films grown from $\text{CpMe}_2\text{Zr}(\text{OMe})\text{Me}$, $\text{Er}(\text{thd})_3$ (on SiN_x), $\text{Gd}(\text{thd})_3$ (on SiO_2) and O_3 . The doped films were grown with ZrO_2 :rare earth oxide cycle ratio of 20:2. Annealing was carried out at 650°C in N_2 for 10 min.

Conduction mechanisms most likely to be assigned to pure and doped ZrO_2 films were identified as Poole-Frenkel conduction, i.e. the charge transport dominated by field-assisted excitation of carriers from gap states into conduction band throughout the dielectric “bulk”. This type of transport mechanism may be regarded as that most frequently observed in wide-band-gap gate and memory dielectrics [29,105,138,145,148,154,]. At higher electric fields (2.3 MV/cm ...5 MV/cm) and/or at low temperatures (77 K) the tunnel emission caused by Fowler–Nordheim emission in ZrO_2 thin films are considered [145,155]. In the films grown from cyclopentadienyls in the framework of the present thesis [V,VII], the bulk-limited, i.e. the Poole-Frenkel conduction was either dominating or strongly contributing to the general leakage currents.

In doped ZrO_2 films, the leakage currents tended to increase with the content of dopant (Y, Er, Gd). At low voltages, the Schottky-like thermally assisted emission of carriers over interface barriers into dielectrics could be taken into account, especially in the case of the thinnest films grown. Schottky plots are presented by Figure 29 for ZrO_2 , Er_2O_3 and ZrO_2 :Er grown from $(\text{CpMe})_2\text{Zr}(\text{OMe})\text{Me}$ and $\text{Er}(\text{thd})_3$. Linear relationship between $\ln J$ and $E^{1/2}$ was generally obtained. The barrier heights can be determined at a fixed electric field E by plotting $\ln(J/T^2)$ versus $1/T$ and measured from its slope. The barrier heights were 0.28 and 0.39 eV for undoped Er_2O_3 and ZrO_2 , respectively. Barrier heights of 0.49, 0.53, and 0.73 eV were obtained for films grown with ZrO_2 : Er_2O_3 cycle ratios of 15:2 (Er:Zr = 0.014 by RBS), 10:2 (Er:Zr = 0.061 by RBS) and 6:2 (Er:Zr = 0.103 by RBS), respectively. With dot electrodes on annealed films, the corresponding values for doped films were 0.56, 0.54, and 0.51 eV. Thus, it seems that the height of the barrier was somewhat affected by the film composition but remains in the range also earlier measured in

ZrO₂-based structures. Earlier studies on ZrO₂-based films have implied, for instance, that the height of the barrier can vary between 0.47 and 0.53 eV in Au/ZrO_x/Si capacitors, depending on the film stoichiometry, and can then increase with the dielectric permittivity [151,155].

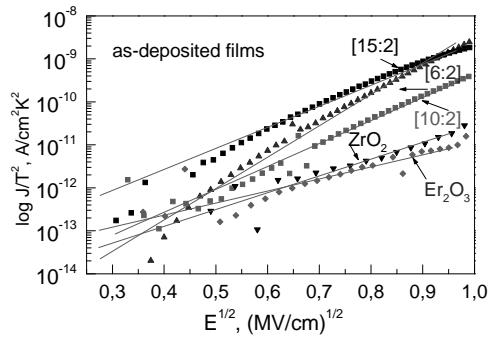


Figure 29. Schottky plots of ZrO₂, Er₂O₃ and ZrO₂:Er₂O₃ films. The J/T^2 curves measured at room temperature.

8.10.3. Conduction mechanism in nanolaminated structures

Current-density electric field (J - E) curves for laminates deposited from two different rare earth oxides and ZrO₂ are presented in Figure 30. The nanolaminates were grown to thicknesses 15–30 nm, i.e. to thicknesses sufficiently high for the formation of a nanolaminated (multilayered) structure.

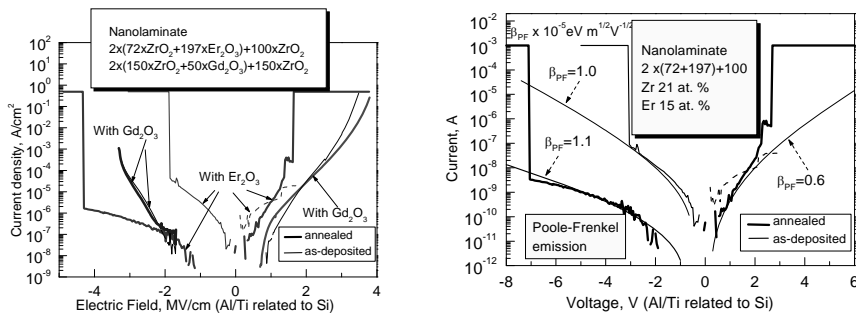


Figure 30. Leakage current density versus electric field curves of 16.4 nm thick ZrO₂:Er₂O₃ and 28.8 nm thick ZrO₂:Gd₂O₃ films on SiN_x substrate (left panel), and leakage current density versus voltage curves of selected Er₂O₃-ZrO₂ nanolaminates fitted to the bulk-limited conduction mechanism before and after annealing (right panel). Growth cycle sequences, cation contents and annealing status are indicated by labels.

In such structures, quite expectedly the bulk conduction mechanisms would dominate. Indeed, no role of the interface barriers was recognized in the ZrO_2 dielectrics nanolaminated with rare earth oxides Er_2O_3 and Gd_2O_3 .

The charge transport in nanolaminate structures was overwhelmed by Poole-Frenkel mechanism. The factor β_{PF} , as the Poole-Frenkel coefficient, was calculated on the basis of the measured I-U curves from the slope of the $\ln(I/E) - E^{1/2}$ relationships in logarithmic scale [104,105] (Figure 31). In films with increased rare earth content, the scatter of $J-E$ curves increased which made the conduction mechanism analysis more complicated. In general, at low voltages either Poole-Frenkel effect or Richardson-Schottky emission could dominate.

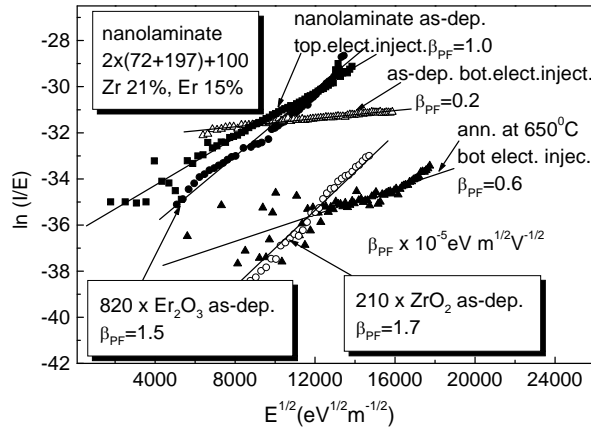


Figure 31. Poole-Frenkel plots for ZrO_2 and Er_2O_3 films and for a nanolaminate grown using a cycle sequence of $2 \times (72 \times \text{ZrO}_2 + 197 \times \text{Er}_2\text{O}_3) + 100 \times \text{ZrO}_2$. Annealing status, voltage polarity and Poole-Frenkel coefficients are indicated by labels.

The currents were controlled by the bulk properties of the $\text{ZrO}_2\text{-Gd}_2\text{O}_3$ and $\text{Er}_2\text{O}_3\text{-ZrO}_2$ nanolaminates, rather than interfaces between electrodes and oxide films, as clearly revealed by the Poole-Frenkel characteristics. In terms of possible pragmatic applications, such configurations may serve, for instance, as optical materials, being not necessarily meant to outperform the non-doped or e.g. aluminum oxide-doped ZrO_2 as memory dielectrics. In order to further study the possible applications in nanoelectronics, the total thickness of laminates as well as the thicknesses of constituent materials should be decreased and the material possibly grown as Er or Gd doped ZrO_2 instead of multilayers. However, the study has shown that Er_2O_3 and Gd_2O_3 can be alternately layered with ZrO_2 with their characteristic crystal structure, and the resulting material essentially retains the insulating dielectric properties.

SUMMARY AND CONCLUSIONS

Well-controlled atomic layer deposition of high-quality thin films of ZrO_2 and HfO_2 can be realized using novel cyclopentadienyl-based precursors in normal laboratory conditions. Cyclopentadienyls of zirconium and hafnium, viz. $(\text{CpMe})_2\text{ZrMe}_2$, $(\text{CpMe})_2\text{Zr}(\text{OMe})\text{Me}$, $(\text{CpMe})\text{Zr}(\text{NMe}_2)_3$, $(\text{CpEt})\text{Zr}(\text{NMe}_2)_3$, $(\text{CpMe})_2\text{Hf}(\text{OMe})\text{Me}$, and $\text{CpHf}(\text{NMe}_2)_3$ ($\text{Cp} = \text{C}_5\text{H}_5$, $\text{Me} = \text{CH}_3$, and $\text{Et} = \text{C}_2\text{H}_5$) together with ozone as the oxygen source are thus appropriate precursors for ALD process, providing dense dielectric and insulating films on semiconductor or metallic substrates. Appreciably high conformality (step-coverage) on three-dimensional substrates can be achieved.

Both HfO_2 and ZrO_2 films deposited at 300–350°C consisted predominantly of the monoclinic phase. Upon decreasing the film thickness down to 5–15 nm, the significance of metastable cubic or tetragonal phases increased, especially in ZrO_2 films, which was promising in terms of higher dielectric permittivity and therefore increasing capacitance. The precursors containing two Cp-ligands and oxygen seemed to be more stable and yielded films with slightly higher phase homogeneity compared to precursors containing two Cp-ligands without methoxy-groups (OMe). These films were also more insulating, although not necessarily superior in terms of electronic defect density. Leakage currents in HfO_2 were lower than those in ZrO_2 , although the ZrO_2 films could possess even lower interface trap densities than HfO_2 .

Conduction mechanisms were quite alike in films grown from the different precursors, but the ultrathin films grown from $(\text{CpMe})_2\text{Zr}(\text{OMe})\text{Me}$ appeared more insulating possessing higher breakdown fields than those e.g. in the films grown from $(\text{CpMe})_2\text{ZrMe}_2$. The dominant conduction mechanism was bulk-limited field-assisted excitation of charge carriers, although at low voltages thermal excitation over interfacial barriers could also be taken into account.

Since the ability of metastable cubic/tetragonal phases of HfO_2 and/or ZrO_2 to withstand post-deposition annealing procedures without transformation to lower-permittivity monoclinic phase was a likely issue when fabricating high-density capacitors, the films were further doped or mixed with rare earth metal oxides. In the case of HfO_2 , quite a recently developed monocyclopentadienyl-based precursor $\text{CpHf}(\text{NMe}_2)_3$ was chosen and used in the experiments devoted to the studies on Y_2O_3 -doped HfO_2 . In the case of ZrO_2 , a well-behaving compound $(\text{CpMe})_2\text{Zr}(\text{OMe})\text{Me}$ was chosen for the preparation of ZrO_2 films doped or nanolaminated with Gd_2O_3 and Er_2O_3 .

Doped HfO_2 :Y films were amorphous in as-deposited state but crystallized in the form of metastable polymorphs after heat-treatments above 500°C, possessing higher capacitance and lower equivalent oxide thickness compared to those of non-doped HfO_2 . The leakage currents remained significant, probably due to somewhat inhomogeneous crystallization. ZrO_2 :Gd and ZrO_2 :Er films were crystalline already in as-deposited state, and the cubic polymorph of ZrO_2 was retained upon annealing at 650°C in the doped films, whereas lower

permittivity monoclinic ZrO_2 became apparent in the nondoped films already in the as-deposited state. The dielectric permittivity value of 31 was achieved in the $\text{ZrO}_2:\text{Er}_2\text{O}_3$ films with an Er:Zr cation ratio of 0.09 and 30 in the $\text{ZrO}_2:\text{Gd}_2\text{O}_3$ films with a Gd:Zr cation ratio of 0.027, whereas in non-doped films permittivity values above 20–25 could not be measured. Concerning the bottom electrode materials, the best results in terms of permittivity and leakage currents were achieved with Ru, allowing equivalent oxide thickness below 1 nm and a current density of 3×10^{-8} A/cm² at 1 V. In general, at electric fields below 2–3 MV/cm, normal and trap-compensated Poole–Frenkel conduction mechanisms were competing, whereas at higher fields, Fowler–Nordheim and/or trap-assisted tunneling were to be considered. In $\text{Er}_2\text{O}_3\text{-ZrO}_2$ and $\text{Gd}_2\text{O}_3\text{-ZrO}_2$ nanolaminates the cubic ZrO_2 and rare earth oxide phases dominated, but the capacitance increased after annealing in the films with relatively low rare earth metal content and decreased in the case of higher rare earth content, being indicative of the sensitivity of dielectric behavior on the contribution of ZrO_2 phases.

The processes and resulting films examined within the present study may well become considered as those relevant to the fabrication of high-performance capacitor dielectric materials. Further studies might become concentrated on the optimization of the dopant content and deposition (cycle) time parameters, in order to improve the structural stability, capacitance density, pre-breakdown leakage currents and conformal growth over 3D substrates. In addition, the search for even better cyclopentadienyl-based precursors for both host and dopant materials may continue.

SUMMARY IN ESTONIAN

Käesoleva väitekirja pealkiri on: “Kõrge dielektrilise läbitavusega isolaatorkilede aatomkihtsadestamine tsüklopentadienüülähteainetest”.

Õhukeste ja kõrgekvaliteediliste ZrO_2 ja HfO_2 kilede kontrollitavat aatomkihtsadestust on võimalik realiseerida kasutades suhteliselt uudseid tsüklopentadienüülidepõhiseid metallide lähteaineid tavalistes laboratooriumitingimustes (mitte ilmtingimata puhasruumis). Tsirkooniumi ja hafniumi tsüklopentadienüülid, ehk sellised ühendid nagu $(CpMe)_2ZrMe_2$, $(CpMe)_2Zr(OMe)Me$, $(CpMe)Zr(NMe_2)_3$, $(CpEt)Zr(NMe_2)_3$, $(CpMe)_2Hf(OMe)Me$ ja $CpHf(NMe_2)_3$ ($Cp = C_5H_5$, $Me = CH_3$, ja $Et = C_2H_5$) osutusid aatomkihtsadestusprotsessi jaoks sobivateks tsirkooniumi ja hafnium lähteaineteks, kui hapniku lähteaine osooniga. Antud lähteainekeemial põhineva sadestusprotsessi tulemusena oli võimalik saada tiheda struktuuriga dielektrilisi ja isoleerivaid metalloksiidkilesid pooljuht- ja metallaluspindadel (substraatidel). Kasutades neid lähteaineid, oli võimalik saavutada ühtlane, s.t. konformaalne kasv ka kolme-dimensionaalsetel substraatidel.

Nii ZrO_2 kui HfO_2 kiled kristalliseerusid sadestustemperatuuridel vahemikus $300\text{--}350^\circ\text{C}$, koosnedes peamiselt nende oksiidide monokliinsetest faasidest. Kõige õhemates töös uuritud kiledes paksustega ca. $5\text{--}15$ nm suurenes oluliselt metastabiilsete kuubilise ja/või tetragonaalse faasi osakaal. Kuna nende materjalide metastabiilsetest faasidest koosnevates tahkiskihitudes on varemgi täheldatud efektiivse dielektrilise läbitavuse ja seega kondensaatorkonfiguratsioonis ka mahtuvuse tõusu, võis tuvastatud faasikoostist lugeda paljulubavaks. Need metallilähteained, mille koostises oli kaks tsüklopentadienüülrühma ja samuti hapnik, näisid teistega võrreldes olevat keemiliselt stabiilsemad ja ülikoolilaboratooriumi tingimustes paremini käsitletavad. Samuti võimaldasid sellised lähteained sadestada faasikoostise mõttes mõnevõrra ühtlasemaid kilesid. Veel osutusid sellised kiled veidi paremini isoleerivateks, ehk nendes mõõdetud lekkevool ei olnud väga kõrge. Samas siiski ei pruukinud sellised kiled olla teistest paremad siirdpindade defektitiheduse mõttes. Materjalidevahelises võrdluses tuli jälle kord ilmsiks, et HfO_2 kiledes on lekkevool väiksem võrreldes vooludega ZrO_2 kiledes, kuid ZrO_2 kiled võimaldasid valmistada kondensaatorstruktuure isegi väiksema piirpinnadefektide tihedusega.

Juhtivusmehhanismid erinevatest lähteainetest sadestatud tahkiskihitudes olid üldiselt küllaltki sarnased. Mõningaid erisusi võis täheldada eeskätt üldistes karakteristikutes: näiteks õhukesed ZrO_2 kiled, mis sadestati kasutades lähteainet $(CpMe)_2Zr(OMe)Me$, osutusid siiski paremini isoleerivateks ja nendele tuli läbilöögi tekitamiseks rakendada kõrgemaid pingeid võrreldes kiledega, mis kasvatati lähteainest $(CpMe)_2ZrMe_2$. Juhtivusmehhanismid kiledes olid peamiselt kilesiseses materjalis elektrivälja poolt võimendatud laengukandjate emissioonist juhtivustsooni (Poole-Frenkel'i efekt). Suhteliselt madalatel

pingetel võis siiski ka esineda laengukandjate termilist ergastust üle elektroodi ja metalloksiidi vahelise piirpindbarjääri (Schottky efekt).

ZrO₂ ja HfO₂ kuubilise või tetragonaalse faasi stabiliseerimine järeltöötlustemperatuuril monokliinseks faasiks transformeerimise vastu on osutunud probleemiks. Seetõttu stabiliseeriti neid faase dopeerides või kombineerides kilesid haruldaste muldmetallide oksiididega. HfO₂ juhul kasutati hiljuti välja-töötatud ühte tsüklopentadienüüli ja kolme amino-gruppi sisaldavat lähteainet CpHf(NMe₂)₃ üttriiumiga dopeeritud HfO₂ kilede sadestamisel. ZrO₂ puhul kasutati stabiliseerimiseks gadoliiniumi ja erbiiumi okside, kusjuures ZrO₂ ise kasvatati lähteainest (CpMe)₂Zr(OMe)Me.

Dopeeritud HfO₂:Y kiled osutusid kasvatusjärgselt amorfseteks, kuid kristalliseerusid metastabiilsete faasidena kuumutamisel temperatuuridel üle 500°C. HfO₂:Y kilede basil loodud kondensaatorstruktuuride mahtuvus osutus kõrgemaks ja mahvuvuslik ekvivalentoksiidi paksus madalamaks võrreldes dopeerimata materjaliga. Lekkevoolud jäid küll märkimisväärselt kõrgeteks, tõenäoliselt mõnevõrra heterogeense faasikoostise tõttu. ZrO₂:Gd ja ZrO₂:Er kiled kristalliseerusid juba kasvatusjärgselt ning kuubiline ZrO₂ stabiliseerus vähemalt lõõmutustemperatuurini 650°C, samas kui dopeerimata kiledes võis näha monokliinset faasi juba lõõmutamata materjalis. Dielektrilise läbitavuse väärtus tõusis dopeeritud kiledes, näiteks väärtuseni 31 ZrO₂:Er₂O₃ kiledes, milles Er:Zr katioonsuhe oli 0.09 ja väärtuseni 30 ZrO₂:Gd₂O₃ kiledes, milles Gd:Zr katioonsuhe oli 0.027. Samas dopeerimata kiledes dielektrilise läbitavuse väärtus ei tõusnud üle 20–25. Parimad tulemused saavutati ruteeniumist aluselektroodile sadestatud kiledes, arvestades mõõdetud ekvivalentoksiidi paksust alla 1 nanomeetri ning lekkevoolutugevust 3×10^{-8} A/cm² ühevoldisel pingel. Üldiselt elektriväljades alla 2–3 MV/cm konkureerisid neis kiledes tavaline ja laengulõksudega kompenseeritud Poole-Frenkel'i juhivusmehhanism. Kõrgemate väljade korral võis arvestada ka Fowler-Nordheimi või lõksude poolt assisteeritud tunnellerumisega. ZrO₂-Er₂O₃ ja ZrO₂-Gd₂O₃ nanolaminaatides domineerisid faasikoostise mõttes kuubilised komponentoksiidide faasid. Neil nanolaminaatidel baseeruvates kondensaatorites tõusis mahtuvus peale lõõmutusprotseduuri just neis kiledes, kus muldmetalli sisaldus oli suhteliselt väike, mis andis tunnistust just ZrO₂ faaside tähtsusest dielektriliste omaduste mõjutamisel.

Selles töös uuritud sadestusprotsessid ja sadestatud kilede kvaliteet lubavad arvestada uuritud materjalidega paremate mälukondensaatorite väljatöötamisel. Edasistes uuringutes võiks pühenduda dopantmaterjalide kontsentratsiooni ja sadestustsükli parameetrite optimeerimisele, saavutamaks veel paremat struktuurset stabiilsust, kõrgemaid mahtuvustihedusi, madalamaid läbilöögieelseid lekkevoolutugevusi ning eriti ühtlasemat kasvu kolmedimensionaalsetel kõrge aspektisuhtega substraatidel. Lisaks võiksid jätkuda uute ja parendatud omadustega tsüklopentadienüüllähteainete otsingud.

ACKNOWLEDGEMENTS

At first, I would like to give my special thanks to my supervisors. Dr. Kaupo Kukli is thanked for guiding me throughout the fascinating high-k topic. Docent Kalev Tarkpea, my mentor, is thanked for the continuous support in the life of a PhD student.

I am most grateful to Dr. Jaakko Niinistö, Prof. Mikko Ritala and Prof. Markku Leskelä for providing access to the projects, reactors and to the material characterization equipment available at the University of Helsinki, Laboratory of Inorganic Chemistry, during the scholarships in Finland at the University of Helsinki.

I am indeed very thankful to my other co-authors and co-workers: Dr. Charles L. Dezelah, Mr. Mikko Heikkilä, Dr. Peter N. Heys, Dr. Indrek Jõgi, Mrs. Jekaterina Kozlova, Dr. Jun Lu, Prof. Lauri Niinistö, Dr. Timo Sajavaara, Dr. Fuquan Song, Dr. Massimo Tallarida, Dr. Matti Putkonen, Dr. Paul Williams. They have most directly been involved in those studies. Their contribution to thin films ranged from growth experiments to characterization and stimulating writing about the thin films.

My special thanks belong to Prof. Jaan Aarik for useful discussions and support to understanding the theoretical background of thin films characterization.

I am grateful my family for they support and understanding during the PhD studies.

The study has been partially supported by the Centre for Higher Education Development of Archimedes Foundation, Doctoral Studies and Internationalization Program “DoRa,” and graduate school “Functional Materials and Processes,” receiving funding from the European Social Fund under project 1.2.0401.09–0079, Estonian Ministry of Education and Research (targeted projects SF0180042s07 and SF0180046s07), Estonian Science Foundation (grant no. 6651 and no. 7845).

REFERENCES

1. M. T. Bohr, R. S. Chau, T. Ghani, K. Mistry, *IEEE Spectrum* 44 (2007) 29.
2. J. Hicks, D. Bergstrom, M. Hattendorf, J. Jopling, J. Maiz, S. Pae, C. Prasad, J. Wiedemer, *Intel Technol. J.* 12 (2008) 131.
3. P. Packan, S. Akbar, M. Armstrong, M. Brazier, H. Deshpande, K. Dev, G. Ding, T. Ghani, O. Golonzka, W. Han, J. He, R. Heussner, R. James, J. Jopling, C. Kenyon, S-H. Lee, M. Liu, S. Lodha, B. Mattis, A. Murthy, L. Neiberg, J. Neiryneck, S. Pae, C. Parker, L. Pipes, J. Sebastian, J. Seiple, B. Sell, S. Sivakumar, B. Song, A. St. Amour, K. Tone, T. Troeger, C. Weber, K. Zhang, S. Natarajan, *The International Electron Devices Meeting (IEDM)* 2009.
4. K. Mistry, C. Allen, C. Auth, B. Beattie, D. Bergstrom, M. Bost, M. Brazier, M. Buehler, A. Cappellani, R. Chau, C.-H. Choi, G. Ding, K. Fischer, T. Ghani, R. Grover, W. Han, D. Hanken, M. Hattendorf, J. He, J. Hicks, R. Huessner, D. Ingerly, P. Jain, R. James, L. Jong, S. Joshi, C. Kenyon, K. Kuhn, K. Lee, H. Liu, J. Maiz, B. McIntyre, P. Moon, J. Neiryneck, S. Pae, C. Parker, D. Parsons, C. Prasad, L. Pipes, M. Prince, P. Ranade, T. Reynolds, J. Sandford, L. Shifren, J. Sebastian, J. Seiple, D. Simon, S. Sivakumar, P. Smith, C. Thomas, T. Troeger, P. Vandervoorn, S. Williams, K. Zawadzki, *IEEE* (2007).
5. G. D. Wilk, R. M. Wallace, J. M. Anthony, High-k gate dielectrics: Current status and materials properties considerations, *J. Appl. Phys.* 89 (2001) 5243.
6. A. Toriumi, K. Kita, Y. Zhao, J. Widiez, T. Nabatame, H. Ota, M. Hirose, *IEEE* (2007).
7. E. P. Gusev, E. Cartier, D. A. Buchanan, M. Gribelyuk, M. Copel, *Microel. Eng.* 59 (2001) 341.
8. S. Monfray, C. Fenouillet-Beranger, G. Bidal, F. Boeuf, S. Denorme, J. L. Huguenin, M. P. Samson, N. Loubet, J. M. Hartmann, Y. Campidelli, V. Destefanis, C. Arvet, K. Benotmane, L. Clement, O. Faynot, T. Skotnicki, *Solid-State Electron.* 54 (2010) 90–96.
9. K. Kakushima, M. Nakagawa, P. Ahmet, K. Tsutsui, N. Sugii, T. Hattori, H. Iwai, *Semicond. Sci. Technol.* 25 (2010) 045029.
10. M. Ritala, J. Niinistö, *ECS Transactions* 25 (8) (2009) 641.
11. H. Kim, H. B. R. Lee, W.-J. Maeng, *Thin Solid Films* 517 (2009) 2563.
12. M. Ritala, M. Leskelä, *Appl. Surf. Sci.* 75 (1994) 333.
13. J. Aarik, A. Aidla, A. A. Kiisler, T. Uustare, V. Sammelselg, *Thin Solid Films* 340 (1999) 110.
14. J. Aarik, A. Aidla, H. Mändar, T. Uustare, V. Sammelselg, *Thin Solid Films* 97 (2002) 408.
15. U. Schroeder, S. Jakschik, E. Erben, A. Avellan, S. P. Kudelka, M. Kerber, A. Link, A. Kersch, *ECS Transactions* 1 (2006) 125.
16. K. Kukli, M. Ritala, M. Leskelä, J. Sundqvist, L. Oberbeck, J. Heitmann, U. Schröder, J. Aarik, A. Aidla, *Thin Solid Films* 515 (2007) 6447.
17. S. Codato, G. Carta, G. Rossetto, G. A. Rizzi, P. Zanella, P. Scardi, M. Leoni, *Chem. Vap. Deposition* 5 (1999) 159.
18. M. Putkonen, L. Niinistö, *J. Mater. Chem.* 11 (2001) 3141.
19. J. Niinistö, M. Putkonen, L. Niinistö, K. Arstila, T. Sajavaara, J. Lu, K. Kukli, M. Ritala, M. Leskelä, *J. Electrochem. Soc.* 153 (2006) F39.

20. J. Niinistö, M. Putkonen, L. Niinistö, F. Song, P. Williams, P. N. Heys, R. Odedra, *J. Chem. Mater.* 19 (2007) 3319
21. C. L. Dezelah IV, J. Niinistö, K. Kukli, F. Munnik, J. Lu, M. Ritala, M. Leskelä, L. Niinistö, *Chem. Vap. Deposition* 14 (2008).
22. J. Niinistö, K. Kukli, M. Kariniemi, M. Ritala, M. Leskelä, N. Blasco, A. Pinchart, C. Lachaud, N. Laaroussi, Z. Wang, C. Dussarrat, *J. Mater. Chem.* 18 (2008) 5243.
23. J. Niinistö, M. Putkonen, L. Niinistö, K. Kukli, M. Ritala, M. Leskelä, *J. Appl. Phys.* 95 (2004) 84.
24. X. Zhao, D. Vanderbilt, *Phys. Rev. B* 74 (2006) 12108.
25. D. P. Thompson, A. M. Dickins, J. S. Thorp, *J. Mater. Sci.* 27 (1992) 2267.
26. K. Kukli, J. Ihanus, M. Ritala, M. Leskelä, *J. Electrochem. Soc.* 144 (1997) 300.
27. Y. Yamamoto, K. Kita, K. Kyuno, A. Toriumi, *Appl. Phys. Lett.* 89 (2006) 032903.
28. L. Wu, H. Y. Yu, K. L. Pey, J. S. Pan, M. Tuominen, E. Tois, D. Y. Lee, K. Y. Hsu, K. T. Huang, H. J. Tao, Y. J. Mii, *Electrochem. Solid-State Lett.* 13 (2010) G21.
29. K. B. Jinesh, Y. Lamy, E. Tois, R. Firti, F. Roozeboom, W. F. A. Besling, *J. Mater. Res.* 25 (2010) 1629.
30. G. H. Chen, Z. F. Hou, X. G. Gong, Q. Li, *J. Appl. Phys.* 104 (2008) 070101-1-6.
31. J. Niinistö, K. Kukli, T. Sajavaara, M. Ritala, M. Leskelä, L. Oberbeck, J. Sundqvist, U. Schröder, *Electrochem. Solid-State Lett.* 12 (2009) G1.
32. L. Shi, Y. Zhou, J. Yin, Z. Liub, *J. Appl. Phys.* 107 (2010) 014104.
33. P. R. Chalker, M. Werner, S. Romani, R. J. Potter, K. Black, H. C. Aspinall, A. C. Jones, C. Z. Zhao, S. Taylor, P. N. Heys, *Appl. Phys. Lett.* 93 (2008) 182911.
34. S. Govindarajan, T. S. Böske, P. Sivasubramani, P. D. Kirsch, B. H. Lee, H.-H. Tseng, S. Ramanathan, B. E. Gnade, *Appl. Phys. Lett.* 91 (2007) 062906.
35. P. Tsipas, S. N. Volkos, A. Sotiropoulos, S. F. Galata, G. Mavrou, D. Tsoutsou, Y. Panayiotatos, A. Dimoulas, C. Marchiori, J. Fompeyrine, *Appl. Phys. Lett.* 93 (2008) 082904
36. K. B. Jinesh, W. F. A. Besling, E. Tois, J. H. Klootwijk, R. Wolters, W. Dekkers, M. Kaiser, F. Bakker, M. Tuominen, F. Roozeboom, *Appl. Phys. Lett.* 93 (2008) 062903.
37. Y. Zhang, S. Jin, C. Liao, C. H. Yan, *Mater. Lett.* 56 (2002) 1030.
38. M. Ritala, M. Leskelä, In *Handbook of Thin Film Materials; Nalwa. H. S.. Ed.; Academic Press: San Diego. CA.* 1 (2001) pp 103.
39. M. Leskelä, M. Ritala, *Angew. Chem. Int. Ed.* 42 (2003) 5548.
40. D. G. Schlom, S. Guha, S. Datta, *MRS Bulletin* 33 (2008) 1017.
41. A. Nisar, A. C. Valles, K. Sivakumar, *Intel Technology Journal.* 12 (2008) 131.
42. M. Bohr, IDF 2009 (Intel Developer Forum). SPCS. (2009), <http://software.intel.com/en-us/articles/teach-parallel-at-idf-2009-san-francisco/20.09.2010>
43. I. Gilvarry, *Intel Technol. J.* 13 (2009) 146.
44. M. A. Pavanello, J. A. Martino, E. Siomoen, R. Rooyackers, N. Collaert, C. Claeys, *Solid-State Electron.* 51 (2007) 285.
45. K. S. Novoselov, A. K. Geim, S. V. Morozov, D. Jiang, Y. Zhang, S. V. Dubonos, I. V. Grigorieva, A. A. Firsov, *Science* 22 (2004) 666.
46. I. Meric, M. Y. Han, A. F. Young, B. Ozyilmaz, P. Kim, K. L. Shepard, *Nature Nanotechnology* 3 (2008) 654.

47. Y. Xuan, Y. Q. Wu, T. Shen, M. Qi, M. A. Capano, J. A. Cooper, P. D. Ye, *Appl. Phys. Lett.* 92 (2008) 013101.
48. F. Xia, D. B. Farmer, Y. Lin, P. Avouris, *Nano Lett.* 10 (2010) 715.
49. A. Reina, X. Jia, J. Ho, D. Nezich, H. Son, V. Bulovic, M. S. Dresselhaus, J. Kong, *Nano Lett.* 9 (2009) 30.
50. J. Campos-Delgado, J. M. Romo-Herrera, X. Jia, D. A. Cullen, H. Muramatsu, Y. A. Kim, T. Hayashi, Z. Ren, D. J. Smith, Y. Okuno, T. Ohba, H. Kanoh, K. Kaneko, M. Endo, H. Terrones, M. S. Dresselhaus, M. Terrones, *Nano Lett.* 8 (2008) 2773.
51. D. B. Farmer, H.-Y. Chiu, Y.-M. Lin, K. A. Jenkins, F. Xia and P. Avouris, *Nano Lett.* 9 (2009) 4474.
52. H. Alles, J. Aarik, A. Aidla, A. Fay, J. Kozlova, A. Niilisk, M. Pärs, M. Rähn, M. Wiesner, P. Hakonen, V. Sammelselg, *Cent. Eur. J. Phys.* (2010) DOI: 10.2478/s11534-010-0040-x
53. H. Zhang, R. Solanki, *J. Electrochem. Soc.* 148 (2001) F63.
54. O. Sneh, R. B. Clark-Phelps, A. R. Londergan, J. Winkler, T. E. Seidel, *Thin Solid Films* 402 (2002) 248.
55. W. F. A. Besling, E. Young, T. Conard, C. Zhao, R. Carter, W. Wandervorst, M. Caymax, S. De Gendt, M. Heyns, J. Maes, M. Tuominen, S. Haukka, *J. Non-Cryst. Solids* 303 (2002) 123.
56. H. Kim, P. C. McIntyre, K. C. Saraswat, *J. Mater. Res.* 19 (2004) 643.
57. Y. S. Kim, S. J. Yun, *J. Cryst. Growth* 274 (2005) 585.
58. L. Zhong, F. Chen, S. A. Campbell, W. L. Gladfelter, *Chem. Mater.* 16 (2004) 1098.
59. A. Javey, H. Kim, M. Brink, Q. Wang, A. Ural, J. Guo, P. McIntyre, P. Mceuen, M. Lundstrom, H. Dai, *Nature Mater.* 1 (2002) 242.
60. M. Rinkio, A. Johansson, G. S. Paraoanu, P. Törma, *Nano Lett.* 9 (2009) 643.
61. X. Zhu, D. Guc, Q. Li, D. E. Ioannou, H. Baumgart, J. S. Suehle, C. A. Richter, *Microel. Eng.* 86 (2009) 1957.
62. P. C. Wu, R. M. Ma, C. Liu, T. Sun, Y. Ye, L. Dai, *J. Mater. Chem.* 19 (2009) 2125.
63. S. Choi, Y.-K. Cha, B.-S. Seo, S. Park, J.-H. Park, S. Shin, K. S. Seol, J.-B. Park, Y.-S. Jung, Y. Park, Y. Park, I.-K. Yoo, S.-H. Choi, *J. Phys. D: Appl. Phys.* 40 (2007) 1426.
64. D. B. Farmer, R. G. Gordon, *J. Appl. Phys.* 101 (2007) 124503.
65. H. W. Kim, S. H. Shim, J. W. Lee, *Thin Solid Films* 515 (2007) 6433.
66. H. J. Cho, Y. D. Kim, D. S. Park, E. Lee, C. H. Park, J. S. Jang, K. B. Lee, H. W. Kim, Y. J. Ki, I. K. Han, Y. W. Song, *Solid-State Electr.* 51 (2007) 1529.
67. H. Iwai, S. Ohmi, *Microelectronics Reliability* 42 (2002) 465.
68. W.Arden, *Mat. Sci. Eng.B* 134 (2006) 104.
69. International Technology Roadmap for Semiconductors, 2001, Edition, Front End Processes, p6, [http:// public.itrs.net/](http://public.itrs.net/) 20.09.2010
70. International Technology Roadmap for Semiconductors, 2005, Edition, Front End Processes, p6, [http:// public.itrs.net/](http://public.itrs.net/) 20.09.2010
71. International Technology Roadmap for Semiconductors, 2009, Edition, Front End Processes, p6, [http:// public.itrs.net/](http://public.itrs.net/) 20.09.2010
72. D. Hisamoto, W. C. Lee, J. Kedzierski, H. Takeuchi, K. Asano, C. Kuo, E. Anderson, T. J. King, J. Bokor, *IEEE Transacti. Electron Devices*, 47 (2000) 2320.

73. J. Moers, *Appl. Phys. A* 87 (2007) 531.
74. T. Schloesser, F. Jakubowski, J. v Kluge, A. Graham, S. Slesazek, M. Popp, P. Baars, K. Muemmler, P. Moll, K. Wilson, A. Buerke, D. Koehler, J. Radecker, E. Erben, U. Zimmermann, T. Vorrath, B. Fischer, G. Aichmayr, R. Agaiby, W. Pamler, T. Schuster, W. Bergner, W. Mueller, *IEDM 2008*, (2008).
75. T. Hori, *Gate Dielectrics and MOS ULSIs, Principles, Technologies, and Applications*, Springer (1997).
76. K. H. Kuesters, M. F. Beug, U. Schroeder, N. Nagel, U. Bewersdorff, G. Dallmann, S. Jakschik, R. Knoefler, S. Kudelka, C. Ludwig, D. Manger, W. Mueller A. Tilke, *Adv. Eng. Mater.* 11 (2009) 241.
77. J. Doering, *Solid State Technol.* 53 (2010) 1.
78. P. Phatak, I. Hashim, S. Malhotra, S. Shanker, W. French, H. Chen, P. Kumar, E. Haywood, R. Endo, T. Chiang, *Solid State Technol.* 53 (2010), http://www.electroiq.com/index/display/semiconductors-article-display/0480634154/articles/solid-state-technology/semiconductors/wafer-processing/deposition-and_growth/2010/may/combinatorial-tooling.html 20.09.2010
79. J. Niinistö, A. Rahtu, M. Putkonen, M. Ritala, M. Leskelä, L. Niinistö, *Langmuir* 21 (2005) 7321.
80. J. Niinistö, K. Kukli, M. Heikkilä, M. Ritala, M. Leskelä, *Adv.Engin. Mater.* 11 (2009) 223.
81. J. Müller, T. S. Böcke, U. Schröder, M. Reinicke, L. Oberbeck, D. Zhou, W. Weinreich, P. Kücher, M. Lemberger, L. Frey, *Microel. Eng.* 86. (2009) 1818.
82. M. G. Walawalkar, A. Kottantharayil, V. R. Rao, *Synthesis and Reactivity in Inorgani Metal-Organic and Nano-Metal Chemistry* 39 (2009) 331.
83. R. L. Puurunen, *J. Appl. Phys.* 97 (2005) 121301.
84. W-M. Li, M. Ritala, M. Leskelä, R. Lappalainen, J. Jokinen, E. Soininen, B. Hüttl, E. Nykänen, L. Niinisto, *J. Appl. Phys.* 84 (1998) 1029.
85. K. Kukli, M. Ritala, M. Leskelä, *New Materials and Processes for Incoming Semiconductors Technologies.* (2006) pp 1–40.
86. J. Niinistö, M. Mäntymäki, K. Kukli, L. Costelle, E. Puukilainen, M. Ritala, M. Leskelä, *J. Cryst. Growth* 312 (2010) 245.
87. M. Leskelä, M. Ritala, *Thin Solid Films* 409 (2002) 138.
88. <http://www.picosun.com/products/index.php>. 20.09.2010
89. K.-E. Elers, T. Blomberg, M. Peussa, B. Aitchison, S. Haukka, S. Marcus, *Chem. Vap. Deposition.* 12 (2006) 13.
90. M. Ritala, K. Kukli, A. Rahtu, P. I. Räisänen, M. Leskelä, T. Sajavaara, J. Keinon, *Science* 288 (2000) 319.
91. M. Ritala, M. Leskelä, *Appl. Surf. Sci.* 75 (1994) 333.
92. M. Ritala, M. Leskelä, L. Niinistö, T. Prohaska, G. Friedbacher, M. Grasserbauer, *Thin Solid Films* 250 (1994) 72.
93. C. Auth, M. Buehler, A. Cappellani, C. Choi, G. Ding, W. Han, S. Joshi, B. McIntyre, M. Prince, P. Ranade, J. Stanford, C. Thomas, *Intel Techno. J.* 12 (2008) 77.
94. M. Verghese, S. Battle, J. Roeder, *Semiconductor International*, 04.01.2008
95. R. Huang, A. H. Kitai, *Appl. Phys. Lett.* 61 (1992) 1450.
96. J. Niinistö, M. Putkonen, L. Niinistö, S. L. Stoll, K. Kukli, T. Sajavaara, M. Ritala, M. Leskelä, *J. Mater. Chem.* 15 (2005) 2271.

97. M. Putkonen, J. Niinistö, K. Kukli, T. Sajavaara, M. Karppinen, H. Yamauchi, L. Niinistö, *Chem. Vap. Deposition* 9 (2003) 207.
98. J. W. Elam, M. J. Pellin, S. D. Elliot, A. Zydor, M. C. Faia, J. T. Hupp, *Appl. Phys. Lett.* 91 (2007) 253123.
99. K. Knapas, M. Ritala, *Chem. Mater.* 20 (2008) 5698.
100. J. Robertson, *Rep. Prog. Phys.* 69 (2006) 327.
101. J. Robertson, *J. Appl. Phys.* 104 (2008) 124111.
102. G. Lucovsky, J. G. Hong, C. C. Fulton, Y. Zou, R. J. Nemanich, H. Adel, D. G. Scholm, J. L. Freeouf, *Phys. Stat. Sol. (b)* 241 (2004) 2221.
103. D. P. Norton, *Mater. Sci. Eng. R* 43 (2004) 139.
104. S. M. Sze, *Physics of semiconductor devices*, Edition 2 1981, *New York, Wiley*.
105. S. Dueñas, H. Castán, H. Garcia, A. Gómez, L. Bailón, K. Kukli, J. Niinistö, M. Ritala, and M. Leskelä, *J. Vac. Sci. Technol. B* 271 (2009) 389.
106. G. Scarel, S. Spiga, C. Wiemer, G. Tallarida, S. Ferrari, M. Fanciulli, *Mater. Sci. Eng. B* 109 (2004) 11.
107. S. Ferrari, D. T. Dekadjevi, S. Spiga, G. Tallarida, C. Wiemer, M. Fanciulli, *J. Non-Cryst. Solids* 303 (2002) 29.
108. R. O’Kane, J. Gaskell, A. C. Jones, P. R. Chalker, K. Black, M. Werner, P. Taechakumput, S. Taylor, P. N. Heys, R. Odedra, *Chem. Vap. Deposition* 13 (2007) 609.
109. X. Zhao, D. Vanderbilt, *Phys. Rev. B* 65 (2002) 233106.
110. X. Zhao, D. Vanderbilt, *Phys. Rev. B* 65 (2002) 075105.
111. V. Fiorentini, G. Gulleri, *Phys. Rev. Lett.* 89 (2002) 266101–1
112. M. Alessandri, A. Del Vitto, R. Piagge, A. Sebastiani, C. Scozzari, C. Wiemer, L. Lamagna, M. Perego, G. Ghidini, M. Fanciulli, *Microelec. Eng.* 87 (2010) 290.
113. E. R. Andrievskaya, *J. Eur. Ceram. Soc.* 28 (2008) 2363.
114. G. Cabello, L. Lillo, C. Caro, G. E. Buono-Core, B. Chornik, M. A. Soto, *J. Non-Cryst. Solids* 354 (2008) 3919.
115. K. A. Khor, J. Yang, *Scripta Mater.* 37 (1997) 1279.
116. C. Adelman, H. Tielens, D. Dewulf, A. Hardy, D. Pierreux, J. Swerts, E. Rosseel, X. Shi, M. K. Van Bael, J. A. Kittl, S. Van Elshocht, *J. Electrochem. Soc.* 157 (2010) G105.
117. Q. Tao, G. Jursich, P. Majumder, M. Singh, W. Walkosz, P. Gu, R. Klie, C. Takoudis, *Electrochem. Solid-State Lett.* 12 (2009) G50.
118. C. Wiemer, L. Lamagna, S. Baldovino, M. Perego, S. Schamm-Chardon, P. E. Coulon, O. Salicio, G. Congelo, S. Spiga, M. Fanciulli, *Appl. Phys. Lett.* 96 (2010) 182901.
119. K. B. Jinesh, Y. Lamy, E. Tois, W. F. A. Besling, *Appl. Phys. Lett.* 94 (2009) 252906.
120. L. Lamagna, C. Wiemer, S. Baldovino, A. Molle, M. Perego, S. Schamm-Chardon, P. E. Coulon, M. Fanciulli, *Appl. Phys. Lett.* 95 (2009) 122902.
121. I. Jögi, K. Kukli, M. Ritala, M. Leskelä, J. Aarik, A. Aidla, J. Lu, *Microelec. Eng.* 87 (2010) 144.
122. T. Suntola, *Mater. Sci. Rep.* 4 (1989) 261.
123. T. Suntola, *Thin Solid Films* 216 (1992) 84.
124. K. Kukli, M. Ritala, T. Sajavaara, J. Keinonen, M. Leskelä, *Chem. Vap. Deposition* 8 (2002) 199.
125. K. Kukli, T. Pilvi, M. Ritala, T. Sajavaara, J. Lu, M. Leskelä, *Thin Solid Films* 491 (2005) 328.

126. J. Aarik, A. Aidla, A. Kikas, T. Käämbre, R. Rammula, P. Ritslaid, T. Uustare, V. Sammelselg, *Appl. Surf. Sci.* 230 (2004) 292.
127. Y. S. Kim, Y. H. Lee, K. M. Lim, M. Y. Sung, *Appl. Phys. Lett.* 74 (1999) 2800.
128. R. K. Nahar, V. Singh, A. Sharma, *J Mater Sci: Mater Electron* 18 (2007) 615.
129. M. Bhagwat, V. Ramaswamy, *Mater. Res. Bul.* 39 (2004) 1627.
130. J. Jokinen, J. Keinonen, P. Tikkanen, A. Kuronen, T. Ahlgren, K. Nordlund, *Nucl. Instr. Methods B* 119 (1996) 533
131. T. Sajavaara, Heavy Ion Recoil Spectroscopy of Surface Layers, University of Helsinki Report Series in Physics, HU-P-D99, University of Helsinki (2002), <http://ethesis.helsinki.fi/julkaisut/mat/fysik/yk/sajavaara>
132. J. Niinistö, M. Putkonen, L. Niinistö, *Chem. Mater.* 16 (2004) 2953.
133. J. Päiväsaari, M. Putkonen, L. Niinistö, *Thin Solid Films* 472 (2005) 575.
134. J. Päiväsaari, M. Putkonen, T. Sajavaara, L. Niinistö, *J. Alloys Compd.* 374 (2004) 124.
135. L. M. Terman, *Solid-State Electronics.* 5 (1962) 285.
136. C. K. Maiti, G. K. Dalapati, S. Chatterjee, S. K. Samanta, S. Varma, S. Patil, *Solid-State Electronics* 48 (2004) 2235.
137. M. Gutowski, J. E. Jaffe, C.-L. Liu, M. Stoker, R. I. Hegde, R. S. Rai, P. J. Tobin, *Appl. Phys. Lett.* 80 (2002) 1897.
138. B. G. Streeman, S. K. Banerjee, *Solid State Electronic Devices*, Sixth edition, *Prentice Hall* (2006)
139. J.-H. Kim, V. Ignatova, P. Kücher, J. Heitmann, L. Oberbeck, U. Schröder, *Thin Solid Films* 516 (2008) 8333.
140. E. H. Nicollian and J. R. Brews, *MOS (Metal Oxide Semiconductor) Physics and Technology*. *New York: Wiley* (1982) pp 2–294.
141. W. A. Hill, C. C. Coleman, *Solid State Electron*, 23 (1980) 987.
142. K. Martens, G. Brammertz, B. D. Jaeger, D. Kuzum, M. Meuris, M. M. Heyns, T. Krishnamohan, K. Saraswat, H. E. Maes, *IEEE Transact. Electron Devices*, 55 (2008) 547.
143. C. Mahata, M. K. Bera, P. K. Bose, C. K. Maiti, *Thin Solid Films* 517 (2008) 163.
144. C. K. Maiti, G. K. Dalapati, S. Chatterjee, S. K. Samanta, S. Varma, S. Patil, *Solid State Electr.* 48 (2004) 2235.
145. B. L. Yang, P. T. Lai, H. Wong, *Microelec. Reliability* 44 (2004) 709.
146. E. Gerritsen, N. Emonet, C. Caillat, N. Jourdan, M. Piazza, D. Fraboulet, B. Boeck, A. Berthelot, S. Smith, P. Mazoyer, *Solid-State Electron.* 49 (2005) 1767.
147. T. Bertaud, C. Bermond, T. Lacrevez, C. Vallée, Y. Morand, B. Fléchet, A. Farcy, M. Gros-Jean, S. Blonkowski, *Microel. Eng.* (2009) doi:10.1016/j.mee.2009.06.016.
148. K.-H. Allers, *Microel. Reliab.* 44 (2004) 411.
149. K. Fröhlich, J. Aarik, M. Tapajna, A. Rosavcá, A. Aidla, E. Dobročka, K. Hušková, *J.Vac. Sci.Technol.* B 27 (2009) 266.
150. F. El Kamel, P. Gonon, C. Vallée, C. Jorel, *J. Appl. Phys.* 106 (2009) 064508.
151. W.-C. Chen, Y.-J. Lin, Y.-H. Chen, H.-C. Chang, *Semicond. Sci. Technol.* 25 (2010) 055003.
152. W. Weinreich, R. Reiche, M.Lemberger, G. Jegert, J. Müller, L.Wilde, S. Teichert, J. Heitmann, E. Erben, L.Oberbeck, U. Schröder, A.J.aer, H. Ryszel, *Microelectro. Eng.* 86 (2009) 1826.
153. H. B. Michaelson, *J. Appl. Phys.* 48 (1977) 4729.

154. V. Mikhelashvili, G. Eisenstein, F. Edelman, R. Brenner, N. Zakharov, P. Werner, *J. Appl. Phys.* 95 (2004) 613.
155. M. T. Wang, T. H. Wang, B. Y. Y. Cheng, J. Y. Lee, *J. Electrochem. Soc.* 153 (2006) F8.

PUBLICATIONS

CURRICULUM VITAE

General data

Name and surname: Aile Tamm
Date and place of birth: 24.03.1977, Tartu, Estonia
Citizenship: Estonian
Marital Status: Married, 2 children
Contact: Institute of Physics, University of Tartu, Riia 142,
51014, Tartu, Estonia;
Telefon. +372 50 68 312,
e-mail: aile.tamm@ut.ee

Education:

2001–2010 University of Tartu, PhD student
(on acad. leave 2002–2007)
1999–2001 University of Tartu, 2001, M.Sc. (Master of Science)
1995–1999 University of Tartu, 1999, B.Sc. (Science)
1992–1995 Nõo Real Gymnasium
1984–1992 Puhja High School

Professional employment:

Since 2008 University of Tartu, Faculty of Science and Technology,
Institute of Physics, University of Tartu;
engineer.
2007–2008 Cybernetica AS
1999–2006 University of Tartu, lector
1998–1999 Estonian University of Life Sciences, lector in physic.

Administrative responsibilities:

Since 2008 member of EMRS
Since 2010 The Board member of the Estonian Physics Society
(EFS)
Since 2009 EFS web newsletter editor

Language skills:

Estonian mother tongue
English good, Russian basic.

Awards:

2010 Estonian PhD Student Conference on Functional
Material and Science 2010, FMTD-2010, the best oral
presentation.
2010 Estonian LOTE Phd Student Conference 2010, the
best oral presentation

ELULOO KIRJELDUS

Üldandmed

Ees- ja perekonnanimi: Aile Tamm
Sünniaeg ja koht: 24.03.1977, Tartu, Eesti
Kodakondsus: Eesti
Perekonnaseis: Abielus, kaks last
Kontakt: Füüsika Instituut, Tartu Ülikool, Riia 142, 51014, Tartu, Eesti
Telefon: +372 50 68 312,
e-mail: aile.tamm@ut.ee

Haridus:

2001–2010 Tartu Ülikool, doktoriõpe
(akadeemilisel puhkusel 2002–2007)
1999–2001 Tartu Ülikool, 2001, M.Sc. (Master of Science)
1995–1999 Tartu Ülikool, 1999, B.Sc. (Science)
1992–1995 Nõo Reaalgümnaasium
1984–1992 Puhja Keskkool

Teenistuskäik:

Alates 2008 insener, Tartu Ülikool, Loodus- ja tehnoloogia-
teaduskonna
Tartu Ülikooli Füüsika Instituut, Tähe 4, 51010 Tartu.
2007–2008 Cybernetica AS, referent- testija
1999–2006 TÜ, praktikumide juhendaja
1998–1999 EPMÜ, füüsika lektor.

Teadusorganisatsiooniline ja -administratiivne tegevus:

Alates 2008 Euroopa materjali teaduse ühingu liige
Alates 2010 Eesti Füüsika Seltsi laiendatud juhatuse liige
Alates 2009 EFS veebiajakirja toimetaja

Keelteoskus:

Eesti keel on emakeel, inglise keel heal tasemel ja
vene keel rahuldav.

Auhinnad:

2010 Funktsionaalsete materjalide ja teaduse konverents
FMTDK-2010 (Estonian PhD Student Conference on
Functional Material and Science 2010), parim suuline
ettekanne.
2010 LOTE PhD Üliõpilaste konverents 2010, parim
suuline ettekanne.

DISSERTATIONES PHYSICAE UNIVERSITATIS TARTUENSIS

1. **Andrus Ausmees.** XUV-induced electron emission and electron-phonon interaction in alkali halides. Tartu, 1991.
2. **Heiki Sõnajalg.** Shaping and recalling of light pulses by optical elements based on spectral hole burning. Tartu, 1991.
3. **Sergei Savihhin.** Ultrafast dynamics of F-centers and bound excitons from picosecond spectroscopy data. Tartu, 1991.
4. **Ergo Nõmmiste.** Leelishalogeniidide röntgenelektronemissioon kiiritamisel footonitega energiaga 70–140 eV. Tartu, 1991.
5. **Margus Rätsep.** Spectral gratings and their relaxation in some low-temperature impurity-doped glasses and crystals. Tartu, 1991.
6. **Tõnu Pullerits.** Primary energy transfer in photosynthesis. Model calculations. Tartu, 1991.
7. **Olev Saks.** Attoampri diapsoonis voolude mõõtmise füüsikalised alused. Tartu, 1991.
8. **Andres Virro.** AlGaAsSb/GaSb heterostructure injection lasers. Tartu, 1991.
9. **Hans Korge.** Investigation of negative point discharge in pure nitrogen at atmospheric pressure. Tartu, 1992.
10. **Jüri Maksimov.** Nonlinear generation of laser VUV radiation for high-resolution spectroscopy. Tartu, 1992.
11. **Mark Aizengendler.** Photostimulated transformation of aggregate defects and spectral hole burning in a neutron-irradiated sapphire. Tartu, 1992.
12. **Hele Siimon.** Atomic layer molecular beam epitaxy of A^2B^6 compounds described on the basis of kinetic equations model. Tartu, 1992.
13. **Tõnu Reinot.** The kinetics of polariton luminescence, energy transfer and relaxation in anthracene. Tartu, 1992.
14. **Toomas Rõõm.** Paramagnetic H^{2-} and F^+ centers in CaO crystals: spectra, relaxation and recombination luminescence. Tallinn, 1993.
15. **Erko Jalviste.** Laser spectroscopy of some jet-cooled organic molecules. Tartu, 1993.
16. **Alvo Aabloo.** Studies of crystalline celluloses using potential energy calculations. Tartu, 1994.
17. **Peeter Paris.** Initiation of corona pulses. Tartu, 1994.
18. **Павел Рубин.** Локальные дефектные состояния в CuO_2 плоскостях высокотемпературных сверхпроводников. Тарту, 1994.
19. **Olavi Ollikainen.** Applications of persistent spectral hole burning in ultrafast optical neural networks, time-resolved spectroscopy and holographic interferometry. Tartu, 1996.
20. **Ülo Mets.** Methodological aspects of fluorescence correlation spectroscopy. Tartu, 1996.
21. **Mikhail Danilkin.** Interaction of intrinsic and impurity defects in CaS:Eu luminophors. Tartu, 1997.

22. **Ирина Кудрявцева.** Создание и стабилизация дефектов в кристаллах KBr, KCl, RbCl при облучении ВУФ-радиацией. Тарту, 1997.
23. **Andres Osvet.** Photochromic properties of radiation-induced defects in diamond. Tartu, 1998.
24. **Jüri Örd.** Classical and quantum aspects of geodesic multiplication. Tartu, 1998.
25. **Priit Sarv.** High resolution solid-state NMR studies of zeolites. Tartu, 1998.
26. **Сергей Долгов.** Электронные возбуждения и дефектообразование в некоторых оксидах металлов. Тарту, 1998.
27. **Кауро Kukli.** Atomic layer deposition of artificially structured dielectric materials. Tartu, 1999.
28. **Ivo Heinmaa.** Nuclear resonance studies of local structure in $\text{RBa}_2\text{Cu}_3\text{O}_{6+x}$ compounds. Tartu, 1999.
29. **Aleksander Shelkan.** Hole states in CuO_2 planes of high temperature superconducting materials. Tartu, 1999.
30. **Dmitri Nevedrov.** Nonlinear effects in quantum lattices. Tartu, 1999.
31. **Rein Ruus.** Collapse of 3d (4f) orbitals in 2p (3d) excited configurations and its effect on the x-ray and electron spectra. Tartu, 1999.
32. **Valter Zazubovich.** Local relaxation in incommensurate and glassy solids studied by Spectral Hole Burning. Tartu, 1999.
33. **Indrek Reimand.** Picosecond dynamics of optical excitations in GaAs and other excitonic systems. Tartu, 2000.
34. **Vladimir Babin.** Spectroscopy of exciton states in some halide macro- and nanocrystals. Tartu, 2001.
35. **Toomas Plank.** Positive corona at combined DC and AC voltage. Tartu, 2001.
36. **Kristjan Leiger.** Pressure-induced effects in inhomogeneous spectra of doped solids. Tartu, 2002.
37. **Helle Kaasik.** Nonperturbative theory of multiphonon vibrational relaxation and nonradiative transitions. Tartu, 2002.
38. **Tõnu Laas.** Propagation of waves in curved spacetimes. Tartu, 2002.
39. **Rünno Lõhmus.** Application of novel hybrid methods in SPM studies of nanostructural materials. Tartu, 2002.
40. **Kaido Reivelt.** Optical implementation of propagation-invariant pulsed free-space wave fields. Tartu, 2003.
41. **Heiki Kasemägi.** The effect of nanoparticle additives on lithium-ion mobility in a polymer electrolyte. Tartu, 2003.
42. **Villu Repän.** Low current mode of negative corona. Tartu, 2004.
43. **Алексей Котлов.** Оксидионные диэлектрические кристаллы: зонная структура и электронные возбуждения. Tartu, 2004.
44. **Jaak Talts.** Continuous non-invasive blood pressure measurement: comparative and methodological studies of the differential servo-oscillometric method. Tartu, 2004.
45. **Margus Saal.** Studies of pre-big bang and braneworld cosmology. Tartu, 2004.

46. **Eduard Gerškevičš.** Dose to bone marrow and leukaemia risk in external beam radiotherapy of prostate cancer. Tartu, 2005.
47. **Sergey Shchemelyov.** Sum-frequency generation and multiphoton ionization in xenon under excitation by conical laser beams. Tartu, 2006.
48. **Valter Kiisk.** Optical investigation of metal-oxide thin films. Tartu, 2006.
49. **Jaan Aarik.** Atomic layer deposition of titanium, zirconium and hafnium dioxides: growth mechanisms and properties of thin films. Tartu, 2007.
50. **Astrid Rekker.** Colored-noise-controlled anomalous transport and phase transitions in complex systems. Tartu, 2007.
51. **Andres Punning.** Electromechanical characterization of ionic polymer-metal composite sensing actuators. Tartu, 2007.
52. **Indrek Jõgi.** Conduction mechanisms in thin atomic layer deposited films containing TiO₂. Tartu, 2007.
53. **Aleksei Krasnikov.** Luminescence and defects creation processes in lead tungstate crystals. Tartu, 2007.
54. **Küllike Rägo.** Superconducting properties of MgB₂ in a scenario with intra- and interband pairing channels. Tartu, 2008.
55. **Els Heinsalu.** Normal and anomalously slow diffusion under external fields. Tartu, 2008.
56. **Kuno Kooser.** Soft x-ray induced radiative and nonradiative core-hole decay processes in thin films and solids. Tartu, 2008.
57. **Vadim Boltrushko.** Theory of vibronic transitions with strong nonlinear vibronic interaction in solids. Tartu, 2008.
58. **Andi Hektor.** Neutrino Physics beyond the Standard Model. Tartu, 2008.
59. **Raavo Josepson.** Photoinduced field-assisted electron emission into gases. Tartu, 2008.
60. **Martti Pärs.** Study of spontaneous and photoinduced processes in molecular solids using high-resolution optical spectroscopy. Tartu, 2008.
61. **Kristjan Kannike.** Implications of neutrino masses. Tartu, 2008.
62. **Vigen Issahhanjan.** Hole and interstitial centres in radiation-resistant MgO single crystals. Tartu, 2008.
63. **Veera Krasnenko.** Computational modeling of fluorescent proteins. Tartu, 2008.
64. **Mait Müntel.** Detection of doubly charged higgs boson in the CMS detector. Tartu, 2008.
65. **Kalle Kepler.** Optimisation of patient doses and image quality in diagnostic radiology. Tartu, 2009.
66. **Jüri Raud.** Study of negative glow and positive column regions of capillary HF discharge. Tartu, 2009.
67. **Sven Lange.** Spectroscopic and phase-stabilisation properties of pure and rare-earth ions activated ZrO₂ and HfO₂. Tartu, 2010.
68. **Aarne Kasikov.** Optical characterization of inhomogeneous thin films. Tartu, 2010.

69. **Heli Valtna-Lukner.** Superluminally propagating localized optical pulses. Tartu, 2010.
70. **Artjom Vargunin.** Stochastic and deterministic features of ordering in the systems with a phase transition. Tartu, 2010.
71. **Hannes Liivat.** Probing new physics in e^+e^- annihilations into heavy particles via spin orientation effects. Tartu, 2010.
72. **Tanel Mullari.** On the second order relativistic deviation equation and its applications. Tartu, 2010.
73. **Aleksandr Lisovski.** Pulsed high-pressure discharge in argon: spectroscopic diagnostics, modeling and development. Tartu, 2010.